

A Comprehensive Hamiltonian Atmospheric Sound Propagation Model for Prediction of
Wind Turbine Noise

Sterling M. McBride

Thesis submitted to the faculty of the Virginia Polytechnic Institute and State University
in partial fulfillment of the requirements for the degree of

Master of Science
In
Mechanical Engineering

Ricardo A. Burdisso, Chair
Pablo A. Tarazaga
Michael J. Roan
Corina Sandu

December 6, 2017
Blacksburg, Virginia

Keywords: Wind Turbine Noise, Ray Tracing, Atmospheric Sound Propagation.

Copyright 2017, Sterling McBride

A Comprehensive Hamiltonian Atmospheric Sound Propagation Model for Prediction of Wind Turbine Noise

Sterling M. McBride

ABSTRACT

Wind energy is the world's fastest-growing renewable energy source. Thus, the amount of people exposed to wind farm noise is increasing. Due to its broadband amplitude modulated characteristic, wind turbine noise (WTN) is more annoying than noise produced by other common community/industrial sources. Aerodynamic noise along the blade span is the dominant noise source of modern large wind turbines. This type of noise propagates through the atmosphere in the proximity of wind farms. However, modelling and simulating WTN propagation over large distances is challenging due to the complexity of atmospheric conditions. Real temperature, wind velocity and relative humidity measurements typically show a characteristic nonlinear behavior. A comprehensive propagation model that addresses this problem while maintaining high accuracy and computational efficiency is necessary. A Hamiltonian Ray tracing (HRT) technique coupled to aerodynamically induced WTN is presented in this work. It incorporates acoustic wave refraction due to spatial speed of sound gradients, a full Doppler Effect formulation resulting from wind velocities in any arbitrary direction, proper acoustic energy dissipation during propagation, and ground reflection. The HRT method averts many of the setbacks presented by other common numerical approaches such as fast field program (FFP), parabolic equation methods (PE), and the standard Eikonal ray tracing (ERT) technique. In addition, it is not bounded to the linearity assumptions made for analytic propagation solutions. A wave phase tracking analysis through inhomogeneous and moving media is performed. Curved ray-paths are numerically computed by solving a non-linear system of coupled first order differential equations. Sound pressure levels through the propagation media are then calculated by using standard ray tubes and performing energy analysis along them. The ray model is validated by comparing a monopole's ray path results against analytically obtained ones. Sound pressure level predictions are also validated against both FFP and ERT methods. Finally, results for a 5MW modern wind turbine over a flat acoustically soft terrain are provided.

A Comprehensive Hamiltonian Atmospheric Sound Propagation Model for Prediction of Wind Turbine Noise

Sterling M. McBride

GENERAL AUDIENCE ABSTRACT

Modelling propagation of noise produced by wind turbines over large distances is a challenging task. Real temperature distributions, flow characteristics around wind turbines, and relative humidity are some of the parameters that affect the behavior of the produced sound in the atmosphere. To this end, a Hamiltonian ray tracing tool that models the propagation of wind turbine noise has been developed and is the main focus of this thesis. This method avoids many of the limitations and inaccurate assumptions presented by other common numerical and analytical approaches. In addition, current commercial noise propagation codes are incapable of fully capturing the physical complexity of the problem. Finally, validation and simulation results for a wind turbine over flat terrain are presented in order to demonstrate the superior accuracy and computational efficiency of the Hamiltonian approach.

ACKNOWLEDGEMENTS

I would like to thank my thesis advisor Dr. Ricardo Burdisso, Professor at the Department of Mechanical Engineering at Virginia Tech. His continuous advice and support during my graduate studies have encouraged my self-determination and pursue of excellence as a researcher and a professional. This work would not have been possible without his instruction, patience, and guidance. I would also like to express my gratitude to Dr. Corina Sandu, Professor at the Department of Mechanical Engineering at Virginia Tech for providing valuable advice on my research projects and broadening my area of expertise by allowing me to collaborate in international investigation efforts. In addition, I would like to thank the members of my committee Dr. Pablo Tarazga and Dr. Michael Roan, whose input has been greatly appreciated. I would like to show my appreciation to all my fellow graduate students, including Dr. Tan Li and Mr. Daniel Wu from the Vibrations and Acoustics Laboratory at Virginia Tech. I am also grateful with Mr. Mark Hurtado, for his friendship, and willingness to always help and give his best suggestions. I am thankful to God for helping me successfully reach my goals and my family for their constant support.

TABLE OF CONTENTS

ACKNOWLEDGEMENTS	iv
TABLE OF CONTENTS	v
LIST OF FIGURES.....	vii
LIST OF TABLES	x
1. INTRODUCTION	1
1.1. WIND TURBINE NOISE MODELING REVIEW	4
<i>Aerodynamic Analysis.....</i>	<i>4</i>
<i>Aeroelastic Simulation.....</i>	<i>6</i>
<i>Wind Turbine Noise Sources.....</i>	<i>7</i>
<i>Atmospheric Noise Propagation</i>	<i>10</i>
<i>Wind Turbine Noise Prediction Models.....</i>	<i>15</i>
1.2. THESIS OBJECTIVES.....	18
1.3. THESIS ORGANIZATION	20
2. ATMOSPHERIC NOISE PROPAGATION MODELS.....	21
2.1. NUMERICAL METHODS	21
<i>Fast Field Program (FFP).....</i>	<i>21</i>
<i>Crank Nicholson Parabolic Equation Method (CNPE)</i>	<i>26</i>
<i>Green's Function Parabolic Equation Method (GFPE)</i>	<i>30</i>
<i>Eikonal Ray Tracing (ERT).....</i>	<i>33</i>
2.2. ANALYTICAL METHODS	38
<i>Geometric Ray Theory.....</i>	<i>38</i>
<i>Analytic Ray Path.....</i>	<i>46</i>
2.3. COMMERCIAL SOFTWARE PROPAGATION APPROACHES	46
<i>ISO 9613-2</i>	<i>46</i>
<i>CONCAWE.....</i>	<i>49</i>
<i>ESDUpac.....</i>	<i>49</i>
<i>Harmonoise</i>	<i>50</i>
<i>Nord 2000</i>	<i>52</i>
3. HAMILTONIAN RAY TRACING.....	55
3.1. PATH OF A RAY	56
<i>Acoustic Wave's Phase</i>	<i>57</i>
<i>Homogeneous Media</i>	<i>60</i>
<i>Inhomogeneous Media.....</i>	<i>65</i>
<i>Inhomogeneous Moving Media.....</i>	<i>68</i>
<i>Numerical Solution of the Ray Paths.....</i>	<i>72</i>
3.2. ACOUSTIC PRESSURE FIELD.....	76
<i>Conservation of Energy in a Ray-Tube.....</i>	<i>77</i>
<i>Atmospheric Attenuation.....</i>	<i>81</i>
<i>Ground Attenuation and Ray Reflections</i>	<i>85</i>
3.3. METHOD VALIDATION	88

<i>Ray Path Validation</i>	88
<i>Sound Pressure Levels Validation</i>	89
4. WTNOISE MODELING TOOL.....	94
4.1. CODE STRUCTURE.....	94
4.2. COORDINATE SYSTEMS AND ROTATION MATRICES.....	97
<i>Rotor to Global Rotation</i>	98
<i>Airfoil to Rotor Rotation</i>	99
<i>Directivity to Airfoil Rotation</i>	99
<i>Directivity to Global Rotation</i>	100
4.3. BLADE DEFLECTION	100
4.4. WTN PROPAGATION.....	102
<i>Wind Turbine Acoustic Field</i>	102
<i>Ground Reflections</i>	103
4.5. NOISE PREDICTION RESULTS	105
5. CONCLUSIONS AND FUTURE WORK	108
REFERENCES	110
APPENDIX A: AERODYNAMIC <i>BEM</i> METHOD.....	118
APPENDIX B: AERODYNAMIC NOISE SOURCES	125
TURBULENT BOUNDARY LAYER-TRAILING EDGE NOISE (TBL-TE).....	125
SEPARATED FLOW NOISE (SF)	126
LAMINAR BOUNDARY LAYER-VORTEX SHEDDING NOISE (LBL)	126
TRAILING EDGE BLUNTNESS-VORTEX SHEDDING NOISE (TEB).....	127
TURBULENT INFLOW NOISE (TI)	128
AIRFOIL SELF-NOISE DIRECTIVITY.....	129
APPENDIX C: EIKONAL EQUATIONS SOLUTION	131
APPENDIX D: 4TH ORDER RUNGE-KUTTA HRT SOLUTION	136
APPENDIX E: NREL 5-MW BLADE PROPERTIES	140

LIST OF FIGURES

Figure 1.1: Global wind turbine installed capacity projections until the year 2020 (GWEC, 2016).....	1
Figure 1.2: Levelized cost of energy variation (\$/MWh) and wind turbine size evolution in time (Zayas et al., 2015).	2
Figure 1.3: Contours of instantaneous velocity in the vertical plane for three turbulence intensities (TI). The flows are obtained using a AL-LES technique (Barlas et al., 2017). .6	6
Figure 1.4: Noise components for 75 Kw Wind Turbine (Pinder, 1992).....	8
Figure 1.5: Schematic of flow over a wind turbine rotor blade (Wagner et al., 1996).	9
Figure 1.6: Refraction effects caused by temperature and wind changes in the atmosphere (Peng, 2014).	11
Figure 1.7: Hybrid FFP-PE propagation method developed by Rosenbaum (2011).	12
Figure 1.8: Measured and predicted excess attenuation for a MONOTPEROS 50 wind turbine at a distance of 530 meters (Prospathopoulos et al., 2005).....	13
Figure 1.9: Transmission loss for a frequency of 1 KHz. The source is monopole located at 300 meter height, a logarithmic wind profile and linearly decreasing temperature with height have been used (Tuinstra, 2014).....	14
Figure 1.10: Over all sound pressure levels with and without wake flow (Lee et al., 2016).....	16
Figure 1.11: Sound pressure level distribution at four distances around the Bonus 300 kW wind turbine (Wei Jun Zhu, Heilskov, et al., 2005).	16
Figure 1.12: Schematic used for wind turbine noise prediction model proposed by	17
Figure 1.13: WTNoise Framework including Hamiltonian ray tracing propagation (Wu, 2017).....	19
Figure 2.1: Rectangular and axisymmetric coordinate systems used for propagation (E. M. Salomons, 2001).	21
Figure 2.2: FFP Discrete atmospheric layers (E. M. Salomons, 2001).	23
Figure 2.3: Elevation angles for PE methods (E. M. Salomons, 2001).....	26
Figure 2.4: CNPE pressure domain grid (E. M. Salomons, 2001).....	27
Figure 2.5: 3D GFPE method coordinates (E. Salomons et al., 2011).....	33
Figure 2.6: Ray Propagation in Homogeneous Media (Jensen, 2011).	35
Figure 2.7: Ray Propagation in Inhomogeneous Media.	35
Figure 2.8: Unit vector $drds$ and $\nabla\tau$ during ray propagation.....	37
Figure 2.9: Sound Propagation Scheme over ground with impedance Z_g	39
Figure 2.10: Multiple ray reflection geometry.....	43
Figure 2.11: Upward refracted ray and shadow region formation.	44
Figure 2.12: Uneven 2D terrain profile implemented in Harmonoise (E. Salomons et al., 2011).....	51
Figure 2.13: Illustration of the Fresnel ellipse area for a sound ray departing from the source S and arriving to the receiver R above the reflecting plane (C. H. Hansen et al., 2017).....	52
Figure 2.14: Definition of geometrical parameters for circular ray paths in Nord 2000 (Plovsing, 2006).	53

Figure 3.1: Illustration of 2D Wave propagation in homogeneous media at a specific instant in time. Wavenumber vector and its components are shown as well as the wavelength components and wave fronts.	58
Figure 3.2: Representation of an acoustic wave traveling exclusively along the x direction for (a) acoustic pressure variation at time $t = \tau_0$, (b) acoustic pressure time variation at a location $x = x_0$	59
Figure 3.3: Homogeneous media's characteristic surface and curves.	64
Figure 3.4: Integral surface and characteristic curve over x, t, kx space.	67
Figure 3.5: Wind profile and propagating ray path components.	71
Figure 3.6: Absorption Coefficient [dB/100 m] in terms of frequency/pressure ratio [Hz/atm] for various relative humidity values at 20 degrees Celsius (Bass, 1995).	84
Figure 3.7: Attenuation effects on ray tube pressure amplitude between consecutive steps during propagation.	85
Figure 3.8: Ray reflection scheme over ground with impedance Z_G	87
Figure 3.9: Three rays propagated from a noise source located at 100 meter height using the numerical HRT technique and Analytical Eikonal approach.	89
Figure 3.10: Wind and temperature profile used in the simulations.	90
Figure 3.11: Monopole source OASPL noise maps for (a) HRT (4 th order RK and $\Delta t = 0.025$ s.) and (b) FFP numerical solutions.	91
Figure 3.12: Monopole source OASPL noise maps for Eikonal 4th order Runge-Kutta and time step of 0.025 [s].	92
Figure 3.13: Monopole source OASPL noise maps for (a) Eikonal 2 nd order Runge-Kutta and time step of 0.025 [s] and (b) Eikonal 4 th order Runge-Kutta and time step of 0.001 [s].	93
Figure 4.1: Wind Turbine Noise (WTNoise) modelling tool modules.	94
Figure 4.2: (a) Points on rotor plane for aerodynamic and noise calculation, (b) AoA for full rotation in a non-uniform flow, (c) noise source 4 spectrum computed by NAFNoise, (d) sound spheres array for the wind turbine blades, (e) Hamiltonian ray propagation (f) resulting OASPL noise map due to turbine at 48° azimuth position.	95
Figure 4.3: (a) Turbine top view showing yaw angle, (b) Turbine side view showing tilt angle, (c) Turbine side view showing blade cone angle (Wu, 2017).	96
Figure 4.4: WTNoise coordinate systems: (a) global and rotor coordinate systems, (b) airfoil coordinate system (c) directivity coordinate system on the airfoil element, (d) A baffled dipole sound spheres relative to the directivity coordinate system (Wu, 2017). ..	98
Figure 4.5: (a) Hub, blade and shaft coordinate systems for a wind turbine, (b) Blade deflection results for a NREL 5 MW wind turbine (Wu, 2017).	101
Figure 4.6: Ray tube triangular cross section area and vectors used for cross product.	102
Figure 4.7: Ray tube propagation from spherical source grid.	103
Figure 4.8: Ray tube ground reflections scheme.	104
Figure 4.9: NREL 5 MW wind turbine blade.	105
Figure 4.10: Equivalent Overall A-weighted sound pressure level noise map for one rotor revolution: (a) 2,562 and (b) 10,242 rays emitted by each of the 75 sound source.	106
Figure A.1: Annular control volume used for BEM method (M. O. L. Hansen, 2015).	118
Figure A.2: (a) BEM control volume flow velocities and (b) trailing edge velocity triangle for a single airfoil (M. O. L. Hansen, 2015).	119

Figure A.3: (a) Flow velocity components at airfoils leading edge and angles and (b) Forces acting on a single airfoil section (M. O. L. Hansen, 2015).	120
Figure B.1: Turbulent Boundary Layer-Trailing Edge Noise (Brooks et al., 1989).....	125
Figure B.2: Flow Separation Noise (Brooks et al., 1989).	126
Figure B.3: Laminar Boundary Layer-Vortex Shedding Noise (Brooks et al., 1989) ..	127
Figure B.4: Trailing Edge Bluntness-Vortex Shedding Noise (Brooks et al., 1989).....	127
Figure B.5: Airfoil-self noise directivity angles (Brooks et al., 1989).....	129

LIST OF TABLES

Table 2.1: Expressions for k , kz and $S\delta$ for rectangular and axisymmetric pressure domain (see equation (2.1)).	22
Table 2.2: Values for GFPE starting field parameters (E. M. Salomons, 2001).....	33
Table 3.1: Numerical atmospheric propagation methods including the Hamiltonian ray technique.....	55
Table 3.2: Ground impedance model alternatives to the Delany-Bazley model.	87
Table 3.3: Sound Pressure Level results over noise map grid for HRT, FFP and ERT methods.....	91
Table E.1: NREL 5-MW distributed blade properties (J. M. Jonkman et al., 2009).	140

1. INTRODUCTION

Wind power production has significantly increased during recent years. According to the *Global Wind Energy Council* (GWEC, 2016), global cumulative wind installed capacity is projected to rise up to 800 GW by the year 2020 (see Figure 1.1). In addition, the annual installed capacity growth rate is set between 5% and 6% in the near future.

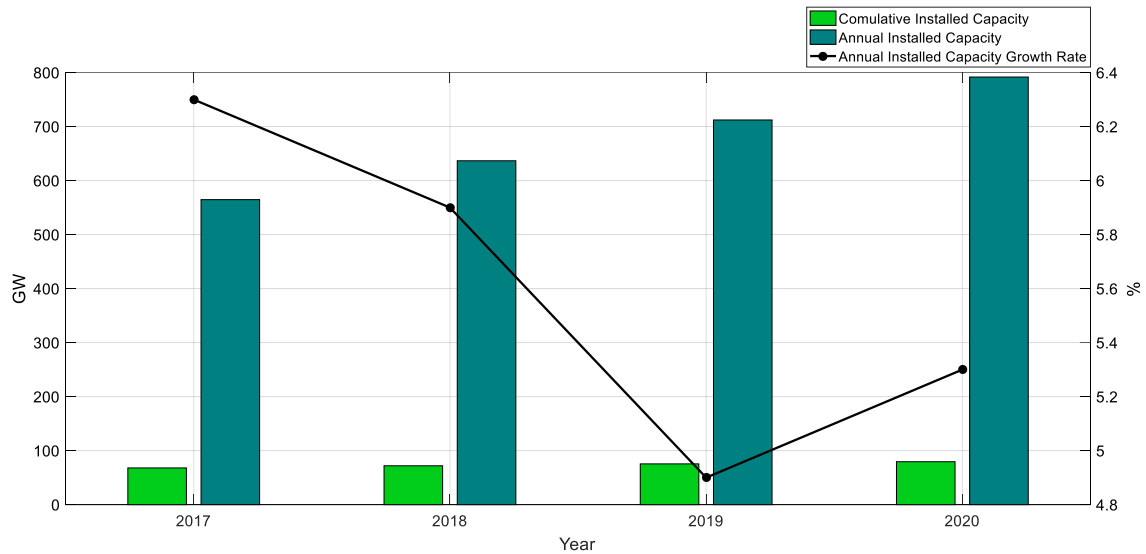


Figure 1.1: Global wind turbine installed capacity projections until the year 2020 (GWEC, 2016).

According to Zayas et al. (2015), the total cost of wind turbine energy production depends on the initial capital costs, recurring annual operations and maintenance expenses, and net energy collected (energy production drives annual revenue). As shown in Figure 1.2, costs are reduced by increasing the energy production per wind turbine. That is, by designing wind turbines with larger rotor swept area and hub height. Therefore, future wind turbines are projected to increase their size to achieve greater power outputs, higher efficiency, and profitability. However, this also means that their environmental impact is set to become more substantial. Consequently, most of onshore wind turbines are subjected to noise constraints and regulations that are ever more stringent.

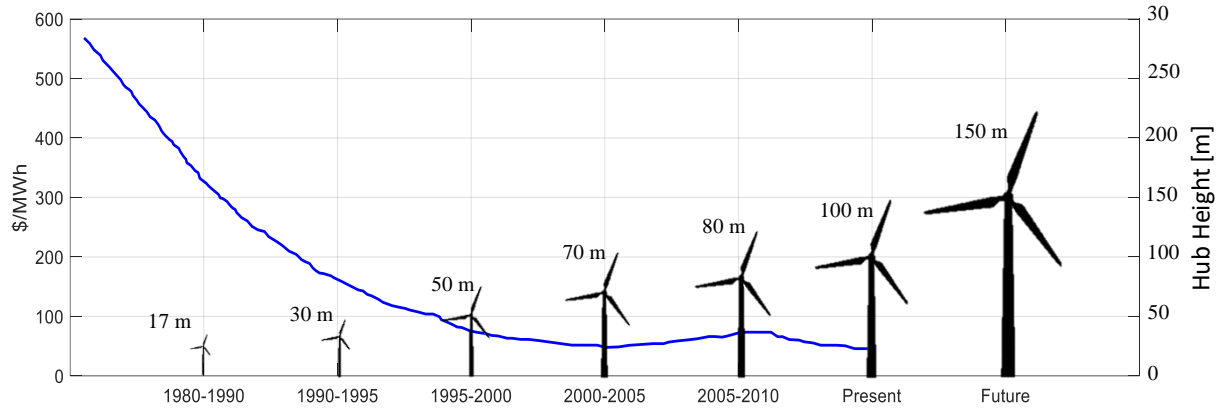


Figure 1.2: Levelized cost of energy variation (\$/MWh) and wind turbine size evolution in time (Zayas et al., 2015).

Dominant wind turbine noise (WTN) is aerodynamically produced and is responsible for an observed amplitude modulation (AM) phenomenon. Broadband noise levels fluctuate significantly along crosswind directions, which is usually referred to as “swishing”, “whooshing” or “pulsating noise” (Bowdler et al., 2012). This is the result of the blade experiencing different aerodynamic conditions (e.g. angle of attack) over a rotor revolution due to wind vertical shear and/or crosswinds. The modulation happens at the blade pass frequency, and its amplitude typically fluctuates between 3 to 5 dBs. Periods of increased swishing have also been reported and referred to as Enhanced Amplitude Modulation (EAM). In this case, the sound variation is usually larger than 6dB and can be perceived at large distances in both downwind and upwind directions. Still, the mechanism for EAM is not clear and potential causes have been attributed to wind shear, yaw error, blade-tower interaction and interference between various wind turbines in a farm (Oerlemans, 2011). These distinctive types of noise are propagated towards neighboring residential areas and is considered the principal cause of reported annoyance (van den Berg, 2005). Other factors such as the quiet rural environment, turbulence of the wind directed into the turbine and at its wake, and the low frequency dominance are the principal sources of perceived annoyance as well.

New wind turbine designs have to meet local and international regulations. Most countries specify the upper allowed sound power noise bounds to be within a range of 30-50 dBA in rural and residential areas (Wagner et al., 1996). Furthermore, before going into production, new designs have to comply various noise guidelines according to the IEC 61400 standard. This is a standard

developed by the International Electrotechnical Commission and two of its sections address noise. IEC 61400-11 specifies wind turbine acoustic measurement techniques and IEC 61400-14 provides with guidelines for apparent sound power levels and their tonality. Measurements according to this standard provide accurate and replicable data only for the near field (Raman, 2016). Even though not specified in any standard, more sophisticated measurements can be performed using microphone arrays and applying beamforming techniques (Oerlemans et al., 2007). This type of measurements are used for source localization during wind turbine operation and developing methods to mitigate amplitude modulation, as proposed by Buck et al. (2013).

There is a need for accurate and cost effective tools that improve WTN predictions over relatively large distances (a few kilometres) around wind turbine farms. Thus, precise turbine noise models that include comprehensive propagation methods must be developed. Currently, noise propagation models are classified as engineering, semi-analytical, or numerical approaches (Bowdler et al., 2012). The first one refers to standards such as ISO 9613-2 and commercial software models like Nord2000, Harmonoise, Concawe and so forth. Even though their degree of sophistication has risen on recent years, they still rely on simplified models where neither actual turbine radiation characteristics, nor real meteorological conditions are taken into account (Plovsing, 2006). Analytical approaches consist of acoustic wave analytical solutions limited to 2D media, where the speed of sound has a linear variation. In this case, acoustic rays follow a circular path under upward or downward refraction (Bérenghier et al., 2003). Finally, numerical methods are based on solutions to multiple forms of the Helmholtz equation or on ray tracing techniques. These methods have proven to be highly accurate for 3D noise propagation, however they still have some simplifications and are computationally very intensive (E. M. Salomons, 2001).

This thesis presents the developments of a Hamiltonian Ray Tracing (HRT) technique coupled to a state of the art WTN prediction tool called WTNoise. This tool is capable of computing aeroacoustic noise sources along the blades based on their design, work specifications, and environmental conditions. The HRT propagation technique tracks the acoustic wave phase behavior as rays travel through the atmospheric media (Lighthill, 1978). It avoids the drawbacks presented by other numerical approaches such as parabolic equation solutions, Fast Field Program, and the traditional Eikonal ray tracing (E. M. Salomons, 2001). Furthermore, it is capable of taking

into account real temperature, wind speed, and humidity variations in a three-dimensional grid over the atmosphere. This is especially important when analyzing noise behind complex flows such as those located at a wind turbine wake. The simplicity of the equations that have to be solved in order to capture ray bending due to refraction is one of the major advantages from this method. This allows maintaining relatively low computational time while running predictions.

1.1. WIND TURBINE NOISE MODELING REVIEW

Modeling wind turbine noise is a complex task. The dynamic behavior of the turbine has to be coupled to noise sources induced by the flow around the blades. In addition, propagation models have to be implemented in order to predict noise over large distances. In this section, the most relevant components for WTN modeling are described. A review on wind turbine aerodynamics and aeroelasticity is included. An introduction to WTN mechanisms is also addressed. Finally, a review on the most innovative propagation methods and complete WTN techniques found in literature is presented.

Aerodynamic Analysis

Characterizing the flow around a wind turbine constitutes one of the most important tasks when building a WTN model. Various aerodynamic parameters influence how aeroacoustic noise sources are generated and how noise propagation behaves. There are several methods available for modeling aerodynamic effects. The most popular one is the *Blade Element Momentum* (BEM) approach. It combines one dimensional momentum theory approach with flow estimations over single blade elements along the blades. Each blade element cross-section is considered to have independent geometric characteristics. This method provides a convenient approach to estimate local angles of attack during blade rotation. Furthermore, it is easy to increase prediction accuracy. For example, corrections due to the vortex system in the wake or inaccuracies in the momentum theory can be addressed by including empirical Glauert corrections (M. O. L. Hansen, 2015). Additional considerations such as dynamic wake, dynamic stall and yaw models can also be used to complement BEM computations. A theoretical description of the BEM methods is included in Appendix A.

Three-dimensional inviscid aerodynamic models can also be implemented in order to characterize the flow around a wind turbine. These type of approaches are limited because they ignore fluid viscosity. However, they provide an appropriate insight on the flow characteristics. *Vortex Methods* model vortices formed at the blades due to bound flow circulation depending on the produced lift. This type of models are very simplistic, however, they have proven valuable for validating momentum theory as shown in the work of Miller (1983). *Panel Methods* define the flow past the blades by defining disturbance sources over the blade surface. The flow field is then defined for an initial singularity and expanded over the domain using Green's theorem. For horizontal wind turbines, this approach is used in the work by Coton et al. (1999).

The *Actuator Disc* technique is fundamental for developing momentum theory. Combining it with blade element analysis leads to BEM models. However, it can also be used with Euler and Navier-Stokes equations. In that case, the numerical equations are solved via common finite difference/volume techniques. Still, neither the geometry of the blades nor viscosity are taken into account. In its place, the area swept by the blades is taken into account by incorporating surface forces that act on the incoming flow. This method has proven accurate only for axisymmetric flow as shown in the work by Masson et al. (2001) and Behrouzifar et al. (2015). Recently, an extended three dimensional actuator disc model has been developed. It is often referred to as a *Line Actuator*. 3D Navier-Stokes equations are solved in combination of a model where the rotor blade forces are radially distributed. Airfoil data and loading is computed iteratively by calculating angles of attack while the rotor is moving as done by Sørensen et al. (2002). This method provides the capability to reproduce detailed dynamics of the wake, tip vortices and their influence on induced velocities on the rotor plane. Actuator methods are useful when implementing wind turbine noise propagation solutions. Barlas et al. (2017) implemented a Line Actuator combined with Large Eddy Simulation technique to predict the wake flow behind the wind turbine. In addition, their work was coupled to a parabolic equation propagation method for noise prediction. As observed in Figure 1.3, the flow at the wake of the wind turbine is altered for more than a kilometer behind the wind turbine, even for various turbulent incoming flows.

Navier-Stokes (NS) solvers are also implemented for wind turbine applications. Given that flow over the rotor blades is usually incompressible and has very low Mach numbers, it is not

convenient to implement compressible flow solvers. However, these still have some advantages such as the ease of implementing different types of meshes and capable of handling high order upwind schemes. On the other hand, if incompressible flow solvers can also be used, where pressure is generally treated as the primary variable. Implementing NS with turbulent inflow for wind turbine applications is usually done via Reynolds Averaged NS equations (RANS). Most of wind turbine aerodynamic applications using CFD have focused on a case where there is zero yaw rotor and both the tower and nacelle are neglected (M. Hansen et al., 2006).

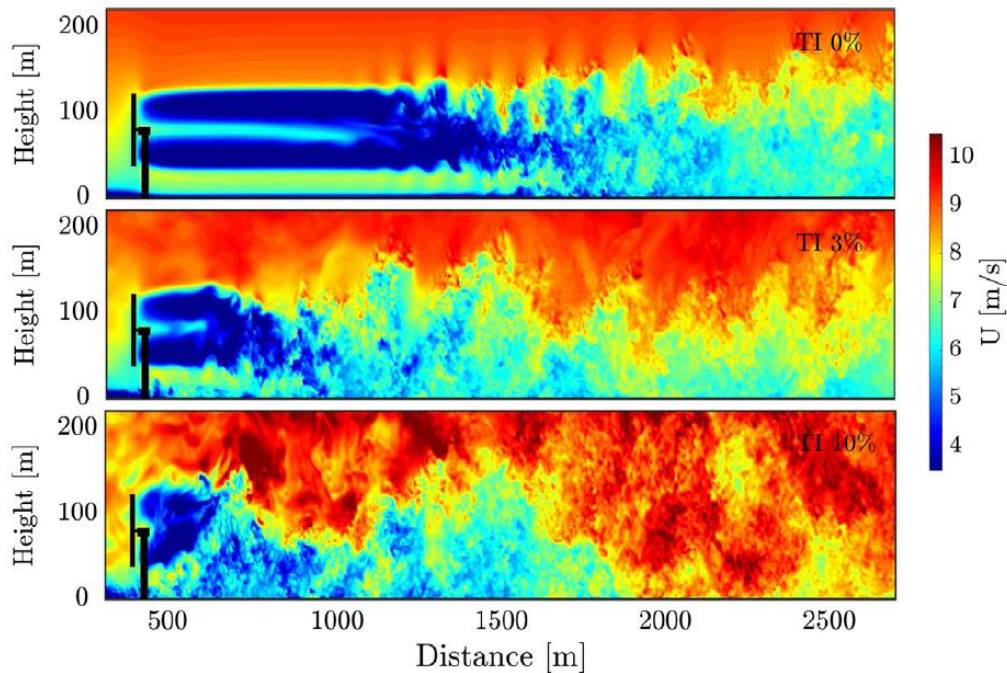


Figure 1.3: Contours of instantaneous velocity in the vertical plane for three turbulence intensities (TI). The flows are obtained using a AL-LES technique (Barlas et al., 2017).

Aeroelastic Simulation

The main aeroelasticity simulation codes available in literature for wind turbine applications are FAST and HAWC2. FAST is considered as one of the most popular (Wu, 2017). It is a driver code that integrates several modules in order to simulate wind turbine operations. The capabilities of this code includes analyzing structural responses of the blades, tower, and platform under arbitrary weather conditions (J. M. Jonkman et al., 2005). Aerodynamics are computed using a BEM method and then coupled to blade aeroelasticity computations using Geometrical Exact Beam theory

(GEBT). T. Kim et al. (2014) performed a comparison between simulation and measurements of an Envision two-bladed 3.6 MW wind turbine. Only edgewise and flapwise blade bending moments were used for comparison, showing good agreement with measurements. Guntur et al. (2016) on the other performed a full dynamic analysis on a Siemens 2.3 MW wind turbine and compared the results to FAST and a code developed by Siemens called BHawC. It was concluded that the latest version of FAST (v8) agrees very well with the measured data and has considerably improved from previous versions.

HAWC2 on the other hand implements a multibody formulation of the wind turbine blades and its tower by using Timoshenko beam elements. Aerodynamics are implemented via an improved BEM approach. In addition, this code is also capable of taking into account various inflow conditions for simulations (Larsen et al., 2007). Shirzadeh et al. (2015) measured the structural natural frequencies of the structure of a 3MW Vestas V90 offshore wind turbine. Simulations for this turbine were also performed using HAWC2. The predictions seemed to overestimate the structural vibration levels even though the simulation trends had good agreement with the measurements.

QBlade is an open source software package used for blade design with application to wind turbines (Marten et al., 2013). This program covers only aerodynamics of wind turbines with enhanced BEM methods including blade twist, curvature and chord optimization of the blades. It integrates XFOIL (Drela et al., 2001), that calculates that lets the user extrapolate polar data for a range of 360 degrees. Finally, QBlade incorporates FAST during simulation in order to perform aeroelasticity computations.

Wind Turbine Noise Sources

Aerodynamic and Mechanical noise sources are the two components of wind turbine noise. Mechanical noise originated from different machinery located at the wind turbine's nacelle and transmitted to all structural components. The main machinery element sources are the gearbox, generator and cooling fans. However, this type of noise sources can be efficiently prevented and treated. The noise spectrum from a 75 Kw wind turbine is shown in Figure 1.4. It is observed that aerodynamic rotor noise is dominant up to 2 kHz. Tower noise has low sound power levels and

the nacelle sound powers are low except for a tone at about 2.5 kHz. However, vibration insulation techniques can lead to the reduction of the nacelle noise up to 15 dB (Pinder, 1992). Thus, aerodynamic noise is the dominant noise component for wind turbines.

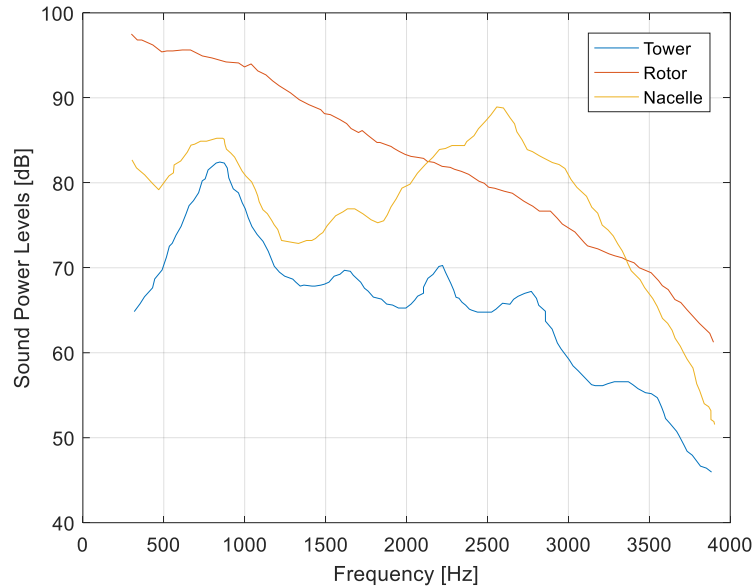


Figure 1.4: Noise components for 75 Kw Wind Turbine (Pinder, 1992).

Aerodynamic noise is generated by both natural turbulence of the inflow and transitions from laminar to turbulent boundary layers close to the trailing edge of the blades. The flow near the leading edge is accelerated and then decelerated on the blade surface. This, combined with an increased pressure gradient induces thicker boundary layers and eventually flow separation. On the other hand, tip vorticity is associated to the pressure difference between the pressure and suction sides of the blades.

Low frequency noise is caused by the interaction of the rotor blades as they encounter the tower. The tower's cylindrical cross section alters the flow around it causing local changes in the blade's aerodynamics. The fluid fluctuations produced by this phenomenon turn into dipole like noise and can be characterized via Ffowcs Williams-Hawkings equations. The dominant frequency for this noise mechanism is related to the blade pass frequency; however, after A-weighting the wind turbine noise only minor contributions are left. This is not a critical wind turbine noise mechanism (Wagner et al., 1996).

The most significant aerodynamic noise from a wind turbine comes from airfoil-self noise. Five different airfoil self-noise mechanisms have been identified. They are turbulent boundary layer-trailing edge noise (TBL-TE), separation stall flow noise (SSF), laminar boundary layer noise (LBL), trailing edge bluntness noise (TEB), and turbulent inflow noise (TI). Each of them are shown Figure 1.5 and briefly listed below:

1. Turbulent boundary layer-trailing edge noise (TBL-TE) is generated by the interaction of turbulent eddies at the trailing edge.
2. Separation stall flow noise (SSF) is caused by flow separation at specific angles of attack and Reynolds numbers. Its radiation is along the entire chord length.
3. Laminar boundary layer noise (LBL) is caused by vortex shedding at the trailing edge. It usually manifests as pure tones, generated by the interaction of the shed vortices and instability waves in the laminar boundary layer.
4. Trailing edge bluntness noise (TEB) generates due to vortex shedding. The frequency and amplitude of the noise is defined by the airfoil bluntness.
5. Turbulent inflow noise (TI) is caused by the interaction between the inflow and leading edge. It becomes more prominent when turbulent inflow eddies are large.

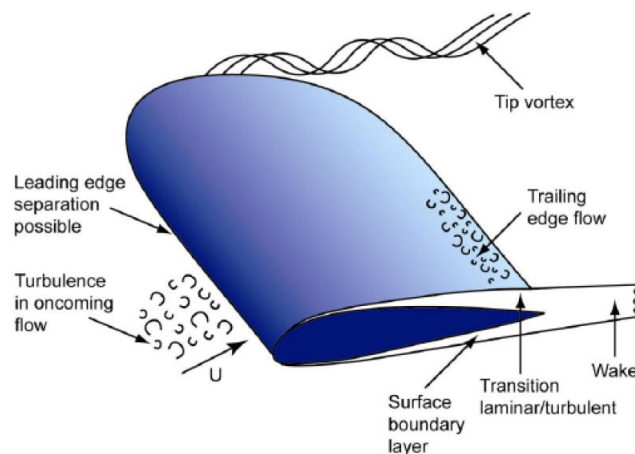


Figure 1.5: Schematic of flow over a wind turbine rotor blade (Wagner et al., 1996).

The TBL-TE, SSF, LBL, and TEB are known as airfoil self-noise. Semi empirical noise solutions to these mechanisms were developed by Brooks et al. (1989). On the other hand, Amiet (1975) and Patrick Moriarty et al. (2005) developed methods to solve for TI noise.

Airfoil self-noise can be predicted for individual airfoils using the code NAFNoise, which stands for NREL Airfoil Noise. The predictions made by this software are based on empirical models developed from research at the National Renewable Energy Laboratory (P Moriarty, 2005). NAFNoise predicts noise produced by any airfoil geometry under a specified angle of attack. The results are presented for each airfoil self-noise mechanism sound pressure levels in 1/3rd octave frequency bands, at a user specified location. The program permits boundary layer computations to be carried out by using Xfoil routines developed by Drela et al. (2001) or by directly using Brooks et al. (1989) semi empirical relations. For this reason, NAFNoise can be implemented within wind turbine noise modeling. All the airfoil self-noise modeling empirical formulation used by NAFNoise and a more thorough physical explanation of them can be found in Appendix B.

Atmospheric Noise Propagation

Atmospheric noise propagation depends on several factors. Wind and temperature distributions affect the path followed by acoustic waves in space due to refraction phenomena. Figure 1.6 shows this behavior under increasing and decreasing temperature with height, and uniform wind. In addition, ground reflections are affected by the terrain characteristics including geometric distribution and absorption. Finally, atmospheric attenuation also has to be taken into account.

There are several approaches for propagation computation. These include numerical, analytical and engineering methods. Numerical approaches include the following: Fast Field Program (FFP), Parabolic Equation Methods (PE), and Ray Tracing. On the other hand, analytical solutions encompass a geometric ray tracing approach. Finally, engineering methods use very simplified acoustic wave and ray solutions. The theoretical development of all these techniques is presented in Chapter 2.

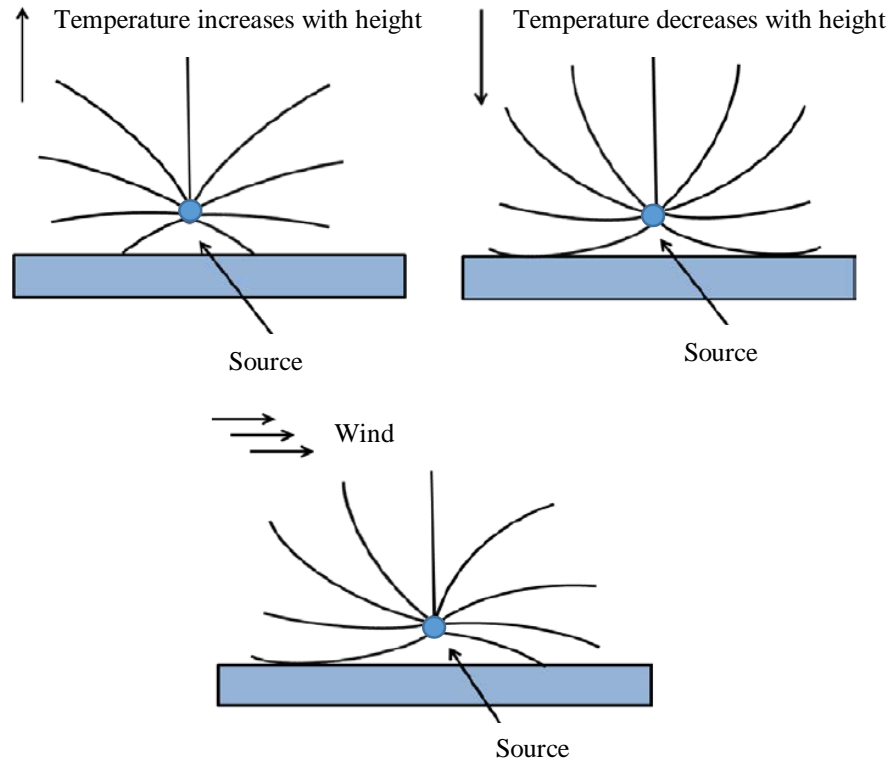


Figure 1.6: Refraction effects caused by temperature and wind changes in the atmosphere (Peng, 2014).

According to Peng (2014), even though a ray tracing method has the advantage of realistic rendering of wave paths, mathematical singularities or caustics are always present. Additionally, it is limited to high frequency applications only. On the other hand, FFP or Fast Field Program the media is assumed to be stratified. Parabolic equation methods are not limited to layered media as FFP, however they are computationally inefficient and inaccurate at large elevation angles (angle between propagation direction and a horizontal plane). For this reason, new propagation methods that avoid these setbacks are needed.

Rosenbaum (2011) approached the propagation problem by implementing a hybrid FFP-PE method. In this case, a PE method was used for elevation angles between 0 and 35 degrees. For the rest of points on the grid an FFP method was used as shown in Figure 1.7. All calculations were performed in 2D. Even though, this approach produced accurate results it still showed to be computationally intensive. In addition, propagation effects such as noise levels over shadow regions were not investigated further. On the other hand, Cheng (2007) developed a new parabolic method coded for inhomogeneous arbitrary moving atmosphere. A novel formulation of the

Helmholtz equation in three-dimensional cylindrical coordinates was used in this work. In this case, discretization using Crank Nicholson finite difference was solved using a Generalized Minimum Residual Method (GMRES) method. For validation purposes, a standard two-dimensional Crank Nicholson Parabolic Equation (CNPE) method was also implemented.

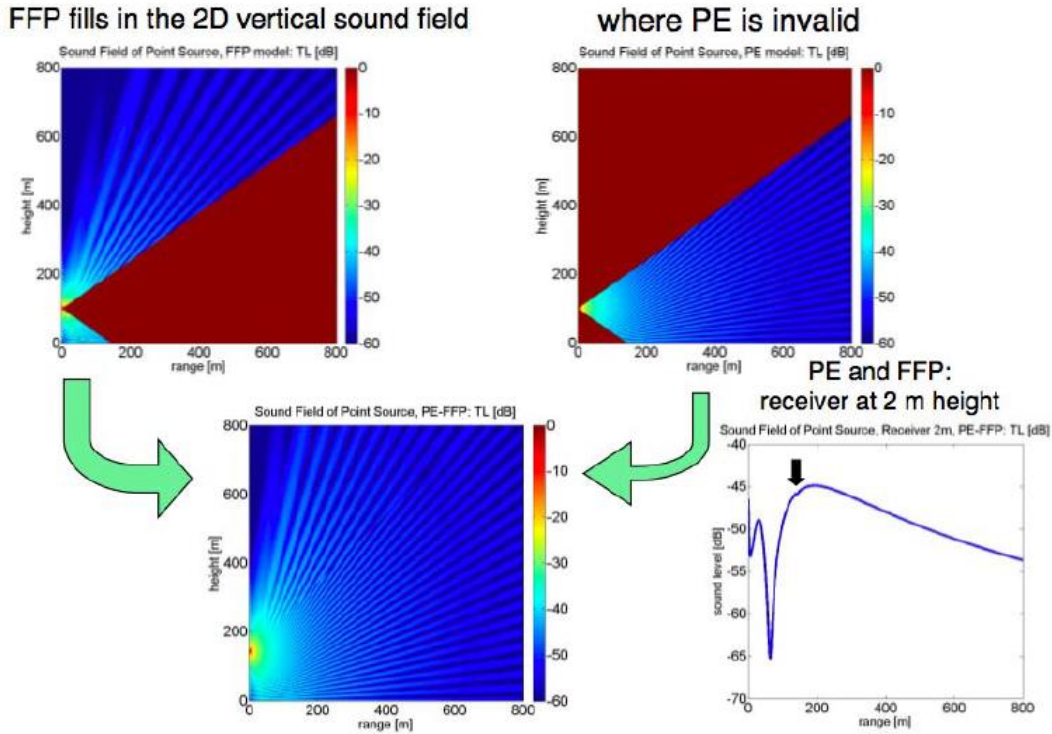


Figure 1.7: Hybrid FFP-PE propagation method developed by Rosenbaum (2011).

E. M. Salomons (1998) identified and addressed four types of numerical errors associated to Green’s Function Parabolic Equation (GNPE) method. These are errors associated to the forward and inverse Fourier transforms, errors in refraction factors, and errors caused by numerical split-step approximations. The improvements applied to this method reduced errors from 50 dB to 0.1 dB, according to the author. Parabolic equation methods implementing finite element solvers have also been developed. Kampanis et al. (2001) implemented a PE technique in cylindrical coordinated over a varying ground surface using various finite element discretization schemes including the Crank-Nicolson Galerkin one. Other cases where PE methods have been addressed can be found in the work by Johansson (2003), Mylonas (2014), and Bolin et al. (2009).

Prospathopoulos et al. (2005) applied ray tracing for propagation of wind turbine noise. An Eikonal

ray tracing approach was used to predict noise propagation from a 1MW MONOPTEROS 50 wind turbine. For example, excess attenuation at a distance of 530 meters was computed with and without refraction effects, and compared to measurements. The results agreed well, as show in Figure 1.8. According to the author, the numerical integration for the ray paths had higher computational efficiency because instead of a Runge-Kutta method (Hairer, 2008), a Bulirsh-Stoer integration technique was used.

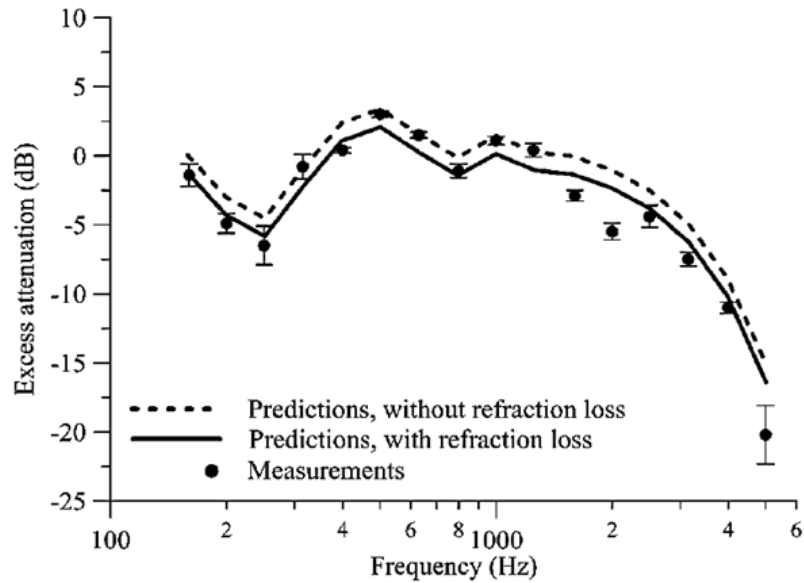


Figure 1.8: Measured and predicted excess attenuation for a MONOTPEROS 50 wind turbine at a distance of 530 meters (Prospathopoulos et al., 2005).

The Eikonal approach is the most popular technique for ray tracing applications as shown in the work by Virieux et al. (2004), Huber et al. (2002), and (Lamancusa et al., 1993). The equations for this method can be solved numerically using the method of characteristics (Brouwer, 2014). Tuinstra (2014) solved an Eikonal ray tracing technique and showed the formation of a shadow region over the upwind area with respect to the noise source, as shown in transmission loss map in Figure 1.9. On the other hand, Iomin et al. (2003) provided insight on the sensitivity of ray paths to initial conditions. Ray tracing techniques including a finite element approach have also been addressed by Porter et al. (1994). Initial Hamiltonian approaches to ray tracing propagation were developed by Chessell (1973) and Lighthill (1978). This methods were applied to both atmospheric and ocean noise propagation (Georges et al., 1986). According to Koyanagi et al.

(2008) the advantage of the Hamiltonian approach is that ray propagation can be studied under numerous circumstances including ray chaos in a similar manner as is done for many dynamical systems with chaotic properties.

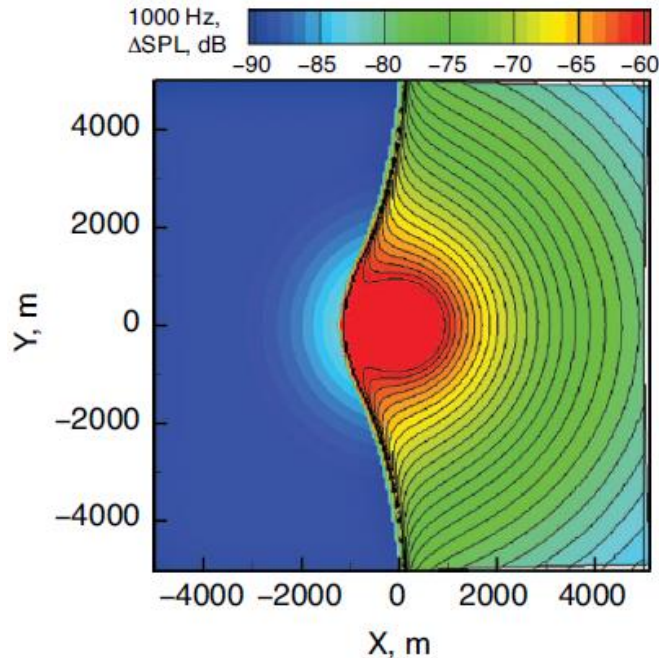


Figure 1.9: Transmission loss for a frequency of 1 KHz. The source is monopole located at 300 meter height, a logarithmic wind profile and linearly decreasing temperature with height have been used (Tuinstra, 2014).

Propagation using simplified engineering approaches usually provide inaccurate results. Kaliski et al. (2011) compared results obtained with CNPE and ISO9613. The wind turbine was assumed a monopole source producing a fixed sound power of 105dB for all 1/3rd octave frequency bands. The objective of this study was to suggest adjustments to a common engineering prediction method such as ISO 9613. Furthermore, the work by Forssén et al. (2010) included the results for measurements, standard PE approach, and NORD 2000. All measurements followed the procedures specified in IEC 61400-11 on a 1.5 MW Enercon E66 wind turbine. Simulations showed that PE methods are sensitive to turbulence, ground roughness and interference between direct and reflected waves, while Nord 2000 is not. Thus, proving that PE methods can predict noise more accurately over physically accurate environments. In addition, it was concluded that the influence of wind in the overall propagation is minimal, even when PE and NORD 2000 methods are compared; however, the wind strongly affects the source's strength.

Finally, propagation has also been solved using Linearized Euler Equations (LEE). Bailly et al. (2000) linearized around a known stationary mean flow and then computed the solution by using a dispersion scheme combined with a fourth order Runge-Kutta method. Still, these methods are restricted to simple meteorological conditions i.e. linear speed of sound profiles (Hornikx et al., 2010). Cotté et al. (2009) compared the propagation results of a pressure pulse between the LEE and a PE method.

Wind Turbine Noise Prediction Models

Developing a comprehensive wind turbine noise prediction tool is a complex task. An aerodynamic and aeroelastic analysis has to be included and coupled to all wind turbine noise mechanisms. Furthermore, a suitable propagation method has to be selected in order to predict accurately noise over large distances. All this while maintaining the highest possible computational efficiency. A review of existing wind turbine prediction models is addressed in this section.

Peng (2014) predicted noise for a wind turbine by implementing an Actuator-Line-Large Eddy Simulation method to simulate the wake form. Once the flow is known, a novel PE method that implements a finite element analysis using a cubic discretization is used. However, the starting field simulating a wind turbine corresponds to a monopole source. Lee et al. (2016) implemented a similar approach by running a RANS CFD simulation to compute the wake flow and a CNPE technique for propagation. Figure 1.10 shows the reported overall sound pressure levels for cases considering a wake with mild wind shear and without wake.

On the other hand, W. J. Zhu (2004) and Leloudas et al. (2007) implemented a BEM approach coupled to the semi-empirical formulation for airfoil-self noise mechanisms developed by Brooks et al. (1989). In addition, optimization strategy tools for the turbine's operational settings as a function of noise production were developed. W. J. Zhu (2004) implemented atmospheric noise propagation in his work, however linear theory was used (linear speed of sound profile) and in order to improve accuracy the location of the source and receiver were altered (Wei Jun Zhu, Sørensen, et al., 2005). An example of the overall SPL distribution around a Bonus 300 kW wind turbine using this method is shown in Figure 1.11.

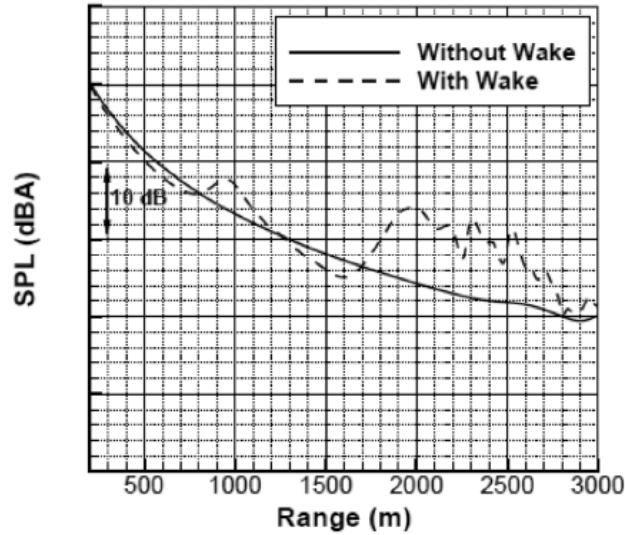


Figure 1.10: Over all sound pressure levels with and without wake flow (Lee et al., 2016).

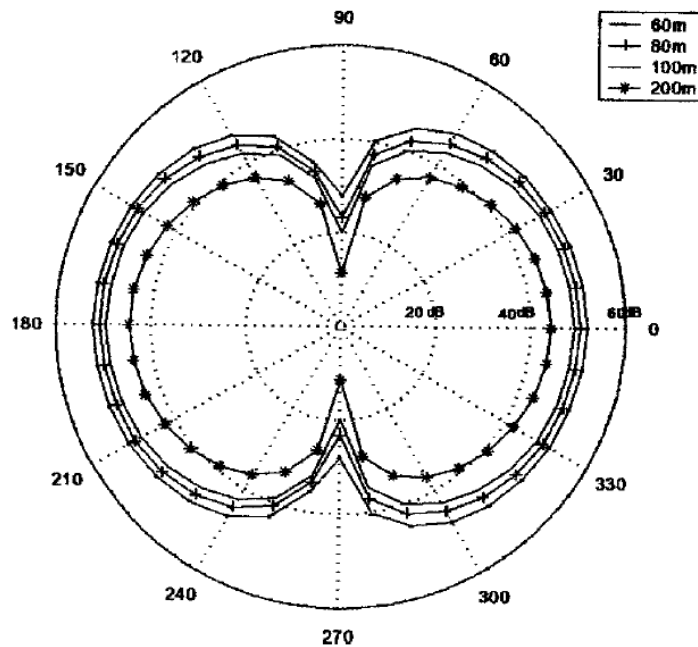


Figure 1.11: Sound pressure level distribution at four distances around the Bonus 300 kW wind turbine (Wei Jun Zhu, Heilskov, et al., 2005).

Cheng (2007) proposed a wind turbine noise modeling tool that follows the sketch shown in Figure 1.12. First, flow field simulations are conducted to obtain pressure distribution data on the wind turbine blades. Then, near field noise is predicted using PSU-WOPWOP (Goldman, 2013), which is a CFD code that also implements Ffowcs Williams-Hawkings equations for airfoils self-noise computation. Finally, long-range sound propagation is implemented using a parabolic equation method.

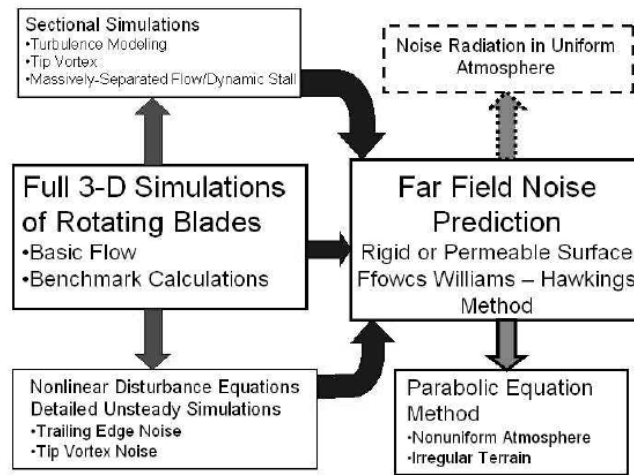


Figure 1.12: Schematic used for wind turbine noise prediction model proposed by .

The work by Cheng (2007) includes atmospheric absorption following ANSI S1.26. On the other hand, according to the author, turbulent flow in the atmosphere cause amplitude fluctuations of around 6 dB. Ground reflections are treated as one of the following cases: (a) internal ground waves are assumed to propagate only in a perpendicular direction relative to its surface; (b) The ground is treated as isotropic media that has the capability of transmitting dilatational waves in any direction, and (c) The ground is treated as an elastic solid having behavioral characteristics such as dilatational and shear waves. An Impedance Mismatch Method is also introduced for irregular terrains by introducing an interface layer between the atmosphere and ground with its own properties.

Son et al. (2010) implemented a similar approach, where the flow around the wind turbine is computed using the Wind Turbine Flow, Aeroacoustics and Structure Analysis (WINFAS) code. The flow analysis results are then used to predict tonal noise, turbulence inflow noise and airfoil self-noise. According to the authors, the tone noise is induced by the displacement of fluid and pressure fluctuations around the blade’s surface (thickness and loading noise). In addition, the proposed model takes into account uneven terrain for predictions. H. Kim et al. (2012) included nonlinear composite beam theory to analyze the rotor structural aeroelasticity in this research study. Noise results for a 1.5 MW RB70 wind turbine were compared for both rigid and flexible blades. It was predicted that the sound pressure levels were higher for the flexible blade case near the rotor center location. Finally, Arakawa et al. (2005) and Wasala et al. (2015) computed the

flow around a wind turbine using Large Eddy Simulation (LES) and then coupled the results to Ffowcs-Williams equations for aeroacoustic noise predictions. None of the wind turbine noise prediction methods mentioned above implemented atmospheric propagation in their simulations.

1.2. THESIS OBJECTIVES

The aim of this thesis is to develop an atmospheric noise propagation method suitable for noise produced by wind turbines. Real meteorological conditions must be incorporated in the model. These include atmospheric temperature and relative humidity distributions, as well as wind velocity. In addition, characteristic ground impedance and terrain roughness are of interest. The model should be capable of accurately computing acoustic wave refraction during propagation, as well as atmospheric attenuation and ground reflections. A Hamiltonian ray tracing approach will be implemented due to its numerous advantages over other methods.

A second goal of this thesis is to integrate the propagation model to the WTN modeling tool *WTNoise*. A scheme that shows the main framework of this tool is shown in Figure 1.13. It incorporates either a stand-alone *AeroDyn* (J. M. Jonkman, Hayman, G.J., Jonkman, B.J., Damiani, R.R., Murray, R.E. , 2017) or *FAST* (J. M. Jonkman et al., 2005) in order to compute the turbine's aerodynamic parameters (angles of attack and inflow wind speeds) for rigid or elastic blades, respectively. Wind turbine airfoil self-noise is then computed using *NAFNoise* (P Moriarty, 2005). Finally, the innovative Hamiltonian propagation model is coupled for propagation over large distances. The proposed approach for WTN prediction requires to be computationally efficient, particularly regarding the propagation module.

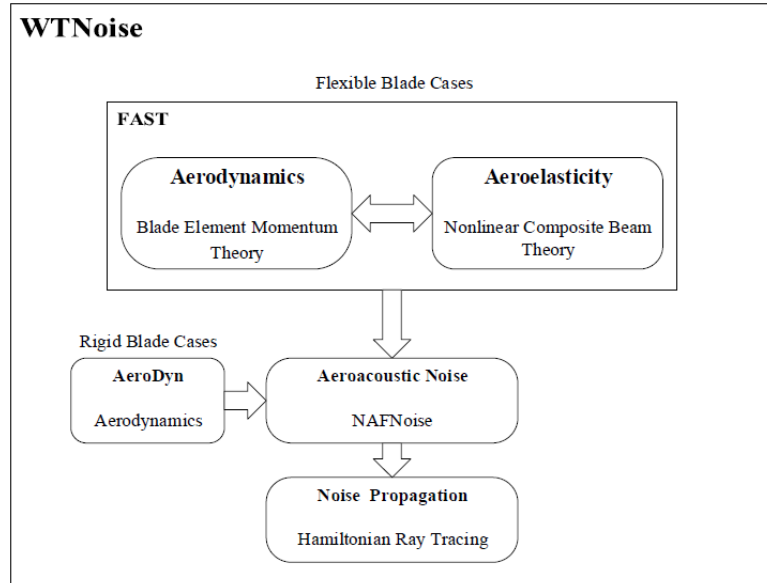


Figure 1.13: *WTNoise* Framework including Hamiltonian ray tracing propagation (Wu, 2017).

The propagation technique has to comply with the following: i) unlike analytical solutions, the media's temperature distribution cannot be limited to linear profiles (these type of conditions do not agree with reality); ii) Propagation equations have to avoid approximations such as effective speed of sound, used by many numerical propagation methods (wind velocity must be fully taken into account; even its vertical component); iii) Computational efficiency must be acceptable while maintaining high accuracy levels; iv) It has to be capable of predicting noise over a 2D and 3D domain (this is very important for propagation along the turbine's wake, where the flow is complex and includes vertical wind components that cannot be ignored); All these conditions guarantee precise physical interpretation of the atmospheric propagation scenario and leverage over other common techniques.

The scope of this study will be on propagation of noise produced by modern wind turbines with blade span ranges from 60 to 100 meters. The turbine's average noise will be predicted over its rated conditions. Aerodynamic effects caused by the interaction of the rotor and tower will be ignored. In addition, the foundation, tower and nacelle will be assumed rigid. Even though the developed propagation technique will be capable of handling turbulent flows and vertical wind components, the presented results will not include such cases. Turbulent inflow and wake computations are not part of the scope of this thesis. The wind considered for simulations will

consist of a steady vertical shear profile. In addition, uneven terrain will not be considered and it will be assumed acoustically homogeneous.

1.3. THESIS ORGANIZATION

The structure of this thesis is the following. Chapter 1 provides background information and introduces the WTN problem. It gives a brief literature summary on state-of-the-art noise models implemented on WTN predictions. In addition, the objectives of this work are presented. Chapter 2 addresses the theory of current noise propagation tools and methods. It is divided in analytical and numerical techniques, as well as approaches taken by commercial software. Chapter 3 is dedicated to the description of the developed HRT propagation code. It specifies the methods used to trace acoustic ray paths and acoustic energy in 2D and 3D space. Validation cases are also included. Chapter 4 describes the developed tool *WTNoise* used to compute, including propagation WTN prediction results. Finally, Chapter 5 provides a set of insightful conclusions and future work suggestions.

2. ATMOSPHERIC NOISE PROPAGATION MODELS

This chapter will address the most relevant atmospheric noise propagation techniques suitable for WTN prediction over large distances. This chapter is divided in three sections. First, current numerical propagation solutions will be covered. Section 2.2 will address analytic solution methods. Finally, section 2.3 will cover methods used in commercial software or commonly referred to as Engineering Methods (Bowdler et al., 2012).

2.1. NUMERICAL METHODS

A brief theoretical review of the most common propagation numerical approaches found in literature is presented in this section. These are, FFP, CNPE, GNPE and the traditional Eikonal ray tracing approach.

Fast Field Program (FFP)

Fast Field Program (FFP) is a numerical sound propagation method where the atmospheric media is divided into layers. Each layer is composed of a homogeneous wavenumber distribution. Meteorological conditions such as wind and temperature are taken into account by using vertical profiles. A homogeneous ground impedance can also be included. In order to calculate a propagating sound field, this method implements a solution to a generic form of the acoustic Helmholtz equation in the wavenumber domain. This permits to obtain sound fields in terms of axisymmetric (in terms of r and ϕ) or rectangular coordinates (x, y, z) . In both cases, the origin is set below the noise source on the ground surface as shown in Figure 2.1 (E. M. Salomons, 2001).

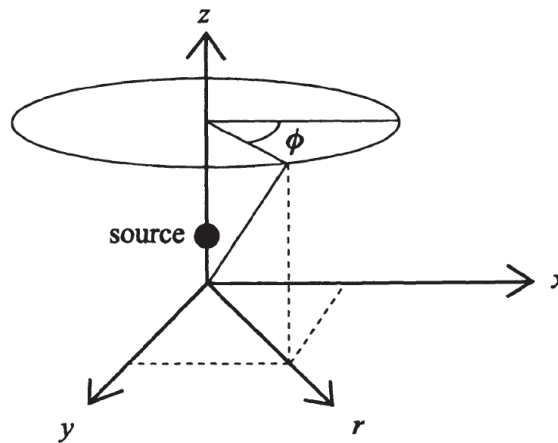


Figure 2.1: Rectangular and axisymmetric coordinate systems used for propagation (E. M. Salomons, 2001).

The initial step taken by the FFP method is to define the Helmholtz equation depending on the coordinate system used for simulations. A generic form of the Helmholtz equation is defined in the wavenumber domain as follows

$$k^2 \frac{\partial}{\partial z} \left(k^{-2} \frac{\partial P}{\partial z} \right) + k_z^2 P = -S_\delta \delta(z - z_s) \quad (2.1)$$

Where, z corresponds to height and z_s is the height of the source. Depending if the acoustic pressure is expressed in a rectangular or axisymmetric wavenumber domain, as $P(k_x, k_y, z)$ or as $P(k_r, z)$, the expressions for k , k_z and S_δ in equation (2.1) are different as specified in Table 2.1. In this table, k_x and k_y correspond to the acoustic wavenumber components expressed in terms of x and y rectangular coordinates. On the other hand, k_r is the wavenumber component along a radial direction from the source and always parallel to a flat ground surface (Terrain irregularities cannot be taken into account when FFP is used). In both cases, z corresponds to height.

Table 2.1: Expressions for k , k_z and S_δ for rectangular and axisymmetric pressure domain (see equation (2.1)).

	Pressure Domain	
Helmholtz Equation Terms	$P(k_x, k_y, z)$	$P(k_r, z)$
k	$\frac{\omega}{c} - \frac{k_x u}{c} + \frac{k_y v}{c}$	$\frac{\omega}{c + v_r}$
k_z	$\sqrt{k^2 - k_x^2 - k_y^2}$	$\sqrt{k^2 - k_r^2}$
S_δ	4π	$\sqrt{2\pi k_r}$

As observed, both cases address wind velocity components in a different manner. In Table 2.1 u and v correspond to the wind velocities in both the x and y directions, while v_r is the wind velocity in the radial direction. In addition, for all the formulation shown in Table 2.1, c corresponds to a constant speed of sound considered at the source's location.

For FFP applications, the wavenumber k is constant within each layer, thus equation (2.1) becomes

$$\frac{\partial^2 P}{\partial z^2} + k_z^2 P = -S_\delta \delta(z - z_s) \quad (2.2)$$

The solution for equation (2.2) has the form

$$P_j = A_j e^{(ik_{zj}z)} + B_j e^{(-ik_{zj}z)} \quad (2.3)$$

Where, $z_j \leq z \leq z_{j+1}$ corresponds to the boundaries of all j layers considered in the domain, as shown in Figure 2.2., k_{zj} corresponds to the value of k_z for each layer, while A_j and B_j are constants obtained from boundary conditions

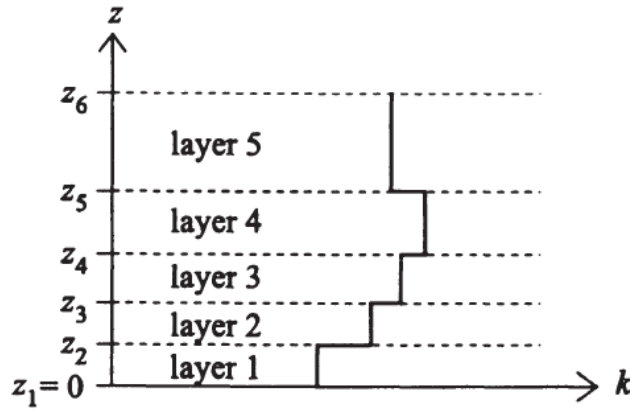


Figure 2.2: FFP Discrete atmospheric layers (E. M. Salomons, 2001).

From equation (2.3) the next relations can be obtained

$$\begin{aligned} P_j(z + \Delta z) &= \cos(k_{zj}\Delta z) P_j(z) + k_{zj}^{-1} \sin(k_{zj}\Delta z) P_j'(z) \\ P_j'(z + \Delta z) &= -k_{zj} \sin(k_{zj}\Delta z) P_j(z) + \cos(k_{zj}\Delta z) P_j'(z) \end{aligned} \quad (2.4)$$

On the other hand, the following boundary conditions have to be applied in order to obtain the constants A_j and B_j

$$\begin{aligned}
P_j(z_j) &= P_{j-1}(z_j) && \text{for } j = 1, 2, \dots, N && (2.5) \\
\eta_j^{-1} \rho_j^{-1} \frac{\partial P_j(z_j)}{\partial z} &= \eta_{j-1}^{-1} \rho_{j-1}^{-1} \frac{\partial P_{j-1}(z_j)}{\partial z} && \text{for } j = 2, 3, \dots, N (j \neq m) \\
\frac{\partial P_j(z_j)}{\partial z} &= \frac{\partial P_{j-1}(z_j)}{\partial z} - S_\delta && \text{for } j = m \\
\rho_j^{-1} \frac{\partial P_j(z_j)}{\partial z} &= \rho_{j-1}^{-1} \frac{\partial P_{j-1}(z_j)}{\partial z} && \text{for } j = 1
\end{aligned}$$

In this case, m represents the layer where the source is located, N represents the layer at the top of the media, and η_j represents the value of $-i\omega + ik_x u + ik_y v$ or $-i\omega + ik_r v_r$ at the layer j . Thus, by implementing boundary conditions over the ground at $z_1 = 0$, then

$$A_1 = R(k_{z_1}) B_1 \quad (2.6)$$

Where,

$$R(k_{z_1}) = \frac{k_{z_1} - k(z_1)/z_s}{k_{z_1} + k(z_1)/z_s} \quad (2.7)$$

The next step is to extrapolate the noise field from the ground to the source. The pressure values for the case where $j = 1$ are obtained by arbitrarily setting $B_1 = 1$ as follows

$$\begin{aligned}
P_1(z_1) &= R(k_{z_1}) + 1 && (2.8) \\
P_1'(z_1) &= ik_{z_1} [R(k_{z_1}) - 1]
\end{aligned}$$

Then, $P_{j-1}(z_j)$ and $P'_{j-1}(z_j)$ are determined successively for $j=1, 2, 3 \dots m$. To do so, equations in (2.4) and (2.5) have to be used, where $\Delta z = z_{j+1} - z_j$ and $z = z_j$. The final values correspond to $P_{m-1}(z_m)$ and $P'_{m-1}(z_m)$.

On the other hand, the next step is to extrapolate the noise field from the top of the media to the source. In this case, it is assumed that $P_{N-1}(z_N)$ is equal to one. From the boundary conditions, equations it is determined that

$$\begin{aligned} P_{N-1}(z_N) &= 1 \\ P'_{N-1}(z_N) &= ik_{z_N} \end{aligned} \quad (2.9)$$

The values of $P_j(z_j)$ and $P'_j(z_j)$ are determined successively for $j=N-1, N-2, N-3, \dots, m$, using equations in (2.4) and (2.5) with $z = z_{j+1}$ and $\Delta z = z_j - z_{j+1}$. The final values correspond $P_m(z_m)$ and $P'_m(z_m)$.

Because of the assumptions made on the previous steps with $B_1 = 1$ and $P_{N-1}(z_N) = 1$, the pressure predictions are no accurate. In order to obtain the correct values, the next relation is used

$$\left(\frac{P'_m(z_m)}{P_m(z_m)} \right) P_m - \left(\frac{P'_{m-1}(z_m)}{P_{m-1}(z_m)} \right) P_m = -S_\delta \quad (2.10)$$

where P_m is the correct value of pressure at the source height. The correct values of P_j and P'_j are the obtained by multiplying the values obtained from the previous step

$$\begin{aligned} \left(\frac{P_m}{P_m(z_m)} \right) & \quad \text{for } z_j > z_m \\ \left(\frac{P_m}{P_{m-1}(z_m)} \right) & \quad \text{for } z_j < z_m \end{aligned} \quad (2.11)$$

Finally, an inverse wavenumber transform is used to compute $P_j(k_x, k_y, z)$ in the three dimensional spatial domain as follows

$$p_{c,j}(x, y, z) = \frac{1}{4\pi^2} \int_{-\infty}^{\infty} \int_{-\infty}^{\infty} \exp(ik_x x + ik_y y) P_j(k_x, k_y, z) dk_x dk_y \quad (2.12)$$

$P_j(k_r, z)$ can also be computed in the spatial domain as

$$p_{c,j}(r, z) = \frac{1}{\pi\sqrt{2}} \int_{-\infty}^{\infty} [\exp(ik_r r) + \exp(-ik_r r)] P_j(k_r, z) dk_r \quad (2.13)$$

Crank Nicholson Parabolic Equation Method (CNPE)

This method is not limited to a layered atmosphere and homogeneous ground surface, i.e. arbitrary speed of sound profile and ground impedance may be implemented. Furthermore, irregular terrain and turbulence can be taken into account (E. M. Salomons, 2001). However, this method is restricted for propagation under elevation angles γ of a maximum of 35 degrees (see Figure 2.3).

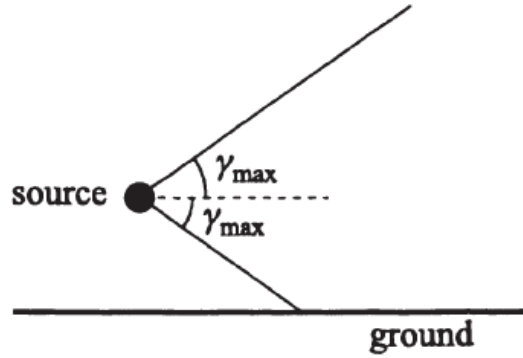


Figure 2.3: Elevation angles for PE methods (E. M. Salomons, 2001).

This method is solved using an axisymmetric coordinate system (see Figure 2.1) in the spatial domain. Thus, the following Helmholtz equation is used

$$\frac{\partial p_c}{\partial r^2} + \frac{\partial^2 p_c}{\partial z^2} + k_{eff}^2 p_c = 0 \quad (2.14)$$

where, the pressure amplitude is expressed as $p_c(r, z)$ and the effective wavenumber is given as $k_{eff} = \omega/c + v_r$. The acoustic field $p_c(r, z)$ is computed over a grid in the (r, z) domain as shown in Figure 2.4. The grid spacing for both Δr and Δz are limited to $\lambda/10$, where λ is the average wavelength of the propagated waves.

The assumed solution to the Helmholtz equation (2.14) is the following

$$p_c(r, z) = \psi(r, z) \exp(ik_a r) \quad (2.15)$$

Where, k_a is the value of the wavenumber at ground surface. If (2.15) is replaced into (2.14), then the following parabolic PDE is obtained

$$2ik_a \frac{\partial \psi}{\partial r} + \frac{\partial^2 \psi}{\partial z^2} + (k^2 - k_a^2) \psi = 0 \quad (2.16)$$

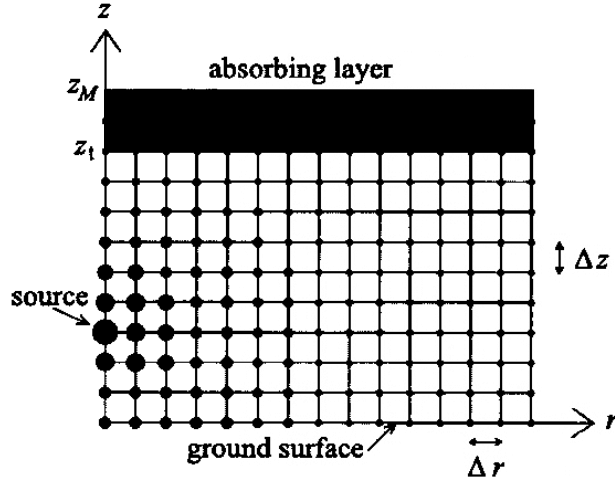


Figure 2.4: CNPE pressure domain grid (E. M. Salomons, 2001).

Equation (2.16) assumes that $\psi(r, z)$ varies very slowly with r . In addition, it applies exclusively for up to elevation angles of 10 degrees, thus it is called the narrow angle parabolic equation.

A wide-angle parabolic equation can also be obtained. Equation (2.14) can be expressed as

$$[\partial_r - iH_1(z)][\partial_r + iH_1(z)]p_c = 0 \quad (2.17)$$

Where, $\partial_r = \partial/\partial r$ and $H_1(z)$ is an expansion of the square root operator given by

$$H_1(z) = k_a \frac{1 + \frac{3}{4}s}{1 + \frac{1}{4}s} \quad (2.18)$$

The factor $[\partial_r - iH_1(z)]$ represents waves traveling in the positive r direction and $[\partial_r + iH_1(z)]$

in the negative r direction. Therefore, the second one can be ignored for atmospheric propagation. By replacing equation (2.18) in (2.17), the positive traveling wave or wide-angle parabolic equation becomes

$$\left(1 + \frac{1}{4}s\right) \partial_r \psi = \frac{1}{2} i k_a s \psi \quad (2.19)$$

Where, equation (2.15) is also used and s is

$$s = k_a^{-1} \delta k^2(z) + k_a^{-2} \partial_z^2 \quad (2.20)$$

In addition to the derivation of the Crank Nicholson narrow and wide-angle parabolic equations, a finite difference solution for both is presented. For the narrow-angle, the solution procedure is the following. First, equation (2.16) is re-written as

$$\partial_r = \alpha \partial_z^2 \psi + \beta \psi \quad (2.21)$$

Where, $\alpha = 0.5i/k_a$ and $\beta = 0.5i(k^2 - k_a^2)/k_a$. Equation (2.21) needs to be adapted to matrix form so that it accounts all the points in the grid shown in Figure 2.4. The field ψ for the range r is defined as a vector $\vec{\psi}(r)$ with elements $\psi_j = \psi(r, z_j)$ for each the heights $j=1, 2, 3 \dots M$ defined by the grid. For the derivative $(\partial_z^2 \psi)_{z_j}$ the central difference formula is used as follows

$$\left(\partial_z^2 \psi\right)_{z_j} = \frac{\psi_{j+1} - 2\psi_j + \psi_{j-1}}{(\Delta z)^2} \quad (2.22)$$

The resultant equation in matrix form for the grid is thus

$$\partial_r \vec{\psi} = (\gamma T + D) \vec{\psi} \quad (2.23)$$

Where, γ is a parameter given by $\gamma = \alpha/(\Delta z)^2$ and the matrices T and D are

$$T = \begin{pmatrix} -2+\sigma_1 & 1+\sigma_2 & & & & & \\ 1 & -2 & 1 & & & & \\ & 1 & -2 & 1 & & & \\ & & \ddots & \ddots & \ddots & & \\ & & & 1 & -2 & 1 & \\ & & & & 1+\tau_2 & -2+\tau_1 & \end{pmatrix} \quad (2.24)$$

$$D = \begin{pmatrix} \beta_1 & & & & & & \\ & \beta_2 & & & & & \\ & & \beta_3 & & & & \\ & & & \ddots & & & \\ & & & & \beta_{M-1} & & \\ & & & & & \beta_M & \end{pmatrix} \quad (2.25)$$

The coefficients σ_1 and σ_2 depend on the ground impedance, and coefficients τ_1 and τ_2 take into account the boundary conditions at the top of the grid (a normalized impedance of 1 is taken). The integration of equation (2.23) is then performed as follows

$$\vec{\psi}(r + \Delta r) - \vec{\psi}(r) = (\gamma T + D) \int_r^{r+\Delta r} \vec{\psi} dr \quad (2.26)$$

Where the integral on the right hand side of equation (2.26) is computed using a Crank-Nicholson approximation

$$\int_{2r}^{r+\Delta r} \vec{\psi} dr = \frac{1}{2} [\vec{\psi}(r + \Delta r) + \vec{\psi}(r)] \Delta r \quad (2.27)$$

Finally, the solution is given by

$$M_2 \vec{\psi}(r + \Delta r) = M_1 \vec{\psi}(r) \quad (2.28)$$

Where, the tridiagonal matrices M_1 and M_2 are:

$$M_1 = 1 + \frac{1}{2} \Delta r (\gamma T + D) \quad (2.29)$$

$$M_2 = 1 - \frac{1}{2} \Delta r (\gamma T + D)$$

For the case of the wide-angle parabolic equation, the same procedure should be followed. The difference is in the tridiagonal matrices M_1 and M_2 . In this case these are

$$M_1 = 1 + \frac{1}{2} \Delta r (\gamma T + D) + \frac{\gamma T + D}{2ik_a} \quad (2.30)$$

$$M_2 = 1 - \frac{1}{2} \Delta r (\gamma T + D) + \frac{\gamma T + D}{2ik_a}$$

Finally, both the narrow and wide-angle CNPE method require a starting field in order to perform the propagation over the grid. For the narrow-angle case, the following field is used

$$p_c(0, z) = \sqrt{ik_a} e^{-\frac{1}{2}k_a^2 z^2} \quad (2.31)$$

On the other hand, for the wide-angle case the starting field is

$$p_c(0, z) = \sqrt{ik_a} (1.3717 - 0.3701k_a^2 z^2) e^{-\frac{1}{3}k_a^2 z^2} \quad (2.32)$$

Green's Function Parabolic Equation Method (GFPE)

The GFPE method is more efficient than CNPE method because larger extrapolation steps Δr can be used. The derivation of this method starts with the Helmholtz equation in (2.14), where the acoustic field given by $p_c(r, z)$ must be solved. In this section, only the 2D GFPE method will be analyzed.

By means of the Kirchhoff-Helmholtz integral for complex pressure fields shown in the work of E. M. Salomons (2001) and the Rayleigh integral (Rayleigh, 1945), the acoustic field generated by the noise source is modeled as

$$p_c(r + \Delta r, z) = \frac{1}{4\pi^2 i} \int_{-\infty}^{\infty} \exp(i\kappa \Delta r) k dk \int_0^{\infty} G(\kappa, z', z) p_c(r, z') dz' \quad (2.33)$$

Where, $G(k, z', z)$ corresponds to a green's function that must satisfy the following equation

$$\left[\frac{\partial^2}{\partial z^2} + k^2(z) - \kappa^2 \right] G(\kappa, z', z) = -4\pi \delta(z - z') \quad (2.34)$$

For equations (2.33) and (2.34), κ corresponds to the horizontal wavenumber amplitude in the radial direction, $k(z)$ is the total wavenumber amplitude, and z' is the height of the source location.

For non-refracting media (homogeneous media) the wavenumber is a constant, following equation (2.34), then the green's function $G(k, z', z)$ is given by

$$G(\kappa, z', z) = \frac{2\pi i}{k_z} \left\{ \exp(ik_z |z - z'|) + R(k_z) \exp(ik_z [z + z']) \right\} \quad (2.35)$$

Where, k_v is the vertical wavenumber amplitude given by

$$k_z^2 = k^2(z) - \kappa^2 \quad (2.36)$$

and

$$R(k_z) = \frac{k_z Z_G - k(z)}{k_z Z_G + k(z)} \quad (2.37)$$

This is the plane wave reflection coefficient where Z_G is the ground normalized impedance. It should also be noticed that $k(z)$ is a constant, since the media is a homogeneous one.

After replacing equation (2.35) into (2.33), the non-refracting field can be calculated as follows

$$\begin{aligned}
p_c(r + \Delta r, z) = & \frac{1}{2\pi} \int_{-\infty}^{\infty} \exp\left(i\Delta r \sqrt{k(z)^2 - k_z^2}\right) \exp(ik_z z) dk_z \int_0^{\infty} \exp(-ik_z z') p_c(r, z') dz' + \\
& \frac{1}{2\pi} \int_{-\infty}^{\infty} R(k_z) \exp\left(i\Delta r \sqrt{k(z)^2 - k_z^2}\right) \exp(ik_z z) dk_z \int_0^{\infty} \exp(ik_z z') p_c(r, z') dz' + \\
& 2i\beta \exp(-i\beta z) \exp\left(i\Delta r \sqrt{k(z)^2 - \beta^2}\right) \int_0^{\infty} \exp(-i\beta z') p_c(r, z') dz'
\end{aligned} \tag{2.38}$$

Where, $\beta = k(z)/Z_G$.

In order to take into account for refraction in an inhomogeneous atmosphere, equation (2.38) has to be multiplied by the following refraction factor

$$\exp\left(i\Delta r \frac{\delta k^2(z)}{2k_a}\right) \tag{2.39}$$

Where, k_a is the wavenumber at the source's location and $\delta k(z)^2 = k(z)^2 - k_a^2$. In addition, if $p_c(r, z)$ is replaced by $\psi(r, z) = \exp(-ik_a r) p_c(r, z)$, the refractive acoustic field becomes

$$\psi(r + \Delta r, z) = \exp\left(i\Delta r \frac{\delta k^2(z)}{2k_a}\right) \times \left\{ \begin{aligned} & \frac{1}{2\pi} \int_{-\infty}^{\infty} \exp[\Psi(r, k_z) + R(k_z) \Psi(r, -k_z)] \times \dots \\ & \exp\left(i\Delta r \left[\sqrt{k_a^2 - k_z^2} - k_a\right]\right) \exp(ik_z z) dk_z + \dots \\ & 2i\beta \Psi(r, \beta) \exp\left(i\Delta r \sqrt{k_a^2 - \beta^2} - k_a\right) \exp(-i\beta z) \end{aligned} \right\} \tag{2.40}$$

Where,

$$\Psi(r, k_z) = \int_0^{\infty} \exp(-ik_z z') \psi(r, z') dz' \tag{2.41}$$

The GFPE method also needs a starting field. In this case $q(0, z)$ is determined as

$$p_c(0, z) = \sqrt{ik_a} \left(A_0 + A_2 k_a^2 z^2 + A_4 k_a^4 z^4 + A_6 k_a^6 z^6 + A_8 k_a^8 z^8 \right) e^{-\frac{1}{B} k_a^2 z^2} \tag{2.42}$$

Where, the values for the constants A_0 through A_8 , and B are defined by E. M. Salomons (2001)

as shown in Table 2.2.

Table 2.2: Values for GFPE starting field parameters (E. M. Salomons, 2001).

Constant	Value
A_0	9.6982
A_2	-20.3785
A_4	6.0191
A_6	-0.4846
A_8	0.0105
B	3

In order to apply the GFPE method for a grid in space, a finite differences technique similar to the one presented for CNPE should be used. This means that the grid spacing for this method is limited. For Δz it should not exceed $\lambda/10$, however, for Δr can be chosen up to 10λ .

Finally, a three dimensional GNPE approach can also be implemented if the angle ϕ is also taken into account in the axisymmetric coordinates as shown in Figure 2.5. The method is similar to the one described in this section.

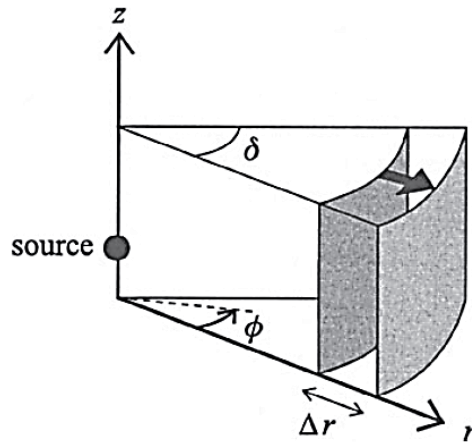


Figure 2.5: 3D GFPE method coordinates (E. Salomons et al., 2011).

Eikonal Ray Tracing (ERT)

The Eikonal ray tracing method is based on an asymptotic series expansion for the Helmholtz wave equation. The assumed solution is based on high frequency approximations from which the

Eikonal and the Transport equations are derived (Jensen, 2011). These equations describe the path taken by the ray and the pressure levels associated to them, respectively. This ray tracing approach is presented in this section.

An acoustic wave is characterized by pressure fluctuations, and it is determined by the following wave equation

$$\nabla^2 p - \frac{1}{c^2(\vec{r})} \frac{\partial^2 p}{\partial t^2} = 0 \quad (2.43)$$

Where, the speed of sound c is a function of the location in space specified by $\vec{r} = x\hat{i} + y\hat{j} + z\hat{k}$, and dependent of the local temperature. The assumed solution for equation (2.43) is the following

$$p(\vec{r}, t) = P(\vec{r})e^{i\omega t} \quad (2.44)$$

If equation (2.44) is replaced into equation (2.43) then the following Helmholtz equation is obtained

$$\nabla^2 P(\vec{r}) + \frac{\omega^2}{c^2(\vec{r})} P(\vec{r}) = 0 \quad (2.45)$$

Physically, both the wave and Helmholtz equations represent a wave travelling in space. Figure 2.6 shows the path followed by an acoustic wave in the (x, z) plane generated by a point source in isotropic media. In this case, the waves are assumed to be rays that travel through straight lines, in a direction orthogonal to the wave fronts τ . The dashed lines in Figure 2.6 correspond to the local wave fronts, and each of them is a surface of constant phase (Jensen, 2011).

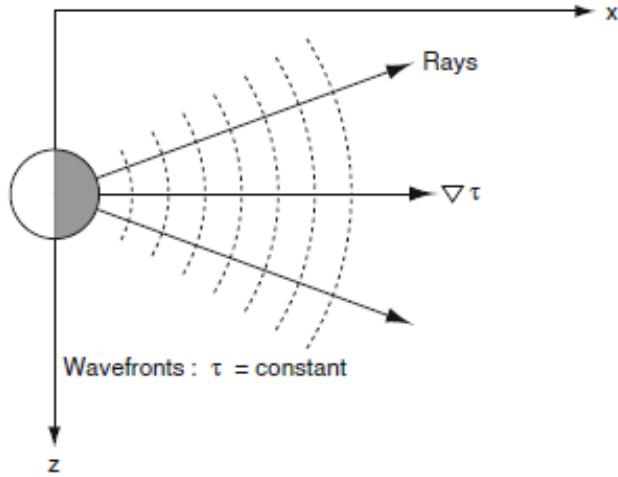


Figure 2.6: Ray Propagation in Homogeneous Media (Jensen, 2011).

For a refractive media such as the atmosphere, the path taken by rays is not characterized by straight lines as it is for isotropic media. The surfaces of constant phase change in shape in space according to the local wavenumber, which is ultimately dependent on wind velocity and temperature. This phenomenon is observed in Figure 2.7.

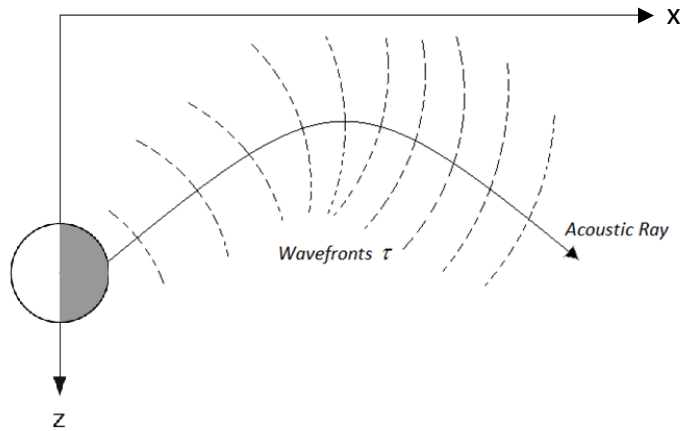


Figure 2.7: Ray Propagation in Inhomogeneous Media.

The solution to the Helmholtz equation in (2.45) can be assumed to be in the form of an asymptotic series as follows

$$P(\vec{r}) = e^{i\omega\tau(\vec{r})} \sum_{n=0}^{\infty} \frac{A_n(\vec{r})}{(i\omega)^n} \quad (2.46)$$

where τ is the wave-front, and $A_n(\vec{r})$ corresponds to an amplitude which can be either imaginary or real depending on the boundary conditions of the system. This type of series is divergent in the case of small frequencies. The error of the expansion is small if ω is sufficiently large, making this type of solution a high frequency approximation (Brokesova, 2006). Thus, only the first terms of (2.46) should be taken into account. In this case, a zero order of the asymptotic series is used. Taking the appropriate partial derivatives of the assumed asymptotic solution (2.46) in order to determine $\nabla^2 P(\vec{r})$, and replacing the results in (2.45) gives

$$-\omega^2 |\nabla \tau|^2 A_0 + i\omega \nabla^2 \tau A_0 + 2i\omega \nabla \tau \nabla A_0 + \nabla^2 A_0 = -\omega^2 \frac{1}{c(\vec{r})} A_0 \quad (2.47)$$

If the terms containing the same order of frequency ω^2 (second order) on both sides of equation (2.47) are equated, then the Eikonal equation in magnitude form is obtained

$$|\nabla \tau|^2 = \left(\frac{1}{c(\vec{r})} \right)^2 \quad (2.48)$$

Where, $\nabla \tau$ is a vector perpendicular to the wave front of the wave and $c(\vec{r})$ is the speed of sound. From the Eikonal equation in (2.48), a unit vector is defined as follows

$$\frac{d\vec{r}}{ds} = c \nabla \tau \quad (2.49)$$

$d\vec{r}/ds$ is a unit vector in the direction of $\nabla \tau$ as shown in Figure 2.8.

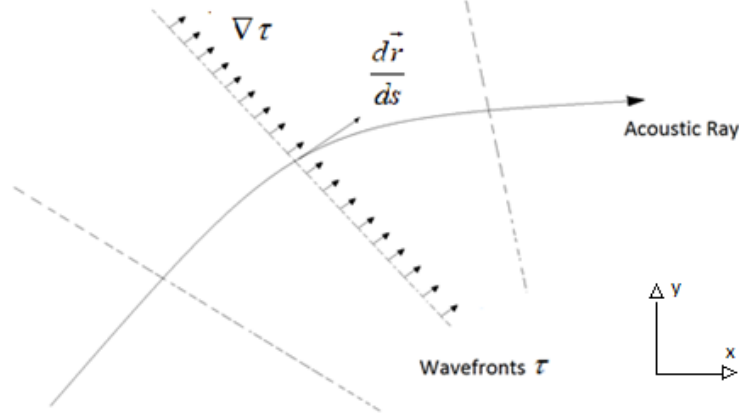


Figure 2.8: Unit vector $d\vec{r}/ds$ and $\nabla\tau$ during ray propagation.

The Eikonal equation in (2.49) only takes into account spatial changes in the speed of sound due to temperature variations. However, the presence of ambient fluid velocity also affects the ray propagation velocity. It does so by adding it to the ambient velocity component in the direction normal to the wave fronts (Brouwer, 2014). To show this, it is convenient to define a vector $\vec{V}(\vec{r}) = (v_x, v_y, v_z)$ corresponding to the spatial ambient flow velocity as a function of spatial location. Thus, the effective speed of sound, which is to be called c_{eff} is defined as

$$c_{eff} = c(\vec{r}) + \vec{V} \cdot \frac{d\vec{r}}{ds} \quad (2.50)$$

As observed in Figure 2.8, it should be noted that $d\vec{r}/ds$ corresponds to a unit vector normal to the wave fronts and equals $\nabla\tau/|\nabla\tau|$. In order to include the effective speed of sound in (2.49), c is replaced by c_{eff} . Thus modifying the Eikonal Equation in magnitude form to

$$|\nabla\tau|^2 = \left(\frac{1 - \vec{V} \cdot \nabla\tau}{c(\vec{r})} \right)^2 \quad (2.51)$$

The procedure used to solve the Eikonal equation in (2.51) is presented in Appendix C.

On the other hand, the transport equation is used to determine the sound pressure levels associated to the rays during propagation. In order to obtain this equation, from (2.47) the terms of first order frequency ω are equated on both sides of the equation. This results in the following,

$$i\omega 2\nabla\tau \cdot \nabla A_0 + i\omega (\nabla^2\tau) A_0 = 0 \quad (2.52)$$

After dividing (2.52) by $i\omega$ then

$$2\nabla\tau \cdot \nabla A_0 + (\nabla^2\tau) A_0 = 0 \quad (2.53)$$

Equation (2.53) is used to determine the amplitude associated with each ray (Brouwer, 2014). Alternatively, the common and simpler ray tube approach for ray tracing (explained in Chapter 3) can be used to compute the sound pressure levels associated to the rays.

2.2. ANALYTICAL METHODS

Atmospheric sound propagation can be analytically modeled through geometric ray approaches. However, these type of methods are limited to unrealistic media i.e. linear speed of sound atmospheric profiles. Furthermore, they do not consider temperature and wind as two separate refracting phenomena. The work by Hidaka et al. (1985) and L'Espérance et al. (1992) have included this approach in their models. In addition, Qi Mo et al. (2015) have also introduced analytic ray path solutions into their models. The most relevant analytical methods will be covered in this section.

Geometric Ray Theory

The geometric ray approach is based on the geometric problem presented on Figure 2.9. Rays originating at the noise source are divided into those that directly arrive to the receiver and those that reflect over the ground. Initially, a homogeneous non-moving media is assumed i.e. spatially homogeneous temperature and no wind. Thus, acoustic rays propagate following a straight line.

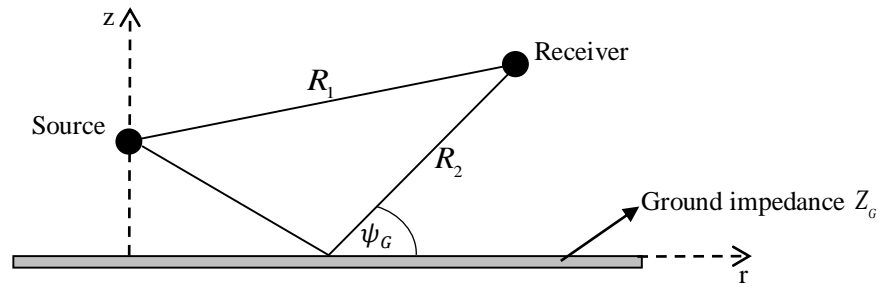


Figure 2.9: Sound Propagation Scheme over ground with impedance Z_G .

A 2D Helmholtz equation characterizes the spherical waves propagating outwards from the source. It is expressed in cylindrical coordinates (only as a function of horizontal distance from the source r and its height z). That is

$$\nabla^2 P(r, z) + k^2 P(r, z) = -2\delta(r)\delta(z - z_0) \quad (2.54)$$

In order to solve this equation, it is necessary to define the ground boundary condition. Nobile et al. (1985) used the following boundary condition

$$\frac{\partial P(r, z)}{\partial z} + i \frac{k\rho c}{Z_G} P(r, 0) = 0 \quad (2.55)$$

where Z_G corresponds to the ground impedance and k is the media's wavenumber. The ground impedance Z_G is determined by conventional models found in literature. These will be covered in the Chapter 3. By implementing the method of images, a solution is defined as a simple sum of the direct component and reflected component of noise. The solution is of the form

$$P(r, z) = \frac{A_1 e^{ikR_1}}{R_1} + Q \frac{A_2 e^{ikR_2}}{R_2} \quad (2.56)$$

In this case, A_1 and A_2 are the amplitudes for the direct and reflected rays. In addition, R_1 and R_2 correspond to the geometrical path lengths of the direct and reflected rays respectively while Q is the image source strength and is defined as follows

$$Q = R_p + (1 - R_p)F \quad (2.57)$$

where, R_p corresponds to the plane wave reflection coefficient and F is known as the boundary loss factor. This type of solution is addressed by many authors. However, depending on the media and reflecting surface characteristics, there are a few differences among them. According to Chessell (1977), the formulation for R_p is the following

$$R_p = \frac{\sin \psi_G - \frac{Z_M}{Z_G} \left(1 - \frac{k_M^2}{k_G^2} \cos^2 \psi_R \right)^{1/2}}{\sin \psi_G + \frac{Z_M}{Z_G} \left(1 - \frac{k_M^2}{k_G^2} \cos^2 \psi_R \right)^{1/2}} \quad (2.58)$$

The angle ψ_G is defined between the ground surface and the incident ray, while the angle ψ_R between the ground surface and a refracted ray propagating through the ground. On the other hand, Z_M and k_M correspond to the media's impedance and wavenumber. The ground's impedance and wavenumber are Z_G and k_G , respectively. This approach is used by Bérengier et al. (1997) to characterize atmospheric noise propagation over porous ground media such as road pavements. However, common atmospheric noise propagation methods consider that wave propagation through the ground is negligible. Thus, equation (2.57) becomes

$$R_p = \frac{\sin \psi_G - \frac{\rho c}{Z_G}}{\sin \psi_G + \frac{\rho c}{Z_G}} \quad (2.59)$$

where, the media's impedance Z_M was replaced by ρc .

On the other hand, in equation (2.57) F is a function that depends on w , the so-called *numerical distance* or *boundary loss factor*. Literature provides several approaches for characterizing it. Nobile et al. (1985) approximated the source's field solution in the form of asymptotic series and arrived to

$$F(w) = 1 + i\sqrt{\pi}w \exp(-w^2) \operatorname{erfc}(-iw) \quad (2.60)$$

The developments by Chien et al. (1975) also included an expression for the case where the numerical distance is large. Thus, becoming

$$F(w) = 2i\sqrt{\pi}w \exp(-w^2) H(-\operatorname{Im}(w)) \quad (2.61)$$

Given that the expressions in (2.60) and (2.61) are derived from asymptotic expansions, more terms can be included. L'Espérance et al. (1992) have included more expansion terms in their propagation models, as well as Bérengier et al. (2003).

Finally, the numerical distance is given by

$$w^2 = \frac{1}{2} jkR_2 [\sin \psi_G + (1/Z_G)]^2 \quad (2.62)$$

Extended ground porous media can also be considered in the numerical distance. For example,

Bérenghier et al. (1997) introduced an expression that includes the complex wavenumber of porous ground.

In order to take into account refraction, geometrical wave methods are limited to linear speed of sound profiles over the atmosphere. Thus, providing an unrealistic modeling scenario. The assumed linear speed of sound profile is the following

$$c(z) = c_0(1 + az) \quad (2.63)$$

Where, c_0 is a reference speed of sound gradient at the ground level, a is the selected speed of sound gradient and z is height. In this case, a solution to the Helmholtz equation in (2.54) is a variant of equation (2.56). Given that the wavenumber is not constant for the rays, the model uses different travel times for both the direct and reflected rays. This solution is given with the following expression

$$p^2 = \frac{A_1^2}{R_1^2} + \frac{A_2^2 |Q|^2}{R_2^2} + \frac{2A_1^2 A_2^2 |Q|}{R_1 R_2} \cos \left[2\pi f (\tau_2 - \tau_1) + \text{Arg}(Q) \right] \quad (2.64)$$

Where, τ_2 and τ_1 are defined as the effective travel times of R_2 and R_1 (Hidaka et al., 1985). These two parameters are defined by L'Espérance et al. (1992) and Bérenghier et al. (2003). This equation should also take into account atmospheric attenuation within its amplitudes. Conventional atmospheric attenuation methods are covered in Chapter 3.

The acoustic pressure field at the receiver location in inhomogeneous linear media is calculated using equation (2.64). However, only a single ground reflection is taken into account. If the gradient a is positive, multiple reflections may occur before the rays reach the receiver. Embleton et al. (1976) provided the following equation in order to estimate the number of reflections before a ray reaches the receiver

$$n(n+1)x^4 - (2n+1)Dx^3 + [b_2^2 + (2n^2 - 1)b_1^2 + D^2]x^2 - (2n-1)b_1^2Dx + n(n-1)b_1^4 = 0 \quad (2.65)$$

Where, D is the total horizontal distance between the source and receiver, n is the number of ground reflections, and

$$b_1^2 = h_s^2 + 2h_s / \gamma \quad (2.66)$$

$$b_2^2 = h_r^2 + 2h_r / \gamma \quad (2.67)$$

The multiple ray reflection geometry shown in Figure 2.10 shows that $1/\gamma$ corresponds to the distance between the ground and the ray's centers of curvature.

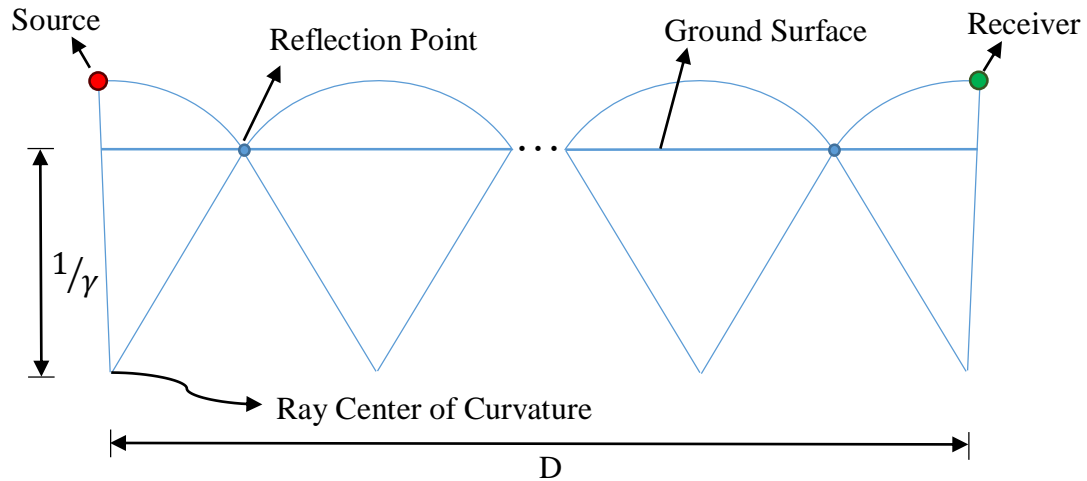


Figure 2.10: Multiple ray reflection geometry.

In order to determine the number of reflections, equation (2.65) must be implemented using $n = 0, 1, 2, 3 \dots$ until x is no longer a real value, as long as $0 < x < D$. After reflections have been taken into account, then equation (2.64) can be rewritten as

$$p^2 = \sum_{i=1}^N \frac{A_i^2 \times |Q_i|^2}{R_i^2} + 2 \sum_{i=2}^N \sum_{j=1}^{i-1} \frac{A_i |Q_i| \times A_j |Q_j|}{R_i R_j} \cos \left[2\pi f (\tau_j - \tau_i) + \text{Arg} \left(\frac{Q_j}{Q_i} \right) \right] \quad (2.68)$$

Where, N corresponds to the total number of rays reaching the receiver (both reflected and direct path rays). In addition, in equation (2.68) $i = 1$ denotes the direct ray. In this case, $Q_i = 1$ (Bérenghier et al., 2003).

It has to be taken into account that the solution presented in equation (2.68) is not valid in the case of a negative gradient a . In this case, rays behave differently because they refract upwards, as shown in Figure 2.11.

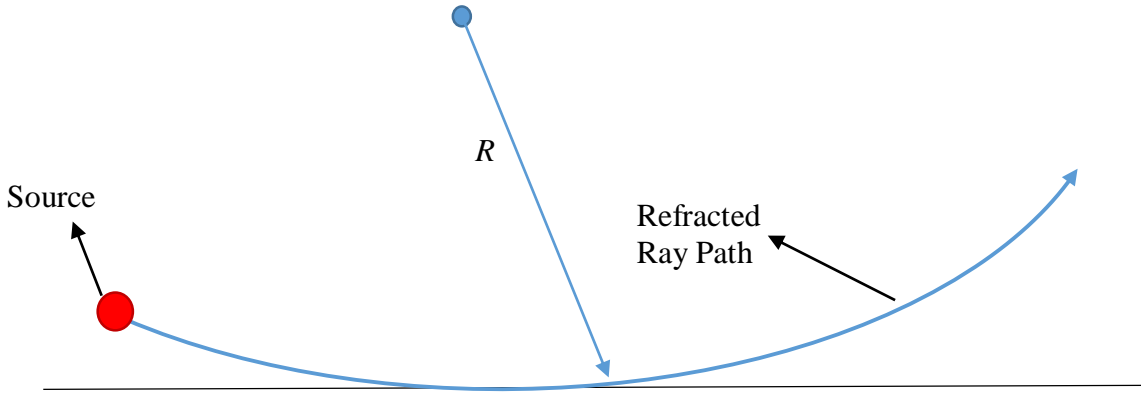


Figure 2.11: Upward refracted ray and shadow region formation.

Because rays refract upwards, there is a region where no rays reach. This is called the shadow region and noise cannot be predicted over this area with equation (2.68). Berry et al. (1988) provide the following solution to compute noise levels at the shadow region

$$p(r, z) = \frac{\pi e^{i\pi/6}}{l} S \sum_n H_0^{(1)}(k_n, r) \times \frac{Ai \left[b_n - (z_s/l) e^{2i\pi/3} \right] Ai \left[b_n - (z_r/l) e^{2i\pi/3} \right]}{\left[Ai(b_n) \right]^2 - b_n \left[Ai(b_n) \right]^2} \quad (2.69)$$

Where, S corresponds to the amplitude associated to the upward refracting rays that are closer to

ground level, z_s and z_r are the source and receiver heights above the ground, $H_0^{(1)}$ is a Hankel function of the first kind and order zero, and b_n corresponds to the zeros of

$$A_i'(b_n) + qe^{i\pi/3} A_i(b_n) = 0 \quad (2.70)$$

In this case, A_i represents an Airy function and A_i' its derivative. On the other hand,

$$q = jk_0 \rho l c / Z_G \quad (2.71)$$

Where, $l = (R/2k_0^2)^{1/3}$ given that R is the curvature radius, $k_0 = \omega/c_0$, ρ corresponds to density and Z_G is the ground's impedances. Evaluating for the valued of b_n becomes trivial in the case where $Z_G \rightarrow 0$ i.e. a rigid surface. If Z_G is a finite complex impedance, then equation (2.70) must be numerically solved.

Equation (2.69) must be implemented exclusively for receivers located within the shadow region. McAninch et al. (2006) defined elliptic boundaries defining where the shadow region starts referred to as Ellipses of Turning Points (ETP). This method classified all emitted rays into those that interact with the ground and those that do not.

Alternatively to equation (2.69), Qi Mo et al. (2017) proposed implementing a Gaussian beam approach to account for sound pressure levels over shadow regions. In this case, the ray's associated amplitude is initially computed using the transport equation and then a Gaussian beam is used to compute paraxial amplitudes (Červený, 2001). Gaussian beams can also be directly applied as an alternative to energy methods and the transport equation to compute ray amplitudes while tracing the rays (method usually referred as *Beam Tracing*). By using this technique, singularities such as caustics can be avoided (Porter et al., 1987).

Analytical Ray Path

Ray paths during propagation can be analytically solved with the Eikonal approach with limitations. Q. Mo et al. (2016) provide the following analytical solution for equation (2.51).

$$x(z) = \frac{\sqrt{1 - \xi_0'^2} c_0^2 - \sqrt{1 - \xi_0'^2} (c_0 + \alpha z)^2}{\xi_0' \alpha} \quad (2.72)$$

where, x corresponds to the horizontal component of the ray path and z to the ray's altitude, $\xi_0' = \cos \theta_0 / c_0$, θ_0 is the angle between the initial wavenumber vector \vec{k}_0 and a line parallel to the x -axis, c_0 is the speed of sound at the noise source's height, and α is the gradient of the speed linear profile. Thus, the speed of sound must be a 2D profile that follows the linear expression

$$c(z) = c_0 + \alpha z \quad (2.73)$$

Graphically, equation (2.72) traces circular ray paths in two dimensions and is limited to linear speed of sound profiles. However, for smooth inhomogeneous media, linear assumptions can be locally assumed. Then, as propagation progresses, new linear speed of sound gradients can be adapted (Qi Mo et al., 2015). Therefore, numerical procedures are still required to account for realistic media.

2.3. COMMERCIAL SOFTWARE PROPAGATION APPROACHES

In this section, a description of the most popular sound propagation approaches used by commercial software packages is provided. These are often referred to as *Engineering Methods* due to their straight-forward approaches and lack of physical complexity (Bowdler et al., 2012). Most of them include a large number of assumptions and simplifications, thus making them inaccurate in complex environmental situations such as wind turbine noise propagation (Peng, 2014). The standard ISO-9613-2 and methods used by commercial software such as Harmonoise, Nord 2000, ESDUpac and CONCAWE are covered in this section.

ISO 9613-2

ISO 9613-2 is an international standard for calculation of outdoor sound propagation. It consists

of two parts. Part 1 addresses atmospheric attenuation (see section 3.2), while Part 2 provides with guidelines to calculate propagated noise. The propagated sound is computed as follows

$$L_T(DW) = L_w + D_c - A \quad (2.74)$$

Where, L_w corresponds to the sound power level output of the source for a specified octave frequency band, D_c is the source's directivity correction, and A is the total attenuation levels at the receiver's location due to various propagation effects. Equation (2.74) is applicable only for a point source and only accurate for downwind receiver locations. The method is limited to cases where wind direction forms a maximum of 45 degrees with the direction connecting the noise source and the receiver (Bowdler et al., 2012).

The source directivity correction D_c is calculated by adding the directivity index of the point source D_I and an index D_Ω that accounts for spherical solid angles. If an omnidirectional point source is considered, then D_c is equal to zero (ISO, 1996). On the other hand, the total attenuation A is calculated by adding the effects of geometric divergence A_{div} , atmospheric absorption A_{atm} , and ground attenuation A_{gr} as follows

$$A = A_{div} + A_{atm} + A_{gr} \quad (2.75)$$

The geometrical divergence attenuation is defined by the acoustic spherical spreading during propagation. It is a frequency independent expression given by

$$A_{div} = 20 \log_{10} (d/d_0) + 11 \quad (2.76)$$

In this case d is the distance from the source to the receiver, and d_0 is a reference distances, usually of 1 meter (Bowdler et al., 2012). The atmospheric attenuation is given by

$$A_{atm} = \frac{\alpha d}{1000} \quad (2.77)$$

Where, α is a frequency dependent atmospheric attenuation coefficient expressed in $[dB/Km]$. The values for this coefficient can be obtained using ISO 9613-1. Further theoretical explanations on this coefficient are defined in section 3.2.

Finally, ground attenuation A_{gr} is calculated in the downwind direction exclusively for flat ground surfaces. The standard divides three different regions for ground attenuation. First, the source region covers the distance from the source towards the receiver up to $30h_s$. The receiver region covers the distance from the receiver towards the source up to $30h_r$. For both cases, h_s and h_r are the source and receiver heights, respectively. The third region is the middle one. It covers the distance between the source and receiver if $d_p < (30h_s + 30h_r)$, where d_p is the distance from the source to the receiver. In order to calculate the total ground attenuation from these three zones, their individual attenuations must be added as follows

$$A_{gr} = A_s + A_r + A_m \quad (2.78)$$

The expressions for these zone-divided attenuations depend on a ground factor G defined in the standard. For hard ground such as pavement, water, ice or concrete $G = 0$, for porous ground such as grass, trees and any type of vegetation $G = 1$. For mixed grounds and variations the value of G can be selected between zero and one (ISO, 1996). Other less common attenuation parameters can also be included. These correspond to attenuation due to barriers, a tree foliage, and industrial and housing sites attenuation.

ISO 9613-2 provides an estimate of noise only for downwind observer locations. Thus, it is very limited for wind turbine applications accuracy due to the complexity of the flow around it. Furthermore, this method does not take into account the specifics of meteorological conditions. According to Bowdler et al. (2012), the reliability of predictions for this method can only be ensured if a careful parameter selection is followed. For example, the ground attenuation factor G should be carefully chosen and observers very close to the ground should be avoided due to oversensitivity. Predictions that used this method are usually accompanied with measurements for validation and parameter tuning.

CONCAWE

CONCAWE is one of the most straightforward engineering methods for propagation. This model was initially developed for computing noise over neighboring areas of open-air industrial plants such as oil refineries. The approach to calculate the sound pressure levels at the receiver's location is given by

$$L_p = L_w + D - \sum_i K_i \quad (2.79)$$

Where, L_p is the sound pressure level at the receiver location, L_w is the sound power level of the source, D is the directivity of the source towards the receiver location and K_i correspond to various attenuation factors including loss due to spherical spreading, atmospheric absorption, ground reflections, wind, barriers, height of source and receiver in relation to topography, and screening by industrial equipment (Marsh, 1982). This method has a similar approach to the ISO-9613-2 method and thus presents similar limitations. However, it is still used in order to obtain rough noise estimates from simplistic noise sources.

ESDUpac

ESDUpac A8936 is a commercial program developed by IHS ESDU (ESDU, 1989). It simulates sound propagation over a flat impedance plane. The theoretical approach is based on an analytical geometrical solution similar to the one presented in section 2.2 and developed by (Rasmussen, 1986). It is limited to a two dimensional linear speed of sound media and low source heights, where wind can be taken into account by using effective speeds of sound. Atmospheric absorption and turbulence are also taken into account. Shadow regions are not predicted. Finally, ground reflections are also included in the model.

In order to calculate the acoustic pressure generated by a source, the field is calculated with cylindrical symmetry as follows

$$p = -2 \int_0^{\infty} J_0(\kappa D) P((z, \kappa) \kappa d\kappa) \quad (2.80)$$

Where, J_0 corresponds to a Bessel function of the first kind of order zero, $P(z, \kappa)$ denotes the transform of p and κ is the constant of integration. If the speed of sound gradient is positive, then

$$P(z, \kappa) = -v(\tau + s) \times \left[w(\tau + t) - \frac{w'(\tau) + qw(\tau)}{v'(\tau) + qv(\tau)} v(\tau + t) \right] l \quad (2.81)$$

On the other hand, if the linear speed of sound gradient is negative, then

$$P(z, \kappa) = -w(\tau - s) \times \left[v(\tau + t) - \frac{v'(\tau) - qv(\tau)}{w'(\tau) - qw(\tau)} w(\tau - t) \right] l \quad (2.82)$$

For both equations (2.80) and (2.81), $l = [|\gamma|2k(0)^2]$, $s = z_i/l$, $t = z/l$, $q = ik(0)\rho c(0)l/Z$, $\tau = [\kappa^2 - k(0)^2]l^2$, $w(\beta) = 2\sqrt{\pi}e^{i\pi/6}Ai(\beta e^{i2\pi/3})$, and $v(\beta) = \sqrt{\pi}Ai(\beta)$. In this case, γ is a constant indicating the speed of sound gradient, k is the wavenumber as a function of height, z_i is the largest height between the source's or observer's height, c is the speed of sound as a function of height, ρ is the density of air, Z is the specific acoustic ground impedance (calculated using the specific flow resistance of the ground surface), and Ai denotes an Airy function. The numerical integration of equations (2.80) and (2.81) is performed by using a repeated Simpson's rule (ESDU, 1989).

The output of this code corresponds to the attenuation relative to the free-field sound pressure levels. These results are presented in 1/3rd octave frequency bands at the receiver's location. This code provides an analytical solution that can be used to validate numerical methods under the specific conditions.

Harmonoise

The Harmonoise engineering model was developed as part of European projects with the objective of predicting road and rail noise. Extensions to this project also include applications to aircraft and industrial noise (van Maercke et al., 2009). In this method, the sound pressure levels at the receiver location is given by

$$L = L_{source} + \Delta L_{prop} \quad (2.83)$$

Where, L_{source} correspond to the source's level and ΔL_{prop} to the propagation attenuation. The last one includes geometrical, air absorption and excess attenuation as follows

$$\Delta L_{prop} = \Delta L_{geo} + \Delta L_{air} + \Delta L_{excess} \quad (2.84)$$

The geometric attenuation is defined as $\Delta L_{geo} = -10 \log_{10}(4\pi r^2)$ for a point source. The air absorption attenuation is given by $\Delta L_{air} = -\alpha_{air} r$, where α_{air} is the atmospheric absorption coefficient is given by ISO 9613-1 and r is the distance between the source and the receiver. Finally, the excess attenuation ΔL_{excess} accounts for atmospheric refraction, turbulence scattering, ground reflection and diffraction caused by obstacles (E. Salomons et al., 2011).

Harmonoise has the capability of taking into account uneven terrain by using a 2D ground profile between the receiver and the source, such as the one shown in Figure 2.12. S_r and R_r represent the source and receiver, while P_0 through P_8 are points between straight segments that conform the terrain profile. Attenuation due to diffraction is calculated at top edges of the ground profile (e.g. P_2, P_5, P_6) using the formulation developed by (Deygout, 1966).

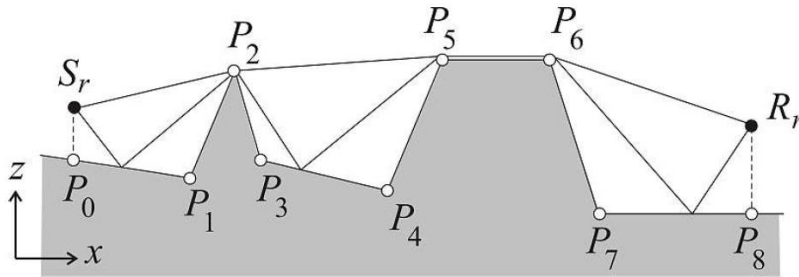


Figure 2.12: Uneven 2D terrain profile implemented in Harmonoise (E. Salomons et al., 2011).

Ground attenuation on the other hand is calculated depending on the type of ground. The three classifications used correspond to concave, convex and hull ground segments. The changes in sound pressure levels are calculated by using a spherical-wave reflection coefficients defined in the work by Chien et al. (1980). In addition, a geometrical weighting factor is used in order to account the differences between the free and diffracted acoustic fields. A coherence factor accounts

for changes in phase between the direct and reflected sound fields. Furthermore, instead of taking into account single specular point for reflections, a Fresnel zone over the reflection area is defined. The ground over the sides of the reflection point affect amplitude and phase of the reflected sound (This phenomenon is relevant only for acoustically inhomogeneous terrain). Mathematically, the changes in sound pressure levels are geometrically dependent on the Fresnel area and are taken into account by using Fresnel weights as described by C. H. Hansen et al. (2017). An example of the Fresnel area (ellipse) used for computations is shown in Figure 2.13.

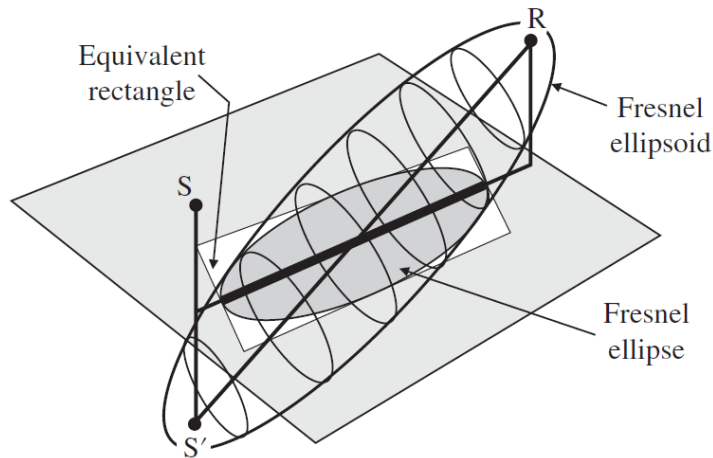


Figure 2.13: Illustration of the Fresnel ellipse area for a sound ray departing from the source S and arriving to the receiver R above the reflecting plane (C. H. Hansen et al., 2017).

The effects of refraction (bending acoustic rays) are taken into account by implementing conformal mapping. This is a coordinate transformation to the terrain segment points (P_0 through P_8 in Figure 2.12). In turn, the propagated rays also transform and bend. However, this approach is only capable of taking into account a linear speed of sound profile.

Nord 2000

Nord 2000 is an engineering propagation model developed by DELTA (Danish Electronics, Light and Acoustics) as part of a research project from Nordic European countries. This model implements an analytical ray tracing solution where the associated sound pressure levels L_R at the receiver location are calculated as follows

$$L_R = L_w + \Delta L_d + \Delta L_a + \Delta L_t + \Delta L_s \quad (2.85)$$

In this case, L_W is the source's sound power level per frequency band, ΔL_d accounts for the spherical divergence during propagation, ΔL_a accounts for air absorption, ΔL_t accounts for terrain effects including ground reflections and barriers, and ΔL_s accounts for scattering zones (Plovsig, 2006a).

The acoustic ray paths can be geometrically calculated exclusively for the following linear-type speed of sound profile

$$c(z) = c_0(1 + \xi(z - z_L)) \quad (2.86)$$

Where, c_0 is the speed of sound at the lowest point, $\xi = (\Delta c / \Delta z) / c_0$ is the relative profile's gradient. In order to account non-linear speed of sound profiles, Nord 2000 also has the capability of linearly approximating a logarithmic profile.

The propagating acoustic rays are defined by both their distance and travel time, given by

$$R(\Delta z) = \frac{1}{\xi \cos(\Psi_L)} \left(\arcsin((1 + \xi \Delta z) \cos(\Psi_L)) - \frac{\pi}{2} + \Psi_L \right) \quad (2.87)$$

$$\tau(\Delta z) = \frac{1}{2\xi c_0} \ln \left(\frac{\frac{1 + \sin(\Psi_L)}{1 - \sin(\Psi_L)}}{\frac{1 + \sqrt{1 - (1 + \xi \Delta z)^2 \cos^2 \Psi_L}}{1 + \sqrt{1 - (1 + \xi \Delta z)^2 \cos^2 \Psi_L}}} \right) \quad (2.88)$$

All the parameters for equation (2.83) and (2.84) are shown in Figure 2.14 for a ray propagating from the source L to the receiver U.

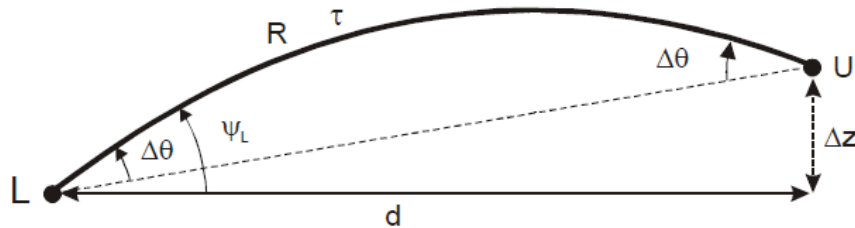


Figure 2.14: Definition of geometrical parameters for circular ray paths in Nord 2000 (Plovsig, 2006).

The spherical divergence of the sound energy associated to the propagated rays is given by

$$\Delta L_d = -10 \log(4\pi R^2) \quad (2.89)$$

The code includes formulation for shadow zone regions, multiple reflections and Fresnel zones. In addition, atmospheric absorption ΔL_α is computed according to ISO 9613-1. Various types of terrain can also be considered when calculating ΔL_t . These include flat and wedge-shaped terrain with single, double screens, or none. Furthermore, effects of scattering zones are computed. These zones reduce coherence in the sound field and usually correspond to housing areas and forests. Scattering effects (ΔL_s) are calculated through statistical methods (Plovsing, 2006).

Nord 2000 is one of the most advanced engineering propagation tools. However, the method still contains many simplifications and is not capable of implementing complex flow predictions in three dimensions. On the other hand, scattering computation capabilities, Fresnel zone considerations and several terrain-type considerations are some of its advantages over other prediction codes.

3. HAMILTONIAN RAY TRACING

The focus of this thesis is the development of a comprehensive atmospheric propagation model that accounts for all relevant physic phenomena present in the atmosphere. The second objective is to integrate it to a wind turbine noise prediction code. A Hamiltonian ray tracing technique based on the work by Lighthill (1978) has been developed and implemented. It avoids the limitations of common numerical approaches such as Fast Field Program (FFP), parabolic equation procedures (PE), and conventional Eikonal ray tracing. Table 3.1 briefly lists the key strengths and limitations of the numerical approaches compared to the developed Hamiltonian approach. Acoustic wave refraction due to spatial speed of sound gradients, a full Doppler Effect formulation due to wind velocities in any arbitrary direction, proper acoustic energy dissipation during propagation, and ground reflections are the fundamental issues that the developed code addresses.

Table 3.1: Numerical atmospheric propagation methods including the Hamiltonian ray technique.

	FFP	PE		RAY TRACING	
		CNPE	GFPE	Eikonal	Hamiltonian
Formulation	Horizontally layered Helmholtz in wavenumber domain	Cylindrical Helmholtz in parabolic form	Cylindrical Helmholtz / Green's function solution	Rectangular Helmholtz with asymptotic series solution	Wavenumber formulation approach
Limitations	<ul style="list-style-type: none"> • Flat and homogeneous terrain only • Low accuracy for 3D applications • No vertical wind component. • Effective wavenumber assumption 	<ul style="list-style-type: none"> • Maximum space grid resolution of $\lambda/10$ • Restrictions on large gradient speed of sound gradients (high elevation angles) • No vertical wind component • Effective wavenumber assumption 	<ul style="list-style-type: none"> • Reduced low frequency accuracy • Caustics Singularities 	<ul style="list-style-type: none"> • Caustics Singularities 	
Strengths	<ul style="list-style-type: none"> • Straightforward formulation • Good for rough estimates 	<ul style="list-style-type: none"> • Terrain irregularities can be incorporated 	<ul style="list-style-type: none"> • Terrain irregularities can be incorporated 	<ul style="list-style-type: none"> • Computationally efficient • Superior physical precision • Terrain irregularities can be incorporated 	

The general propagation problem is divided into two conjoin analyses. The first one focuses on determining the rays' propagation paths by taking into account the contributions of spatial wind and temperature distributions in the atmosphere. The rays propagate from a single noise source with any arbitrary directivity pattern and location in space. A set of 3 dimensional first order differential equations are solved in order to find i) the acoustic ray's location in 3D-space as they propagate, and ii) their corresponding local wavenumber vectors (including wave convective and bending components). Bent ray paths and wave fronts (areas of constant phase) are constructed from the output. The results allow the identification of highly dense acoustic energy zones and other low impact areas.

The second component of the total analysis corresponds to the characterization of the acoustic wave energy associated to the rays. In this case, tubes bounded by a bundle of rays are constructed. Energy conservation laws along the tubes are used to compute the intensity and sound pressure distributions in space. In the case where there is wind present in the media, the energy conservation equations are affected. All simulations include standard atmospheric wave attenuation and appropriate ground impedance models.

This chapter initially provides an insight on how the Hamiltonian equations determine ray path behavior based on the type of media. Section 3.2 explains the energy analysis incorporated in the model and how noise level predictions are constructed. Finally, section 3.3 provides validation for simple cases.

3.1. PATH OF A RAY

Ray tracing is a technique where it is inferred that acoustic waves propagating in space behave like particles moving along paths also known as rays. The relationship between energy and momentum of a particle can be regarded as the relation between frequency and wavenumber of the wave. In order to build the latter frequency-wavenumber wave relationship, wavenumber and frequency have to be defined.

This is done by analyzing the behavior of the wave's phase during propagation. The Hamiltonian formulation is based on this type of analysis. A frequency dispersion relationship is also required.

It defines the parameters of dependency of the acoustic wave's frequency, and is different for each media's homogeneity case. Finally, another parameter that influences the path of a ray is the spatial distribution of wind velocity in the propagation media. To account for it, the dispersion relationship for an acoustic ray is altered by a Doppler Effect formulation established between a stationary point of view and a relative one moving with the local wind velocity.

Acoustic Wave's Phase

The phase of a propagating acoustic wave is given by

$$\alpha = \omega t - \vec{k} \cdot \vec{r} = \omega t - (k_x x + k_y y + k_z z) \quad (3.1)$$

Where ω is the wave frequency, $\vec{k} = k_x \vec{e}_x + k_y \vec{e}_y + k_z \vec{e}_z$ is the wavenumber vector, $\vec{r} = x \vec{e}_x + y \vec{e}_y + z \vec{e}_z$ is the position vector, and t is time.

Note that as an observer travels with the wave along the ray path, it will always see or experience the same frequency. In the most general case, the wavenumber vector in (3.1) is given by

$$\vec{k}(x, y, z) = k_x(x, y, z) \vec{e}_x + k_y(x, y, z) \vec{e}_y + k_z(x, y, z) \vec{e}_z \quad (3.2)$$

The rate of change of the wavenumber components can be approximated as follows

$$\frac{\partial \vec{k}(x, y, z)}{\partial x} \approx \frac{\partial k_x(x, y, z)}{\partial x} \vec{e}_x \quad (3.3)$$

This is equivalent to assuming that the wave vector dependence with space is

$$\vec{k}(x, y, z) \approx k_x(x) \vec{e}_x + k_y(y) \vec{e}_y + k_z(z) \vec{e}_z \quad (3.4)$$

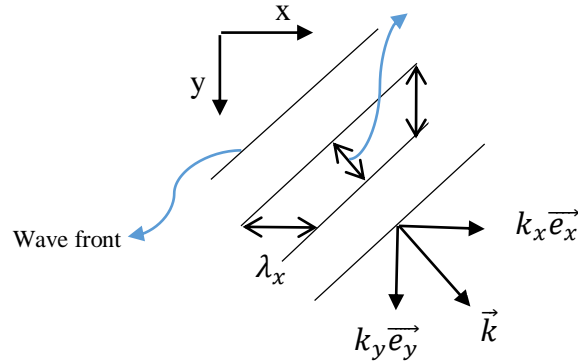


Figure 3.1: Illustration of 2D Wave propagation in homogeneous media at a specific instant in time. Wavenumber vector and its components are shown as well as the wavelength components and wave fronts.

According to the assumption in equation (3.4), a wave propagating in three-dimensional space can be separated in its three components. Figure 3.1 shows a wave propagating parallel to the x-y plane (2D case). Its wavefronts (surfaces of constant phase) and wavenumber components are shown. Likewise, the wavelength is also separated into its spatial components according to (3.4).

A graphical representation of an acoustic wave propagating in the x-component is shown in Figure 3.2. Figure 3.2a shows an acoustic wave propagating at a time $t = \tau_0$. In this case, the acoustic wave's phase $\alpha = \omega t - k_x x$ fluctuates with a specific periodicity. That is, the phase repeats itself when it changes by 2π or the acoustic pressure amplitude changes by a single wavelength λ_x . For a positive travelling wave in the x-direction this is mathematically expressed as

$$(\omega t - k_x x) = [\omega t - k_x (x + \lambda_x)] = (\omega t - k_x x + 2\pi) \quad (3.5)$$

From equation (3.5), it is inferred that

$$k_x = -\frac{2\pi}{\lambda_x} \quad (3.6)$$

If the same procedure is followed for waves in the y and z components, their wavenumbers are

$$k_y = -\frac{2\pi}{\lambda_y} \quad (3.7)$$

$$k_z = -\frac{2\pi}{\lambda_z} \quad (3.8)$$

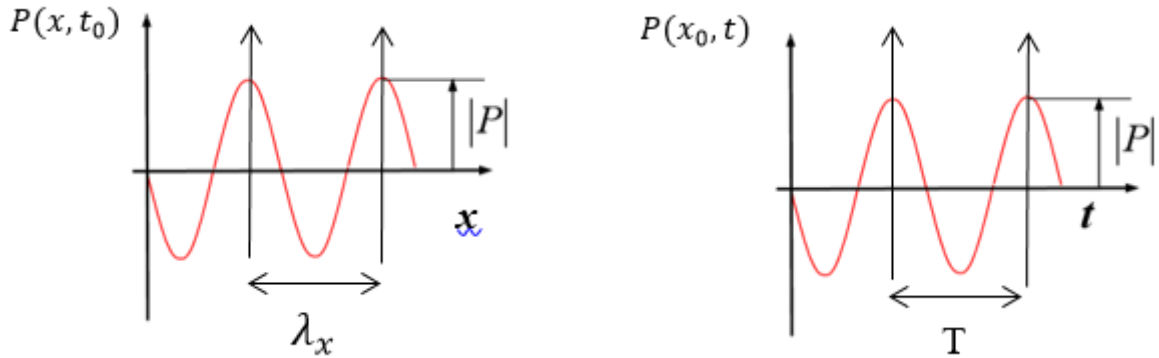


Figure 3.2: Representation of an acoustic wave traveling exclusively along the x direction for (a) acoustic pressure variation at time $t = \tau_0$, (b) acoustic pressure time variation at a location $x = x_0$.

The analysis used to obtain equations (3.6) through (3.8) is analogous to computing the rate of change of phase with respect to x , y , and z while assuming the condition in (3.4) as true. That is

$$\frac{\partial \alpha}{\partial x} = -k_x = \frac{-2\pi}{\lambda_x} \quad (3.9)$$

$$\frac{\partial \alpha}{\partial y} = -k_y = \frac{-2\pi}{\lambda_y} \quad (3.10)$$

$$\frac{\partial \alpha}{\partial z} = -k_z = \frac{-2\pi}{\lambda_z} \quad (3.11)$$

On the other hand, Figure 3.2b shows an acoustic wave at a location $x = x_0$, where acoustic pressure changes with time only. In this case, the acoustic wave's phase $\alpha_x = \omega t - k_x x$ fluctuates with a specific periodicity. That is, the phase repeats itself when it changes by 2π or the acoustic pressure amplitude changes by a single period T . Mathematically, this is

$$(\omega t - k_x x) = [\omega(t + T) - k_x x] = (\omega t - k_x x + 2\pi) \quad (3.12)$$

Equation (3.12) results in

$$\omega = \frac{2\pi}{T} \quad (3.13)$$

Thus, the acoustic wave's frequency is the rate of change of the phase with respect to time. Mathematically, this is

$$\frac{\partial \alpha}{\partial t} = \omega = \frac{2\pi}{T} \quad (3.14)$$

Equations (3.9) through (3.11) and (3.14) are the basis for constructing acoustic ray paths. It is still necessary to characterize the frequency dependency in space in order to account for local changes in the speed of sound or wind. This is addressed in the following sections.

Homogeneous Media

The path followed by a ray depends if the media is considered homogeneous or inhomogeneous. The first one corresponds to the case where temperature is uniformly distributed within the media. The second one corresponds to the case where temperature has a non-uniform spatial distribution. Rays follow a straight path when the media is homogeneous. However, this is not the case for actual atmospheric conditions. In reality, as acoustic rays propagate along the atmosphere they bend due to spatial gradients in the speed of sound. Gradients in the speed of sound are a result of temperature variation. This section will provide initial insight on how to treat acoustic rays propagating in homogeneous media and a windless condition.

In homogeneous media, frequency is characterized by the following three dimensional dispersion relationship

$$\omega = f(k_x, k_y, k_z) \quad (3.15)$$

The dispersion relationship defines the parameters of dependency of the acoustic wave's frequency, and changes depending on the media's homogeneity. The rays in a media with a frequency dependency such as the one given in (3.15) will disperse separately following unique paths. The dispersion relationship is physically interpreted as follows. Individual rays consist of an acoustic wave having a specific and unique frequency. The path followed by each of them has to be the one that maintains a frequency constant as it propagates. Thus, if equation (3.15) is true, the rays propagate with constant wavenumber components equal to the initial ones. The result is rays propagating through straight paths. This is demonstrated mathematically next.

The dispersion relationship in (3.15), combined with the phase rate relationships in (3.9) through (3.11) and (3.14) determine a set of equations that relate the following parameters: wavenumber, frequency and spatial location of a ray at specific propagation times. The assumption on (3.4) is maintained.

By differentiating (3.14) x , y , and z , and considering (3.15), then

$$\frac{\partial^2 \alpha}{\partial t \partial x} = \frac{\partial \omega}{\partial k_x} \frac{\partial k_x}{\partial x} \quad (3.16)$$

$$\frac{\partial^2 \alpha}{\partial t \partial y} = \frac{\partial \omega}{\partial k_y} \frac{\partial k_y}{\partial y} \quad (3.17)$$

$$\frac{\partial^2 \alpha}{\partial t \partial z} = \frac{\partial \omega}{\partial k_z} \frac{\partial k_z}{\partial z} \quad (3.18)$$

On the other hand, by differentiating (3.9) through (3.11) with respect to time t , the results are

$$\frac{\partial^2 \alpha}{\partial t \partial x} = -\frac{\partial k_x}{\partial t} \quad (3.19)$$

$$\frac{\partial^2 \alpha}{\partial t \partial y} = -\frac{\partial k_y}{\partial t} \quad (3.20)$$

$$\frac{\partial^2 \alpha}{\partial t \partial z} = -\frac{\partial k_z}{\partial t} \quad (3.21)$$

By equating (3.16) through (3.18), with (3.19) through (3.21) respectively, gives

$$\frac{\partial k_x}{\partial t} + \frac{\partial \omega}{\partial k_x} \frac{\partial k_x}{\partial x} = 0 \quad (3.22)$$

$$\frac{\partial k_y}{\partial t} + \frac{\partial \omega}{\partial k_y} \frac{\partial k_y}{\partial y} = 0 \quad (3.23)$$

$$\frac{\partial k_z}{\partial t} + \frac{\partial \omega}{\partial k_z} \frac{\partial k_z}{\partial z} = 0 \quad (3.24)$$

For demonstrative purposes, only equation (3.22) will be solved since the same process should be followed for (3.23) and (3.24) separately.

For the derivation of equations (3.9) through (3.14), it was assumed that the acoustic wavenumber was constant with time. However, this assumption is not completely correct. In order to track a ray path in space, the wavenumber has to be tracked in time also. Any changes in the wavenumber during propagation will alter the ray path. Therefore, for equation (3.22), $k_x = f(x, t)$ must be tracked along the ray path. To do so, the first step is to parametrize $k_x(x, t)$ such that $x = x(s)$ and $t = t(s)$. Thus, by the chain rule the derivative of $k_x(x(s), t(s))$ is

$$\frac{\partial k_x}{\partial s} = \frac{\partial k_x}{\partial t} \frac{dt}{ds} + \frac{\partial k_x}{\partial x} \frac{dx}{ds} \quad (3.25)$$

where the parameter s corresponds to the distance along the ray path followed by the acoustic wave as it propagates. The objective of the parametrization is to find the conditions under which the right hand side of (3.25) is equal to the left hand side of (3.22), so that the variation of the wavenumber in the x-direction given by the PDE in (3.22) is bounded by its variation along the ray path s . In this case, this means that

$$\frac{\partial k_x}{\partial t} + \frac{\partial \omega}{\partial k_x} \frac{\partial k_x}{\partial x} = \frac{\partial k_x}{\partial s} = 0 \quad (3.26)$$

This implies that the wavenumber component in the x-direction is always constant along a ray path. It is found that the conditions that allow this to be true are

$$\frac{dt}{ds} = 1 \quad (3.27)$$

$$\frac{dx}{ds} = \frac{\partial \omega}{\partial k_x} \quad (3.28)$$

If (3.27) and (3.28) are solved, then

$$t = s + C_t(\xi) \quad (3.29)$$

$$x = \frac{\partial \omega}{\partial k_x} s + C_x(\xi) = \frac{\partial \omega}{\partial k_x} t + C_x(\xi) \quad (3.30)$$

where, $C_t(\xi)$ and $C_x(\xi)$ correspond to the time and x-component integration constants. Both of them are defined to be dependable of a new variable ξ . In order to find these constants of integration, initial conditions have to be assigned. These are, at time $t = 0$, $s = 0$ and $x = \xi$. This gives $C_t(\xi) = 0$ and $C_x(\tau) = \xi$. This means that (3.29) and (3.30) are equivalent to

$$t = s \quad (3.31)$$

$$x - \frac{\partial \omega}{\partial k_x} t = \xi = C_{[x]}(\xi) \quad (3.32)$$

This equation has a straight forward solution for ray paths in homogeneous media. Even though the rate $\partial \omega / \partial k_x$ is not known in most cases, equation (3.26) proves that $\partial k_x / \partial s = 0$ and thus k_x depends only on the variable ξ , the initial condition for x. That is, a ray propagating in a homogeneous media will always be straight line over the x-t domain and its wavenumber will be

defined by the wavenumber at the emission time. It is important to note that equation (3.32) applies only for non-moving media i.e. it does not take wind speed into account. This will be considered later in this chapter.

The solution method presented above is known as the method of characteristics to solve quasi-linear PDEs (Zauderer, 2006). It was presented here for the simple homogeneous case for the main purpose of introducing the reader to this method. The method of characteristics will be used in the more complicated case of a moving inhomogeneous media.

By the method of characteristics, a graphic interpretation of the acoustic ray paths for homogeneous media can be constructed. Figure 3.3 shows how rays behave in the (x, s, k_x) domain for homogeneous media. Depending on the x-component initial condition, rays follow a straight line while maintaining the wavenumber component constant. These correspond to the characteristic curves that form an integral surface. The projection of the characteristic curves in the x-t plane show the real linear acoustic ray component during propagation.

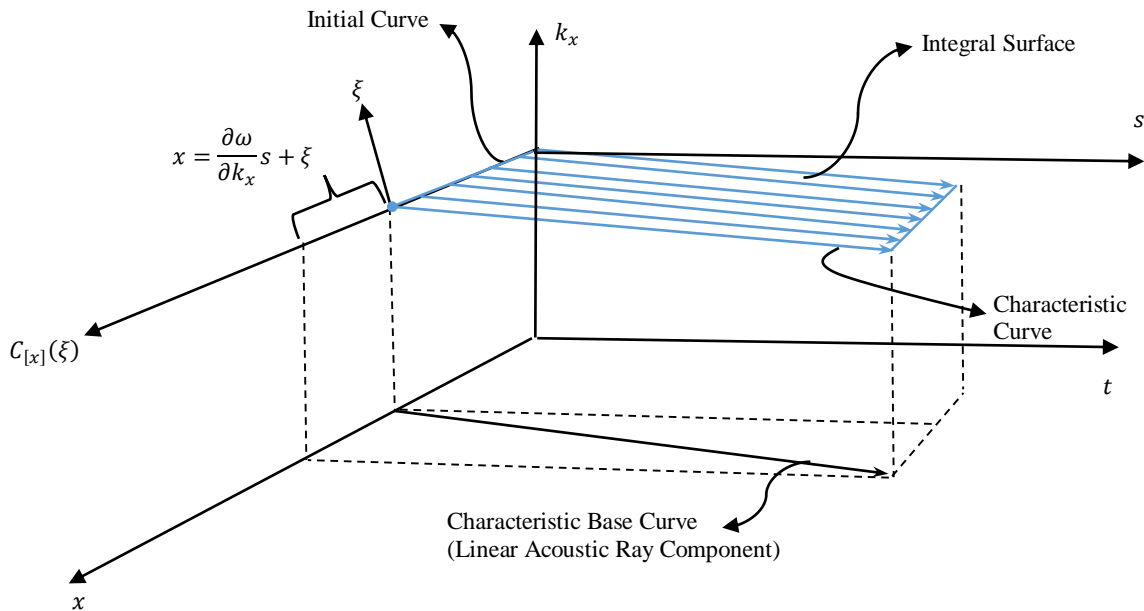


Figure 3.3: Homogeneous media's characteristic surface and curves.

The method of characteristics can be applied to the equations (3.23) and (3.24) separately. Each on the (y, s, k_y) , and (z, s, k_z) domains respectively. Therefore, it is possible to trace acoustic rays

in a homogeneous non-moving media by using the following equations

$$x = \xi_x + \frac{\partial \omega}{\partial k_x} t \quad (3.33)$$

$$y = \xi_y + \frac{\partial \omega}{\partial k_y} t \quad (3.34)$$

$$z = \xi_z + \frac{\partial \omega}{\partial k_z} t \quad (3.35)$$

where, τ_x , τ_y , and τ_z correspond to the initial ray's location in the x, y, and z spatial components.

Inhomogeneous Media

If an inhomogeneous media is considered in a windless condition, acoustic refraction alters ray paths into curved ones. The dispersion relationship is then given by

$$\omega = f(x, y, z, k_x, k_y, k_z) \quad (3.36)$$

This expression states that while a ray propagates, the wavenumber will change with space (thus, the dependence on x, y, z) in such a way that the frequency is constant (equivalent to the frequency of the source). In this case, by differentiating (3.14) x, y, and z, and acknowledging that (3.36) is true, then

$$\frac{\partial^2 \alpha}{\partial t \partial x} = \frac{\partial \omega}{\partial k_x} \frac{\partial k_x}{\partial x} + \frac{\partial \omega}{\partial x} \quad (3.37)$$

$$\frac{\partial^2 \alpha}{\partial t \partial y} = \frac{\partial \omega}{\partial k_y} \frac{\partial k_y}{\partial y} + \frac{\partial \omega}{\partial y} \quad (3.38)$$

$$\frac{\partial^2 \alpha}{\partial t \partial z} = \frac{\partial \omega}{\partial k_z} \frac{\partial k_z}{\partial z} + \frac{\partial \omega}{\partial z} \quad (3.39)$$

The assumption in (3.4) is also taken into account for this case. By combining these equations with

those in (3.19) through (3.21), the following is obtained

$$\frac{\partial \omega}{\partial k_x} \frac{\partial k_x}{\partial x} + \frac{\partial k_x}{\partial t} = -\frac{\partial \omega}{\partial x} \quad (3.40)$$

$$\frac{\partial \omega}{\partial k_y} \frac{\partial k_y}{\partial y} + \frac{\partial k_y}{\partial t} = -\frac{\partial \omega}{\partial y} \quad (3.41)$$

$$\frac{\partial \omega}{\partial k_z} \frac{\partial k_z}{\partial z} + \frac{\partial k_z}{\partial t} = -\frac{\partial \omega}{\partial z} \quad (3.42)$$

These are non-linear PDEs known as quasi-linear PDEs (Zauderer, 2006). In order to solve for the ray path of waves propagating in inhomogeneous media, the quasilinear PDEs in (3.40) through (3.42) must be simplified so that they are easily solved with numerical methods. To do so, the PDEs are expressed as the inner product of two vectors in space-time-wavenumber domain, that is

$$\left(\vec{t} + \frac{\partial \omega}{\partial k_x} \vec{x} - \frac{\partial \omega}{\partial x} \vec{k}_x \right) \cdot \left(\frac{\partial k_x}{\partial t} \vec{t} + \frac{\partial k_x}{\partial x} \vec{x} - \vec{k}_x \right) = 0 \quad (3.43)$$

$$\left(\vec{t} + \frac{\partial \omega}{\partial k_y} \vec{y} - \frac{\partial \omega}{\partial y} \vec{k}_y \right) \cdot \left(\frac{\partial k_y}{\partial t} \vec{t} + \frac{\partial k_y}{\partial y} \vec{y} - \vec{k}_y \right) = 0 \quad (3.44)$$

$$\left(\vec{t} + \frac{\partial \omega}{\partial k_z} \vec{z} - \frac{\partial \omega}{\partial z} \vec{k}_z \right) \cdot \left(\frac{\partial k_z}{\partial t} \vec{t} + \frac{\partial k_z}{\partial z} \vec{z} - \vec{k}_z \right) = 0 \quad (3.45)$$

The solution procedure for each of the three equations is identical. Therefore, in this section, the procedure will be shown only for equation (3.43).

The vector to the left of each of (3.43) is the tangent to a characteristic line over an integral surface constructed in the space-time-wavenumber domain as shown in Figure 3.4. Only the spatial components associated with (3.43) are shown, i.e. the integral surface is defined only on the (x, t, k_x) domain.

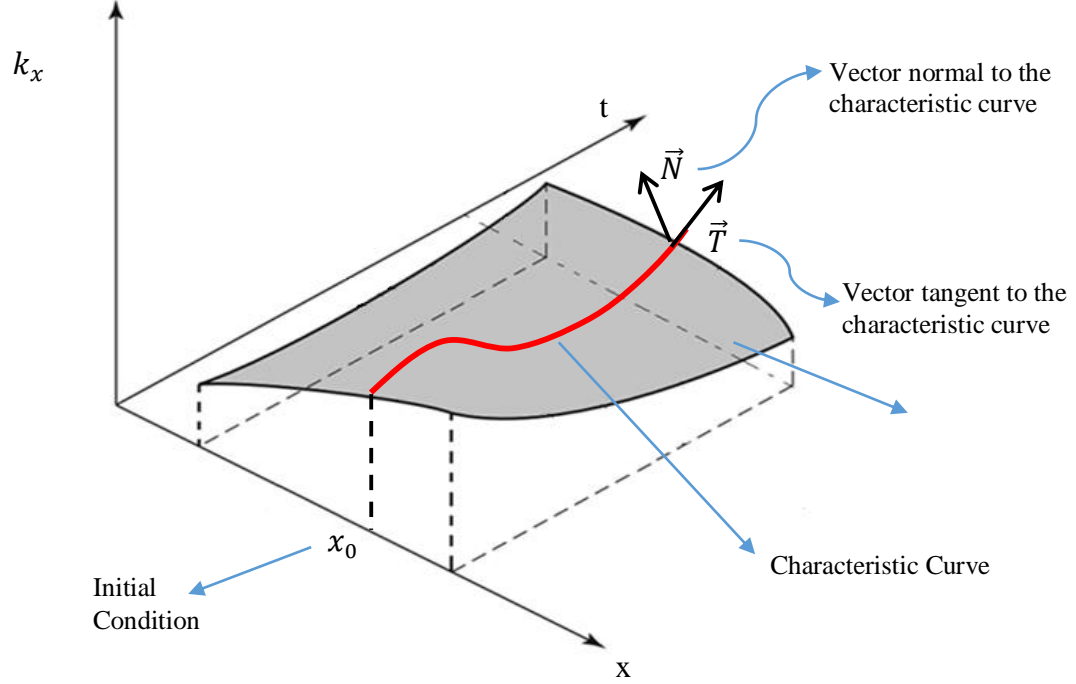


Figure 3.4: Integral surface and characteristic curve over (x, t, k_x) space.

A characteristic curve starting at a specified initial condition is highlighted in red over the integral surface. It corresponds to an assumed solution for the first PDE in (3.40) given a specific initial condition x_0 . This curve is formulated by parametrizing it about s and acknowledging that its derivative about s is both tangent to the characteristic curve and to the integral surface. The parameter s corresponds to the distance along the ray path followed by the acoustic wave as it propagates. Therefore,

$$\frac{d\vec{C}}{ds} = \frac{dt}{ds} \vec{t} + \frac{dx}{ds} \vec{x} + \frac{dk_x}{ds} \vec{k}_x \quad (3.46)$$

This is the vector equation of the characteristic curve in Figure 3.4. This means that it is possible to equate the vector $d\vec{C}/ds$ with the vector to the left on the first expression in (3.43). Mathematically this results in

$$\frac{dt}{ds} = 1, \quad \frac{dx}{ds} = \frac{\partial \omega}{\partial k_x}, \quad \frac{dk_x}{ds} = -\frac{\partial \omega}{\partial x} \quad \text{same as} \quad \frac{\partial \omega}{\partial k_x} \frac{\partial k_x}{\partial x} + \frac{\partial k_x}{\partial t} = -\frac{\partial \omega}{\partial x} \quad (3.47)$$

Note that the PDE in (3.40) is reduced to three equations shown in (3.47). They can be further

simplified by using $dt = ds$. If the same procedure is followed for (3.44) and (3.45), then the following set of coupled first PDEs is obtained

$$\frac{dx}{dt} = \frac{\partial \omega}{\partial k_x} \quad \text{and} \quad \frac{dk_x}{dt} = -\frac{\partial \omega}{\partial x} \quad (3.48)$$

$$\frac{dy}{dt} = \frac{\partial \omega}{\partial k_y} \quad \text{and} \quad \frac{dk_y}{dt} = -\frac{\partial \omega}{\partial y} \quad (3.49)$$

$$\frac{dz}{dt} = \frac{\partial \omega}{\partial k_z} \quad \text{and} \quad \frac{dk_z}{dt} = -\frac{\partial \omega}{\partial z} \quad (3.50)$$

The solution of these set of equations gives the ray path in an inhomogeneous windless media.

Inhomogeneous Moving Media

The set of PDEs in (3.48) through (3.50) are analogous to Hamilton's equations for dynamical systems. Thus, the denomination of "*Hamiltonian ray tracing*" to this method. This type of equations can be easily solved by using numerical methods. However, an expression for frequency is still required in order to proceed.

A Doppler effect due to wind flow effects is created between a stationary point of view and a relative one moving with the local wind velocity $\vec{V} = (V_x, V_y, V_z)$. This phenomenon affects frequency dispersion relationship in the media and accounts for wind convective and bending ray effects in the model. The frequency of acoustic oscillations occurring at a point moving with wind velocity is defined as the relative frequency ω_r . On the other hand, the frequency of oscillations occurring at a fixed point in space is defined as the absolute frequency ω . Both of them are related by

$$\omega = \omega_r + (V_x k_x + V_y k_y + V_z k_z) \quad (3.51)$$

This corresponds to a full Doppler formulation where all components of wind (including the vertical one) are taken into account for changes in frequency of the acoustic wave during propagation.

The relative frequency during propagation of a ray is always assumed constant and the same to the

emitted frequency at the source. This condition must be met while the ray propagates through arbitrary media with conditions that include variations of the speed of sound and the presence of wind. Therefore, in order to capture the media's conditions, it is convenient to define ω_r as follows

$$\omega_r = c(x, y, z) |\vec{k}| = c(x, y, z) \sqrt{k_x^2 + k_y^2 + k_z^2} \quad (3.52)$$

The expression in (3.52) for the relative frequency follows the dispersion relationship for inhomogeneous media.

From the expressions in (3.48) through (3.50), it is observed that the derivatives of the absolute frequency with respect to location and wavenumbers are required. Each pair of expressions in (3.48) through (3.50) are solved by following the same procedure. In this section, only the procedure for the first pair in (3.48) is shown. First, the derivative of the absolute frequency with respect to the wavenumber k_x is determined. That is,

$$\frac{\partial \omega}{\partial k_x} = \frac{\partial \omega_r}{\partial k_x} + V_x \quad (3.53)$$

where, the derivative of relative frequency with respect to the wavenumber k_x gives

$$\frac{\partial \omega_r}{\partial k_x} = c \frac{\partial \omega_r}{\partial k_x} = c \frac{k_x}{\sqrt{k_x^2 + k_y^2 + k_z^2}} = c \frac{k_x}{|\vec{k}|} \quad (3.54)$$

On the other hand, the derivative of the absolute frequency with respect to x is also necessary. The expression for this is the following

$$\frac{\partial \omega}{\partial x} = \frac{\partial \omega_r}{\partial x} + k_x \frac{\partial V_x}{\partial x} + k_y \frac{\partial V_y}{\partial x} + k_z \frac{\partial V_z}{\partial x} \quad (3.55)$$

Note that by the method of characteristics in (3.47) k_x depends exclusively on the ray path

parameter s or equivalent time parameter t . Therefore, in (3.55) k_x is analyzed under the mathematical conjecture that $\partial k_x / \partial x = 0$ (see equation (3.46)).

Finally, by using (3.52), the first term in the term in (2.53) results in

$$\frac{\partial \omega_r}{\partial x} = \frac{\partial c}{\partial x} \left| \vec{k} \right| \quad (3.56)$$

Following this procedure, the resultant modified equations after incorporating frequency changes due to wind into (3.48) through (3.50) are the following

$$\begin{aligned} \frac{dx}{dt} &= c \frac{k_x}{\sqrt{k_x^2 + k_y^2 + k_z^2}} + V_x & \text{and} & \quad \frac{dk_x}{dt} = -\sqrt{k_x^2 + k_y^2 + k_z^2} \frac{\partial c}{\partial x} - k_x \frac{\partial V_x}{\partial x} - k_y \frac{\partial V_y}{\partial x} - k_z \frac{\partial V_z}{\partial x} \\ \frac{dy}{dt} &= c \frac{k_y}{\sqrt{k_x^2 + k_y^2 + k_z^2}} + V_y & \text{and} & \quad \frac{dk_y}{dt} = -\sqrt{k_x^2 + k_y^2 + k_z^2} \frac{\partial c}{\partial y} - k_x \frac{\partial V_x}{\partial y} - k_y \frac{\partial V_y}{\partial y} - k_z \frac{\partial V_z}{\partial y} \\ \frac{dz}{dt} &= c \frac{k_z}{\sqrt{k_x^2 + k_y^2 + k_z^2}} + V_z & \text{and} & \quad \frac{dk_z}{dt} = -\sqrt{k_x^2 + k_y^2 + k_z^2} \frac{\partial c}{\partial z} - k_x \frac{\partial V_x}{\partial z} - k_y \frac{\partial V_y}{\partial z} - k_z \frac{\partial V_z}{\partial z} \end{aligned} \quad (3.57)$$

All equations on the left of (3.57) are referred to as the Hamiltonian Location Equations (HLE), while all equations on the right of (3.57) are referred to as the Hamiltonian Wavenumber Equations (HWE). These correspond to the final form of the system that must be solved for the spatial components (x, y, z) that define a single ray's location during propagation, and its corresponding acoustic wavenumber components (k_x, k_y, k_z) . Thus, in order to propagate a single ray, its initial conditions must be known (initial wavenumber, local speed of sound, location of the source, wind speed at source location, and frequency emitted). This model is physically very accurate because it accepts all velocity components of wind, as well as variations on the speed of sound in any direction. Therefore, simulations that seek considerable accuracy require a complete 3D wind field over the desired propagation volume.

From an initial assessment of the Hamiltonian equations in (3.57), one is able to conclude the

following: i) the location of a ray during propagation is controlled by the wavenumber vector and ii) changes on the acoustic ray's wavenumber are affected only if there are speed of sound and wind speed gradients present in the media. However, recall that by the method of characteristics in equations (3.46) and (3.55), k_x, k_y, k_z were not dependent of $x, y,$ and z but only on the ray parameter s . Physically, this is interpreted as follows. The HWE only account for the changes of wavenumber due to bending effects along the ray path defined by s . This wavenumber is defined as \vec{k}_{bend} . While the HLE implicitly takes into account changes in the wavenumber due to convective effects (wind velocity) and is defined as \vec{k}_{conv} . This means that all the wavenumber components in equations (3.57) correspond only to the components of \vec{k}_{bend} . There is no necessity of computing \vec{k}_{conv} because the HLE computes directly the new location of the ray using the wind velocity vector \vec{V} . This is graphically shown in Figure 3.5.

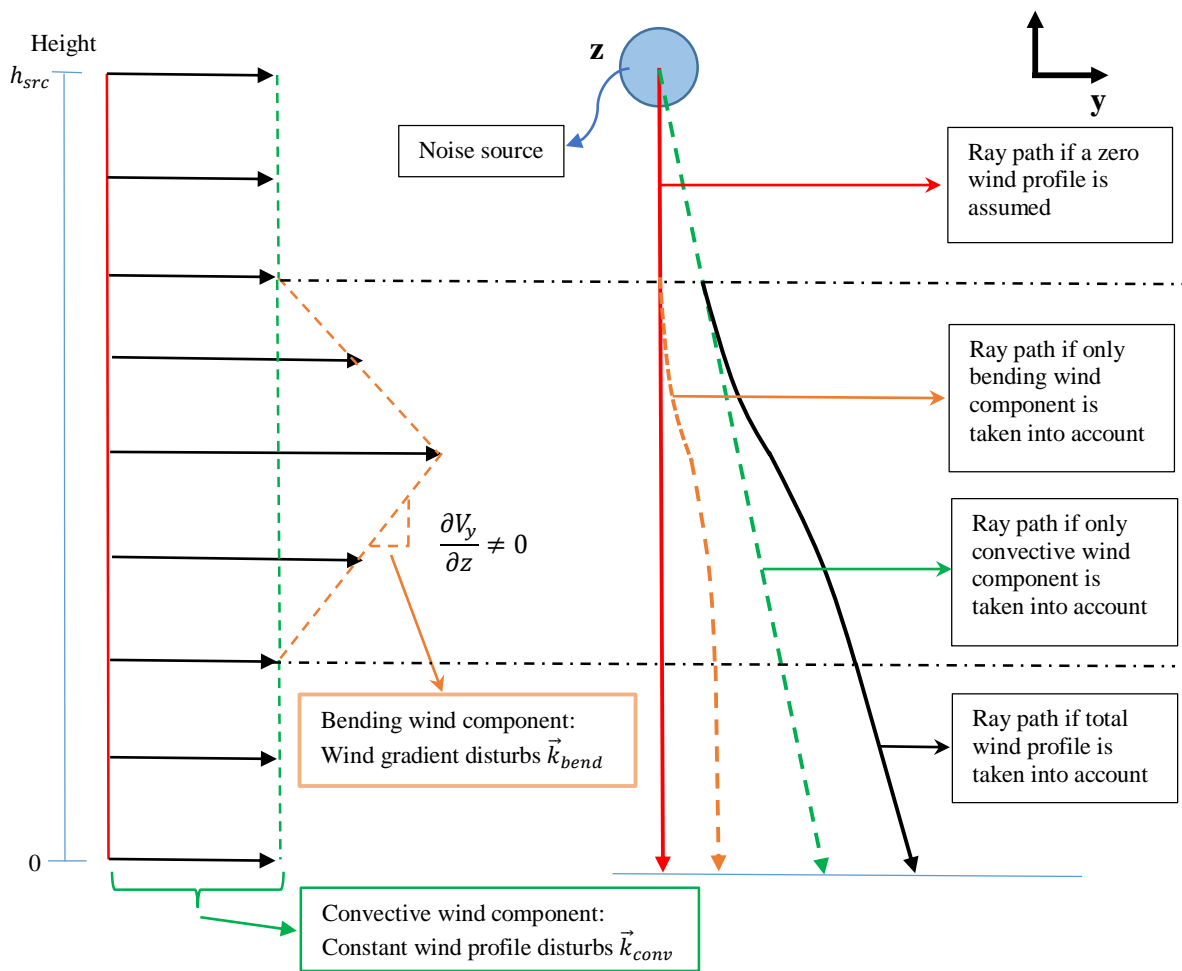


Figure 3.5: Wind profile and propagating ray path components.

Figure 3.5 shows a source located at a height h_{src} in a media where the speed of sound is constant. If zero wind is considered and a single ray is emitted directly towards the ground, the ray will propagate as a straight vertical line (ray path shown in red). If the same ray is propagated towards the ground but there is a constant wind profile in the media, then its path will be convected (ray path shown in green), where $d\vec{k}_{conv}/ds \neq \vec{0}$ and $d\vec{k}_{bend}/ds = \vec{0}$ during propagation. On the other hand, if a bending wind profile such that $\partial V_y/\partial z \neq 0$ is considered (orange line), then $d\vec{k}_{conv}/ds = \vec{0}$ and $d\vec{k}_{bend}/ds \neq \vec{0}$ during propagation, causing the ray to bend (ray path shown in orange). Finally, if a wind profile containing both the convective and bending components is taken into account, then $d\vec{k}_{conv}/ds \neq \vec{0}$ and $d\vec{k}_{bend}/ds \neq \vec{0}$ during propagation, causing the ray to convect and bend along its path (ray path shown in black).

Finally, it is valuable to mention that the more common Eikonal ray tracing method is based on an asymptotic series solution to the acoustic Helmholtz equation. In this case, a complex nonlinear PDE must be solved and moving media is usually taken into account by assuming an effective speed of sound i.e. adding to the speed of sound to the horizontal component of wind velocity in the direction of propagation (Bowdler et al., 2012). Furthermore, the Eikonal equations track the acoustic wavefronts during propagation instead of wavenumbers in order to define the ray paths.

Numerical Solution of the Ray Paths

Runge-Kutta (RK) methods are used to solve the system of equations presented in (3.57). Numerical accuracy depends on the selected order of the RK and time step taken during propagation. Furthermore, these two parameters and the total simulation time are the prime factors that affect the computational efficiency of this technique. This numerical solution procedure is addressed in this section. Given that measured meteorological weather conditions data is commonly presented as vertical profiles, e.g. wind and temperature depends only on height, it is convenient to show how the Hamiltonian ray path equations are numerically solved for this special case.

Considering temperature and wind velocity change only with height (z), the equations in (3.57) become

$$\frac{dx}{dt} = c \frac{k_x}{\sqrt{k_x^2 + k_y^2 + k_z^2}} + V_x \text{ and } \frac{dk_x}{dt} = 0 \quad (3.58)$$

$$\frac{dy}{dt} = c \frac{k_y}{\sqrt{k_x^2 + k_y^2 + k_z^2}} \text{ and } \frac{dk_y}{dt} = 0$$

$$\frac{dz}{dt} = c \frac{k_z}{\sqrt{k_x^2 + k_y^2 + k_z^2}} \text{ and } \frac{dk_z}{dt} = -\sqrt{k_x^2 + k_y^2 + k_z^2} \frac{\partial c}{\partial z} - k_x \frac{\partial V_x}{\partial z}$$

The equations that are equal to zero do not have to be solved. However, the following four equations still require a solution

$$\frac{dx}{dt} = c \frac{k_x}{\sqrt{k_x^2 + k_y^2 + k_z^2}} + V_x \quad (3.59)$$

$$\frac{dy}{dt} = c \frac{k_y}{\sqrt{k_x^2 + k_y^2 + k_z^2}}$$

$$\frac{dz}{dt} = c \frac{k_z}{\sqrt{k_x^2 + k_y^2 + k_z^2}}$$

$$\frac{dk_z}{dt} = -\sqrt{k_x^2 + k_y^2 + k_z^2} \frac{\partial c}{\partial z} - k_x \frac{\partial V_x}{\partial z}$$

These equations can be numerically solved via a second order Runge-Kutta method. This method is based on a numerical trapezoidal approximation for an integral (Hairer, 2008). To solve a first order differential equation such as $dx/dt = f(x, t)$, its integral is approximated with the trapezoidal rule as follows

$$x_{n+1} - x_n = \int_{t_n}^{t_{n+1}} f(x, t) dt \approx \frac{\Delta t}{2} [f(x_n, t_n) + f(x_{n+1}, t_{n+1})] \quad (3.60)$$

Where, n corresponds to a discrete time subscript. Since x_{n+1} is not known it must be approximated using forward Euler's rule: $x_{n+1} \approx x_n + \Delta t f(x_n, t_n)$. Thus, the Runge-Kutta must follow the next steps:

1. Evaluate $f(x_n, t_n)$ and define it as $R_1 = f(x_n, t_n)$.

2. Apply Euler's rule by computing $x_n + \Delta t R_1 = x_n + \Delta t f(x_n, t_n)$.
3. Evaluate $f(x_n + \Delta t R_1, t_{n+1})$ and define it as $R_2 = f(x_n + \Delta t R_1, t_{n+1})$.
4. Apply the trapezoidal rule to obtain $x_{n+1} = x_n + \frac{\Delta t}{2}(R_1 + R_2)$.

This is an iterative procedure method. If this procedure is applied to the Hamiltonian equations in (3.58), then the steps become the following

1. Evaluate the functions at t_n :

Solve for ray path location

$$\begin{aligned}
 R_{1,x} &= c(x_n, y_n, z_n) \frac{k_{x,n}}{\sqrt{k_{x,n}^2 + k_{y,n}^2 + k_{z,n}^2}} + V_{x,n}(x_n, y_n, z_n) \\
 R_{1,y} &= c(x_n, y_n, z_n) \frac{k_{y,n}}{\sqrt{k_{x,n}^2 + k_{y,n}^2 + k_{z,n}^2}} + V_{y,n}(x_n, y_n, z_n) \\
 R_{1,z} &= c(x_n, y_n, z_n) \frac{k_{z,n}}{\sqrt{k_{x,n}^2 + k_{y,n}^2 + k_{z,n}^2}} + V_{z,n}(x_n, y_n, z_n)
 \end{aligned} \tag{3.61}$$

Solve for wavenumber

$$\begin{aligned}
 R_{1,k_x} &= 0 \\
 R_{1,k_y} &= 0 \\
 R_{1,k_z} &= -\sqrt{k_{x,n}^2 + k_{y,n}^2 + k_{z,n}^2} \frac{\partial c}{\partial z}(x_n, y_n, z_n) - k_{x,n} \frac{\partial V_x}{\partial z}(x_n, y_n, z_n)
 \end{aligned} \tag{3.62}$$

2. Apply Euler's rule:

Solve for ray path location

$$\begin{aligned}
x_n + \Delta t R_{1,x} &= x_n + \Delta t \left(c(x_n, y_n, z_n) \frac{k_{x,n}}{\sqrt{k_{x,n}^2 + k_{y,n}^2 + k_{z,n}^2}} + V_{x,n}(x_n, y_n, z_n) \right) \\
y_n + \Delta t R_{1,y} &= y_n + \Delta t \left(c(x_n, y_n, z_n) \frac{k_{y,n}}{\sqrt{k_{x,n}^2 + k_{y,n}^2 + k_{z,n}^2}} + V_{y,n}(x_n, y_n, z_n) \right) \\
z_n + \Delta t R_{1,z} &= z_n + \Delta t \left(c(x_n, y_n, z_n) \frac{k_{z,n}}{\sqrt{k_{x,n}^2 + k_{y,n}^2 + k_{z,n}^2}} + V_{z,n}(x_n, y_n, z_n) \right)
\end{aligned} \tag{3.63}$$

Solve for wavenumber

$$\begin{aligned}
k_{x,n} + \Delta t R_{1,k_x} &= k_{x,n} + \Delta t (0) \\
k_{y,n} + \Delta t R_{1,k_y} &= k_{y,n} + \Delta t (0) \\
k_{z,n} + \Delta t R_{1,k_z} &= k_{z,n} + \Delta t \left(-\sqrt{k_{x,n}^2 + k_{y,n}^2 + k_{z,n}^2} \frac{\partial c}{\partial z}(x_n, y_n, z_n) - k_{x,n} \frac{\partial V_x}{\partial z}(x_n, y_n, z_n) \right)
\end{aligned} \tag{3.64}$$

3. Evaluate the functions at t_{n+1}

Solve for ray path location

$$\begin{aligned}
R_{2,x} &= c(x_n + \Delta t R_{1,x}, y_n + \Delta t R_{1,y}, z_n + \Delta t R_{1,z}) \times \dots \\
&\quad \frac{k_{x,n} + \Delta t R_{1,k_x}}{\sqrt{\left(k_{x,n} + \Delta t R_{1,k_x}\right)^2 + \left(k_{y,n} + \Delta t R_{1,k_y}\right)^2 + \left(k_{z,n} + \Delta t R_{1,k_z}\right)^2}} + \dots \\
&\quad V_{x,n}(x_n + \Delta t R_{1,x}, y_n + \Delta t R_{1,y}, z_n + \Delta t R_{1,z}) \\
R_{2,y} &= c(x_n + \Delta t R_{1,x}, y_n + \Delta t R_{1,y}, z_n + \Delta t R_{1,z}) \times \dots \\
&\quad \frac{k_{y,n} + \Delta t R_{1,k_y}}{\sqrt{\left(k_{x,n} + \Delta t R_{1,k_x}\right)^2 + \left(k_{y,n} + \Delta t R_{1,k_y}\right)^2 + \left(k_{z,n} + \Delta t R_{1,k_z}\right)^2}} + \dots \\
&\quad V_{y,n}(x_n + \Delta t R_{1,x}, y_n + \Delta t R_{1,y}, z_n + \Delta t R_{1,z}) \\
R_{2,z} &= c(x_n + \Delta t R_{1,x}, y_n + \Delta t R_{1,y}, z_n + \Delta t R_{1,z}) \times \dots \\
&\quad \frac{k_{z,n} + \Delta t R_{1,k_z}}{\sqrt{\left(k_{x,n} + \Delta t R_{1,k_x}\right)^2 + \left(k_{y,n} + \Delta t R_{1,k_y}\right)^2 + \left(k_{z,n} + \Delta t R_{1,k_z}\right)^2}} + \dots \\
&\quad V_{z,n}(x_n + \Delta t R_{1,x}, y_n + \Delta t R_{1,y}, z_n + \Delta t R_{1,z})
\end{aligned} \tag{3.65}$$

Solve for wavenumber

$$\begin{aligned}
 R_{2,k_x} &= 0 \\
 R_{2,k_y} &= 0 \\
 R_{2,k_z} &= -\sqrt{\left(k_{x,n} + \Delta t R_{1,k_x}\right)^2 + \left(k_{y,n} + \Delta t R_{1,k_y}\right)^2 + \left(k_{z,n} + \Delta t R_{1,k_z}\right)^2} \frac{\partial c}{\partial z} \times \dots \\
 &\quad \left(x_n + \Delta t R_{1,x}, y_n + \Delta t R_{1,y}, z_n + \Delta t R_{1,z}\right) - \dots \\
 &\quad \left(k_{x,n} + \Delta t R_{1,k_x}\right) \frac{\partial V_x}{\partial z} \left(x_n + \Delta t R_{1,x}, y_n + \Delta t R_{1,y}, z_n + \Delta t R_{1,z}\right)
 \end{aligned} \tag{3.66}$$

4. Apply the trapezoidal rule

Solve for ray path location

$$\begin{aligned}
 x_{n+1} &= x_n + \frac{\Delta t}{2} \left(R_{1,x} + R_{2,x}\right) \\
 y_{n+1} &= y_n + \frac{\Delta t}{2} \left(R_{1,y} + R_{2,y}\right) \\
 z_{n+1} &= z_n + \frac{\Delta t}{2} \left(R_{1,z} + R_{2,z}\right)
 \end{aligned} \tag{3.67}$$

Solve for wavenumber

$$\begin{aligned}
 k_{x,n+1} &= k_{x,n} \\
 k_{y,n+1} &= k_{y,n} \\
 k_{z,n+1} &= k_{z,n} + \frac{\Delta t}{2} \left(R_{1,k_z} + R_{2,k_z}\right)
 \end{aligned} \tag{3.68}$$

Alternatively, a fourth order Runge-Kutta method, that iterates four times before obtaining the results at one-step further in time, can also be implemented. The details of the solution procedure for this case is shown in Appendix D.

3.2. ACOUSTIC PRESSURE FIELD

An acoustic ray that follows a path starting at the noise source and reaching an arbitrary observer always obeys Fermat's principle. It defines that a ray will always follow a path corresponding to the extremum of the wave's phase transit time, often referred to as the minimum-time path. This

physical phenomenon translates into rays bending due to local wave diffraction in inhomogeneous media and straight ray paths in homogeneous media. Both the Eikonal and Hamiltonian ray tracing methods account for this.

It is convenient to assume that any acoustic wave propagating in the vicinity of a minimum-time ray path must do so, with a nearly constant phase. Therefore, sound pressure levels in the far field (large propagation distances compared to the wave's wavelength) can be obtained by means of a ray-tube technique. A ray-tube is constructed as a bundle of acoustic rays enclosing a cross-sectional area that changes as the rays propagate. The acoustic waves within the tubes will coherently contribute to the total enclosed pressure fluctuations (Lighthill, 1978, pp. 190-191).

In order to determine far field spatial sound pressure levels distribution, an analysis on the continuity of acoustic energy along ray tubes has to be performed as they propagate. The following subsections addresses the conservation of energy applied to a ray-tube. Then, the procedure to obtain the SPL along the ray tubes is introduced. Finally, wind and atmospheric attenuation are also considered.

Conservation of Energy in a Ray-Tube

In order to characterize the energy flow within a ray tube, the system to be considered consists of a fluid element corresponding to an infinitesimal volume that contains millions of fluid molecules. It is therefore appropriate to work in terms of energy density or energy per unit volume. Additionally, the selected system is considered a conservative one, where the sum of kinetic and potential energy is always conserved (constant).

The first step is to define the kinetic energy density of a wavelike disturbance. In this case, the particle velocity of the fluid element is given by the vector $\vec{u} = (u, v, w)$, and the fluid's equilibrium density defined as ρ_0 . Thus, the kinetic energy per unit volume (energy density) is

$$E_k = \frac{1}{2} \rho_0 (u^2 + v^2 + w^2) \quad (3.69)$$

Even though the instantaneous density ρ should be used in (3.69), its variation is very small with respect to ρ_0 . Therefore, equation (3.69) still provides an accurate value of kinetic energy density.

On the other hand, the potential energy density is defined as the work done by the acoustic pressure P_{ac} during compression from the media's equilibrium density to the fluid's instantaneous density. The acoustic pressure in this case is equivalent to the difference between the instantaneous pressure P_{ins} and the media's equilibrium pressure P_{eq} . According to this, the potential energy density is given as

$$E_p = \int_{\rho_0}^{\rho} (P_{ins} - P_{eq}) \rho^{-1} d\rho = \int_{\rho_0}^{\rho} P_{ac} \rho^{-1} d\rho \quad (3.70)$$

In this case ρ can also be approximated to ρ_0 in order to facilitate the integration process. Equation (3.70) can be integrated by computing P_{ac} in terms of the instantaneous and equilibrium densities. To this end, a Taylor series expansion for the system's pressure about the equilibrium density can be defined as follows

$$P = P(\rho_0) + \frac{\partial P}{\partial \rho} \times (\rho - \rho_0) + \dots \quad (3.71)$$

If only the first two terms of the series are considered, and acknowledging that $P(\rho_0) = P_{eq}$, $P = P_{ins}$, and $\frac{\partial P}{\partial \rho} = c^2$, then P_{ac} is determined as

$$P_{ac} = P - P(\rho_0) = c^2 \times (\rho - \rho_0) \quad (3.72)$$

Furthermore, if (3.72) is replaced in (3.70) and the resulting expression is integrated, the potential energy density becomes

$$E_p = \int_{\rho_0}^{\rho} (\rho - \rho_0) c^2 \rho_0^{-1} d\rho = \frac{1}{2} (\rho - \rho_0)^2 c^2 \rho_0^{-1} = \frac{1}{2} P_{ac}^2 c^{-2} \rho_0^{-1} \quad (3.73)$$

In turn, the total energy density contained within the system must be equal to the sum of both the potential and kinetic components, that is

$$E_T = E_p + E_k = \frac{1}{2} P_{ac}^2 c^{-2} \rho_0^{-1} + \frac{1}{2} \rho_0 (u^2 + v^2 + w^2) \quad (3.74)$$

Equation (3.74) can be expressed in terms of the velocity potential ϕ , as follows

$$E_T = \frac{\rho_0 \left(\frac{\partial \phi}{\partial t} \right)^2}{2c^2} + \frac{\rho_0}{2} |\nabla \phi|^2 \quad (3.75)$$

In this case, ϕ is defined as the velocity potential, where it must satisfy $\vec{u} = \nabla \phi$. This new variable shows that the acoustic wave excitation of a fluid does not result in a rotational flow particle velocity. This is only true under the assumptions that rotational viscous effects are very small and confined to the boundaries. That is, forces induced by acoustic pressure changes are assumed significantly larger than those induced from viscous effects. Mathematically, this is shown by equation

$$\nabla \times \vec{u} = \nabla \times \nabla \phi = 0 \quad (3.76)$$

where the curl of the velocity potential gradient field is always equal to zero. Thus, the particle velocity field is irrotational.

In order to obtain equation (3.75), the following general acoustic momentum equation for a fluid element (linear Euler's equation)

$$\rho_0 \frac{\partial \vec{u}}{\partial t} = -\nabla P \quad (3.77)$$

has to be expressed in terms of the velocity potential. That is,

$$\nabla \left(\rho_0 \frac{\partial \phi}{\partial t} + P_{ac} \right) = 0 \quad (3.78)$$

In order to hold equation (3.78) true, the expression in the parenthesis can be selected to vanish. Therefore,

$$P_{ac} = -\rho_0 \frac{\partial \phi}{\partial t} \quad (3.79)$$

If equation (3.79) and the velocity potential definition $\vec{u} = \nabla \phi$ are replaced into (3.74), then equation (3.75) is obtained.

The total energy density and acoustic intensity are related since the second one is defined as the rate of transport of acoustic energy (Lighthill, 1978). According to (Kinsler, 2000), it is the instantaneous rate per unit area of the work done by a single element of the fluid on all other adjacent elements, and it is given by

$$\vec{I} = (P_{ins} - P_{eq}) \vec{u} = P_{ac} \vec{u} = -\rho_0 \left(\frac{\partial \phi}{\partial t} \right) \nabla \phi \quad (3.80)$$

If the total energy density in (3.75) is differentiated about time, its time rate expression becomes

$$\frac{dE_T}{dt} = \rho_0 \left(\frac{\partial \phi}{\partial t} \right) \nabla^2 \phi \quad (3.81)$$

On the other hand, the divergence of the acoustic intensity expressed in terms of the velocity potential is

$$\nabla \cdot \vec{I} = -\rho_0 \left(\frac{\partial \phi}{\partial t} \right) \nabla^2 \phi \quad (3.82)$$

Both cases in (3.81) and (3.82) show the same results with opposed signs. By equating both equations, the conservation of energy along an acoustic ray-tube is defined as

$$\frac{\partial E_T}{\partial t} + \nabla \cdot \vec{I} = 0 \quad (3.83)$$

If the media is time-independent and the total energy density can only have variation in space, then the first term in (3.83) is equal to zero. Furthermore, this also means that there are no sources or sinks of energy flux in space. Thus, the second term in (3.83) must also be equal to zero (Dieminger et al., 1996). Under these conditions, the average flow of energy per cycle of the acoustic waves must be constant along a propagating tube. That is, $|\vec{I}| \times A$ is constant along a ray tube where A corresponds to the cross sectional area of the tube at any arbitrary position in space. Therefore, given an initial ray tube area as well as the corresponding initial intensity, it is possible to compute new intensities for each time step during propagation.

Atmospheric Attenuation

Energy losses during sound propagation through the atmosphere are related to viscous effects, heat conduction, and internal molecular translation processes. These pertain to the classical energy dissipation mechanism. On the other hand, the redistribution of internal energy of molecules pertain to the relaxation mechanisms (Attenborough et al., 2007). Both acoustic attenuation mechanisms are included in the computer implementation of HRT. The formulation used within the code is detailed below.

A wave propagating in a media where all attenuation mechanisms are present, is characterized by the following lossy Helmholtz equation

$$\nabla^2 p + \beta^2 p = 0 \quad (3.84)$$

where, $\beta = k - j\alpha$ is a complex wavenumber and p is the acoustic pressure. The assumed solution to equation (3.84) contains a decaying amplitude as follows

$$p = p_0 e^{-\alpha x} e^{j(\omega t - kx)} \quad (3.85)$$

In this case, P_0 corresponds to the initial acoustic pressure amplitude, and x the distance traveled by the wave. On the other hand, α is the absorption coefficient. If the amplitude changes are tracked between two points traveled by the acoustic wave, then

$$\alpha = -\frac{1}{x} \ln \left(\frac{p}{p_0} \right) \quad (3.86)$$

The units for the absorption coefficient must be in nepers per meter [Np/m] (Kinsler, 2000). The absorption coefficient takes into account energy losses for both classical and relaxation attenuation mechanisms (Attenborough et al., 2007), and it is determined by

$$\alpha = f^2 \left[1.84 \times 10^{-11} \left(\frac{P_{atm}}{P_{atm-ref}} \right)^{-1} \left(\frac{T}{T_0} \right)^{1/2} \right] + \dots \quad (3.87)$$

$$f^2 \left(\frac{T}{T_0} \right)^{-5/2} \left[0.01275 \frac{e^{-2239.1/T}}{f_{r,O} + \frac{f^2}{f_{r,O}}} + 0.1068 \frac{e^{-3352/T}}{f_{r,N} + \frac{f^2}{f_{r,N}}} \right]$$

where, f is the acoustic frequency in Hz, P_{atm} is the local atmospheric pressure, $P_{atm-ref}$ is the reference pressure (1 atm), T is the local temperature, T_0 is the reference atmospheric temperature (293.15 K), $f_{r,O}$ is the relaxation frequency for molecular oxygen, and $f_{r,N}$ is the relaxation frequency for molecular nitrogen. The last two are given by

$$f_{r,O} = \left(\frac{P_{atm}}{P_{atm-ref}} \right) \left[24 + 4.04 \times 10^4 h (0.02 + h) \times (0.391 + h)^{-1} \right] \quad (3.88)$$

and

$$f_{r,N} = \left(\frac{P_{atm}}{P_{atm-ref}} \right) \left(\frac{T_0}{T} \right)^{1/2} \left(9 + 280he^{-4.17 \left[\left(\frac{T_0}{T} \right)^{1/3} - 1 \right]} \right) \quad (3.89)$$

For both equations, (3.88) and (3.89), h corresponds to the molar concentration of water vapor in percentage and it is determined as follows

$$h = h_r \left(\frac{P_{sat}}{P_{atm}} \right) \quad (3.90)$$

where, h_r is the local relative humidity and P_{sat} is the saturated vapor pressure given by

$$\begin{aligned} \log_{10} \left(\frac{P_{sat}}{P_{atm}} \right) &= 10.79586 \left[1 - \left(\frac{T_{01}}{T} \right) \right] - 5.02808 \log_{10} \left(\frac{T}{T_{01}} \right) + \dots \\ &1.50474 \times 10^{-4} \times \left(1 - 10^{-8.29692 \left[\frac{T}{T_{01}} - 1 \right]} \right) - 4.2873 \times \dots \\ &10^{-4} \times \left(1 - 10^{-4.276955 \left[\frac{T_{01}}{T} - 1 \right]} \right) - 2.2195983 \end{aligned} \quad (3.91)$$

In this case T_{01} must be equal to 273.16 K and corresponds to the triple-point isotherm temperature.

Figure 3.6 shows the variation of the absorption coefficient on equation (3.87) as a function of frequency per pressure. Curves for various relative humidity at a temperature of 20 degrees Celsius are observed. Variation of the attenuation coefficient with frequency becomes more prominent as relative humidity increases. In addition, attenuation effects are more important as frequency becomes larger (Bass, 1995).

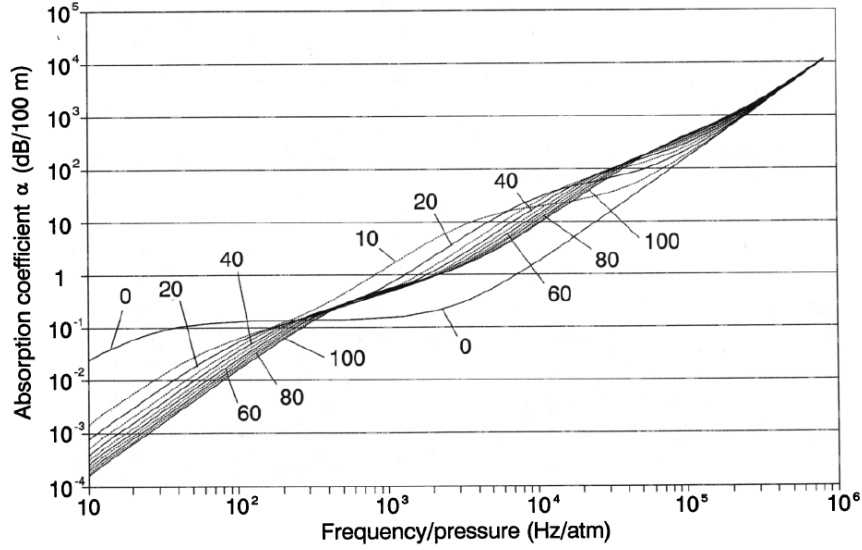


Figure 3.6: Absorption Coefficient [dB/100 m] in terms of frequency/pressure ratio [Hz/atm] for various relative humidity values at 20 degrees Celsius (Bass, 1995).

The formulation presented above is used as part of the HRT computer implementation. It is a widely accepted method for atmospheric sound attenuation and implemented by the standard ANSI/AS S1.26-2014 (ANSI, 2014) and with a slight variation on ISO 9613-1 (ISO, 1993). For the second one, the following expression for calculating P_{sat} is used instead

$$\log_{10} \left(\frac{P_{sat}}{P_{atm}} \right) = -6.8346 \left(\frac{T_{01}}{T} \right)^{1.261} + 4.6151 \quad (3.92)$$

Even though modifications to equation (3.87) have been developed (e.g. by including relaxation frequency for CO_2), this model is still accurate below altitudes of 60 km (Sutherland, 2004).

The HRT computer implementation computes the sound pressure levels during propagation between consecutive ray tube locations in space. In order to take into account attenuation, the traveled distance between these consecutive locations is required. In addition, the attenuation coefficient from equation (3.85) must also be calculated. Figure 3.7 shows a diagram of a ray tube with initial acoustic pressure amplitude P_0 . This ray-tube is then propagated to a new location after

traveling a distance d . The acoustic pressure amplitude at the new location is then $P_0 e^{-\alpha d}$, as specified by equation (3.85).

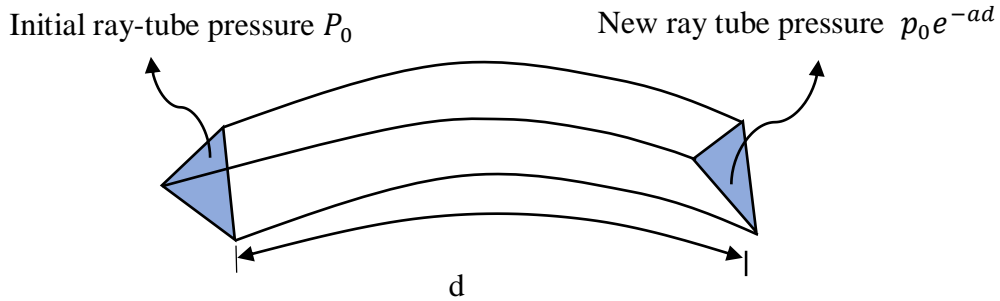


Figure 3.7: Attenuation effects on ray tube pressure amplitude between consecutive steps during propagation.

The sound pressure level reduction between the consecutive ray tube locations shown in Figure 3.7 is then given by

$$\Delta L_{dB-atm} = 10 \log_{10} \left(\frac{P_0 / \sqrt{2}}{P_0 e^{-\alpha d} / \sqrt{2}} \right)^2 = d \times 10 \log_{10} e^{2\alpha} \quad (3.93)$$

Therefore, the developed HRT is capable of taking into account atmospheric attenuation during propagation simulations. In addition to the atmospheric temperature and wind distributions, it also requires a relative humidity distribution over the propagating media.

Ground Attenuation and Ray Reflections

Characterization of ground properties is very important for the calculation of excess attenuation at the receiver's location. Most outdoor ground surfaces are usually classified according to their porosity. For example, the standard ISO-9613-1 considers any surface of low porosity to be acoustically hard, while grass, trees and other vegetation are acoustically soft. This classification oversimplifies a wide range of properties that should be considered. To account for changes in phase and energy dissipation of the reflected component of a wave, flow resistivity is required which is the most important parameter. It corresponds to the ratio of applied pressure gradient to the amount of the induced volume flow rate per unit thickness of the ground material. A material

with high flow resistivity translates to low porosity. Embleton et al. (1983) reported measured flow resistivity for different ground surfaces.

For outdoor sound propagation applications, the characteristic acoustic ground impedance is most commonly a function of both frequency and flow resistivity. The HRT computer implementation uses a widely accepted semi-empirical ground impedance model developed by Delany et al. (1970). An expression for the ground impedance normalized to the characteristic air impedance ρc is given as

$$Z_G = 1 + 9.08 \left(\frac{f}{\sigma} \right)^{-0.75} + 11.9j \left(\frac{f}{\sigma} \right)^{0.73} \quad (3.94)$$

where f is frequency in [Hz] and σ is the flow resistivity in CGS units. This equation was obtained by fitting curves to measurements on different types of materials with an impedance tube. The curves given by (3.94) may be used with confidence over a range of $10 \leq f/\sigma \leq 1000$. However, at low frequencies the results may not be as accurate, especially for materials with very high porosity. This is because some materials are not structurally rigid over low ranges of f/σ .

The Delany-Bazley method is also used in other commercial software such as Harmonoise (E. Salomons et al., 2011), and Nord 2000 (Plovsig, 2006b). In addition, the standards ANSI/ASA S1.18-2010 and NORDTEST ACOU 104 have adopted this method for ground impedance computation. Furthermore, atmospheric noise propagation models based on geometrical approaches such as the one developed by L'Espérance et al. (1992) also use it.

Despite the success of the Delany-Bazley model for impedance predictions, the model is still not physically precise. Energy conservation is violated in the model, causing unrealistic results for specific cases (Gunnar Taraldsen et al., 2011). More accurate impedance models have also been developed in order to improve accuracy of the Delany-Bazley method. Techniques such as those introduced by Miki (1990) and Komatsu (2008) have been developed with the intention of improving its accuracy. According to Attenborough et al. (2011), the Delany-Bazley method is accurate for grass-covered surfaces. However, it fails to predict impedance of softer surfaces such

as forest floor, porous asphalt or gravel. For these cases, alternative models should be used. Table 3.2 summarizes the most relevant impedance models with improved accuracy. Their input parameters have also been listed.

Table 3.2: Ground impedance model alternatives to the Delany-Bazley model.

Model	Input Parameters
Delany et al. (1970)	Effective Flow Resistivity
G. Taraldsen (2005)	Effective Flow Resistivity
Bérenghier et al. (1997)	Porosity, Flow Resistivity, Structure Factor
Attenborough (1987)	Porosity, Flow Resistivity, Tortuosity, Pore Shape Factor
Wilson (1997)	Viscous and Thermal Relaxation Times for Low and High Frequencies

In order to account for ray reflections in the HRT model, the angle β between a line normal to the ground surface and the incident ray tube has to be computed. This is shown in Figure 3.8 (L'Espérance et al., 1992).

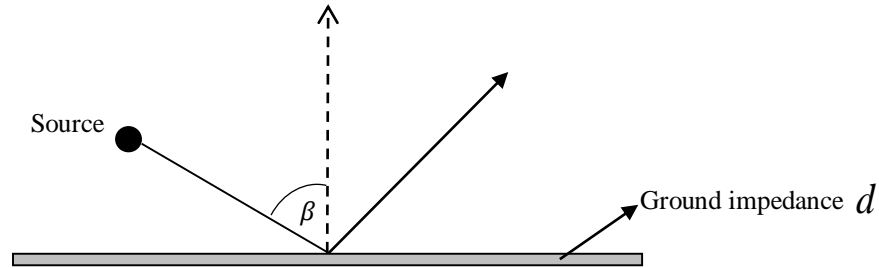


Figure 3.8: Ray reflection scheme over ground with impedance Z_G .

Given the geometry in Figure 3.8, a reflection coefficient is established using the normalized ground impedance as follows

$$R_p = \frac{\cos \beta - Z_G}{\cos \beta + Z_G} \quad (3.95)$$

The sound pressure level reduction due to ground reflection of the ray tubes is then given by

$$\Delta L_{dB-G} = 10 \log_{10} (R_p^2) \quad (3.96)$$

This procedure is followed for all ray tubes that reflect on the ground during the HRT propagation.

3.3. METHOD VALIDATION

This section presents a number of validation and example cases for the HRT propagation method. A ray path validation compared to analytical solutions is initially presented. Sound pressure levels over ground noise maps are then compared with FFP and Eikonal results for the same noise source.

Ray Path Validation

Current analytical solutions for outdoor sound propagation are very limited. However, Qi Mo et al. (2015) developed analytical expressions for the Eikonal ray path (see equation (2.72)). It computes refracted ray paths in 2D planes defined parallel to a defined initial propagation direction. This analytical solution is limited to the case of stationary media (negligible wind) and a linear speed of sound profile. The Hamiltonian ray path numerical solutions have been validated against this analytical approach.

Figure 3.9 shows three rays propagated from a noise source located at 100 meters height in a stationary media where the 2D speed of sound profile is $c(z) = 332 + 0.6z$ from left to right in the figure. The three rays were emitted using different elevation angles (angle between x-axis and direction of emission of the rays) of 15, 45, and 75 degrees. In addition, a maximum height of 300 meters and a distance in the x-axis of 150 meters were selected in order to show refractive effects along the ray paths. The HRT results were obtained using the equations in (3.57) for 2D and a 4th order Runge-Kutta numerical integration method. Results show that the HRT technique produces ray paths that are very close to those analytically computed. Given that the Hamiltonian ray tracing is solved numerically, errors increase for larger propagation distances as expected. However, these are not significant. It is also observed that for shallow elevation angles the results show higher errors than for wide elevation angles. Provided the results in Figure 3.9, it can be concluded that the numerical scheme using the HRT method provides sufficiently accurate ray path solutions.

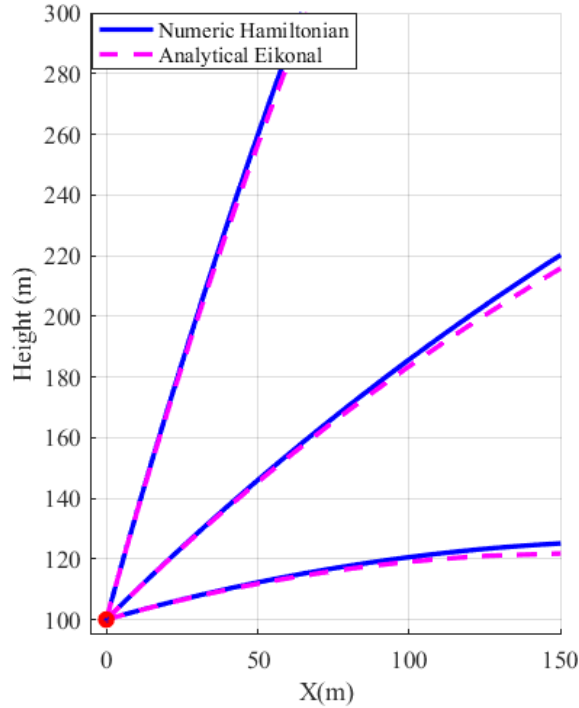


Figure 3.9: Three rays propagated from a noise source located at 100 meter height using the numerical HRT technique and Analytical Eikonal approach.

Sound Pressure Levels Validation

The next validation case compares the Hamiltonian Ray Tracing (HRT) method against a Fast Field Program (FFP) and Eikonal Ray Tracing (ERT) outputs. The FFP implemented for validation is based on a NASA code developed for prediction of noise from fixed wing aircrafts and helicopters (Burley et al., 2014). FFP numerically solves a Helmholtz equation transformed to the horizontal wavenumber domain. It does so over a stratified media where the wavenumber depends exclusively on height (E. M. Salomons, 2001). This is one of the major limitations of this code, in addition to the vast amount of computational time required for simulations. Nevertheless, this method is widely accepted for atmospheric noise prediction purposes.

On the other hand, the selected ERT technique was programmed in Matlab using the formulation in section 2.1. The magnitude-form Eikonal equation (2.51) was implemented by following the wavefront approach solution described in Appendix C. Finally, the ERT and HRT were solved under the same conditions. That is, the same numerical solution method (Runge-Kutta numerical

integration), coding language (Matlab), and simulation parameters (including the same source power levels, wind velocity and direction, atmospheric temperature changes, relative humidity and ground flow resistivity).

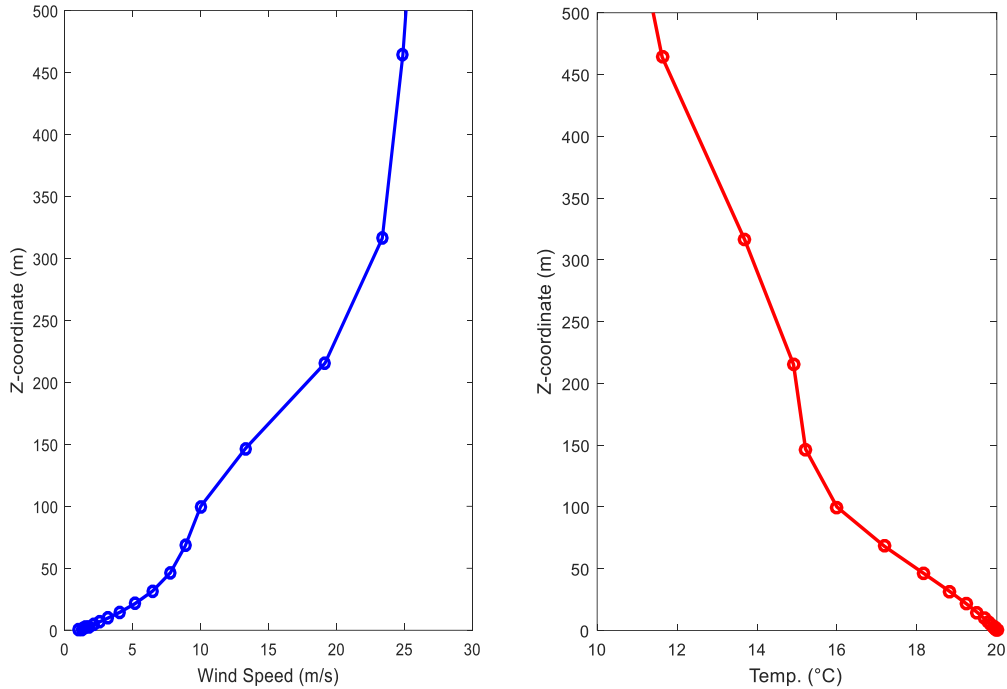


Figure 3.10: Wind and temperature profile used in the simulations.

The selected validation problem consists of a monopole source located at 100 m height. The selected source’s sound power is of 100 [dB] per 1/3rd octave band within 10-10,000 Hz. The weather conditions consist of the non-uniform wind and temperature profiles shown in Figure 3.10. They were generated by modifying experimentally measured data (Slawsky et al., 2015). There is no vertical wind component in the simulations. The terrain was assumed flat and acoustically hard, e.g. very high flow resistivity. The used HRT and ERT codes emitted 2,562 rays from the monopole source using a 4th order Runge-Kutta (RK) integration and a time step of 0.025 [s]. The noise maps consist of a 2 Km square grid that contains 441 points every 50 meters, all located on the ground surface. The monopole is located at the center of the grid for all simulation cases.

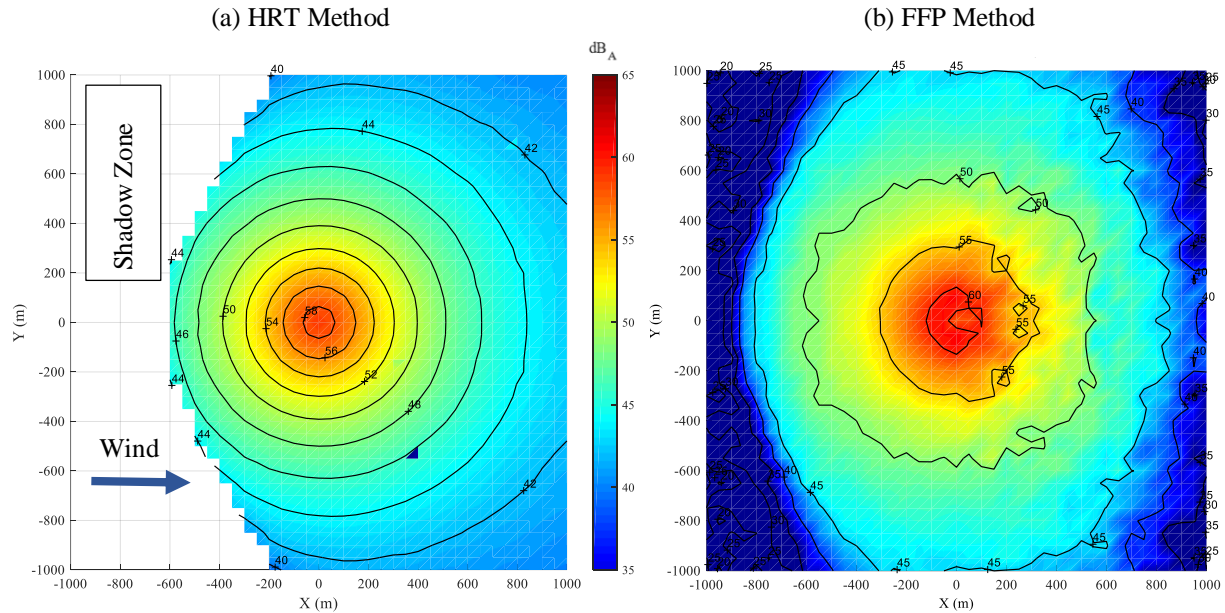


Figure 3.11: Monopole source OASPL noise maps for (a) HRT (4th order RK and $\Delta t = 0.025$ s.) and (b) FFP numerical solutions.

Figure 3.11 shows two simulated monopole overall A-weighted noise levels maps for both the HRT and FFP methods. Both were computationally processed under identical conditions. Smooth lines with decreasing noise levels surrounding the source characterize the HRT results. The FFP map on the other hand shows significant noise level fluctuations around the noise source. However, unlike any ray tracing methods such as the HRT and the ERT techniques, FFP is capable of computing noise over shadow zones. Noise for both HRT and FFP noise levels at different locations on the noise maps are shown in Table 3.3. Sound pressure levels show good agreement between the methods. Yet, computational time for the FFP method was of 3.6 hours using a Fortran code, while the HRT method took only 6 minutes in Matlab. All simulations were performed on a 3.42-GHz quad-core personal computer with 16 GB of RAM.

Table 3.3: Sound Pressure Level results over noise map grid for HRT, FFP and ERT methods.

Noise Map Coordinates (x,y,z)	Sound Pressure Levels [dBA]		
	HRT(4 th Order RK)	FFP	ERT(4 th Order RK)
(800,0,0)	43.8	44.9	40.9
(600,800,0)	41.9	44.4	38.8
(-450,0,0)	48.3	52.0	44.7

Table 3.3 also shows the results for the ERT numerical solution of the same validation case. The sound pressure levels for the ERT show good agreement with the HRT and FFP, with a slight under prediction at the selected ground-level points. Its output noise map is shown in Figure 3.12. It is observed that the Eikonal approach produces inaccurate sound pressure level fluctuations, modifying the characteristic monopole noise pattern around the source. This is not the case for the HRT in Figure 3.11a. The ERT computational time for the shown emission of 2,562 rays using a 4th order RK and $\Delta t = 0.025$ [s] (same conditions as the HRT case presented above) is of 6 minutes. That is, approximately the same computational time used by the HRT.

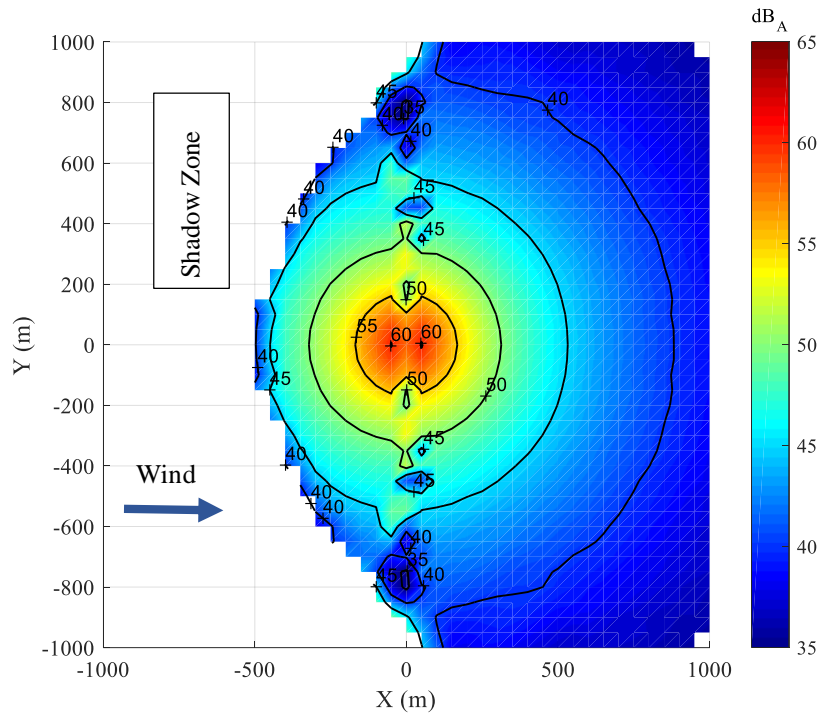


Figure 3.12: Monopole source OASPL noise maps for Eikonal 4th order Runge-Kutta and time step of 0.025 [s].

Figure 3.13 shows ERT results for a 2nd order RK and a step size of 0.025 [s] for integration, while a more realistic monopole directivity pattern is obtained when a higher order RK is implemented with a smaller time step size, as shown in Figure 3.12b (4th order RK and step size of 0.001 [s]). It can be concluded that the ERT unrealistic fluctuations are due to numerical errors. Therefore, higher order integration methods will provide more accurate results. The ERT requires higher order integration methods to reach the same level of accuracy as the HRT. Further investigation on the ERT technique can provide more insight on its limitations and improve its computational efficiency to match that of the HRT approach.

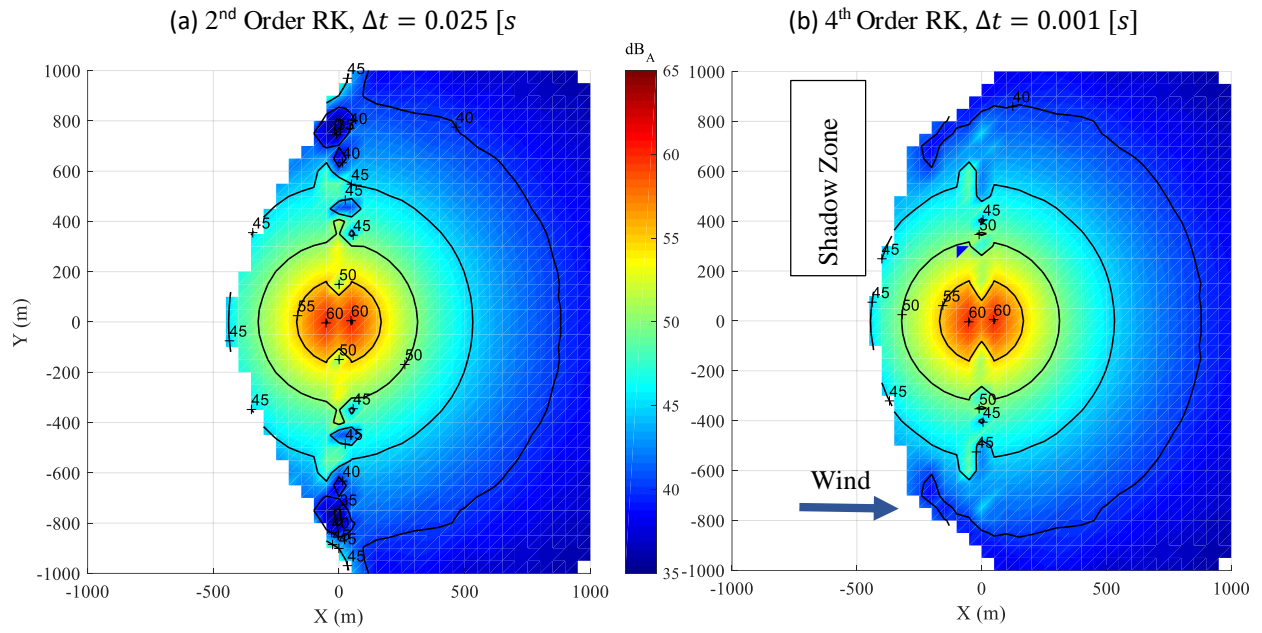


Figure 3.13: Monopole source OASPL noise maps for (a) Eikonal 2nd order Runge-Kutta and time step of 0.025 [s] and (b) Eikonal 4th order Runge-Kutta and time step of 0.001 [s].

4. WTNoise MODELING TOOL

In this chapter, the structure of the developed WTNoise modeling tool is addressed. In addition, its theoretical framework is defined. This includes aerodynamics, acoustic noise sources, and aeroelasticity. Furthermore, a description on the procedure used to couple the HRT computer implementation into WTNoise is provided. Finally, wind turbine noise simulation results are presented propagated over a 2Km ground grid.

4.1. CODE STRUCTURE

WTNoise is modeling tool developed in Matlab. It consists of five modules (see Figure 4.1).

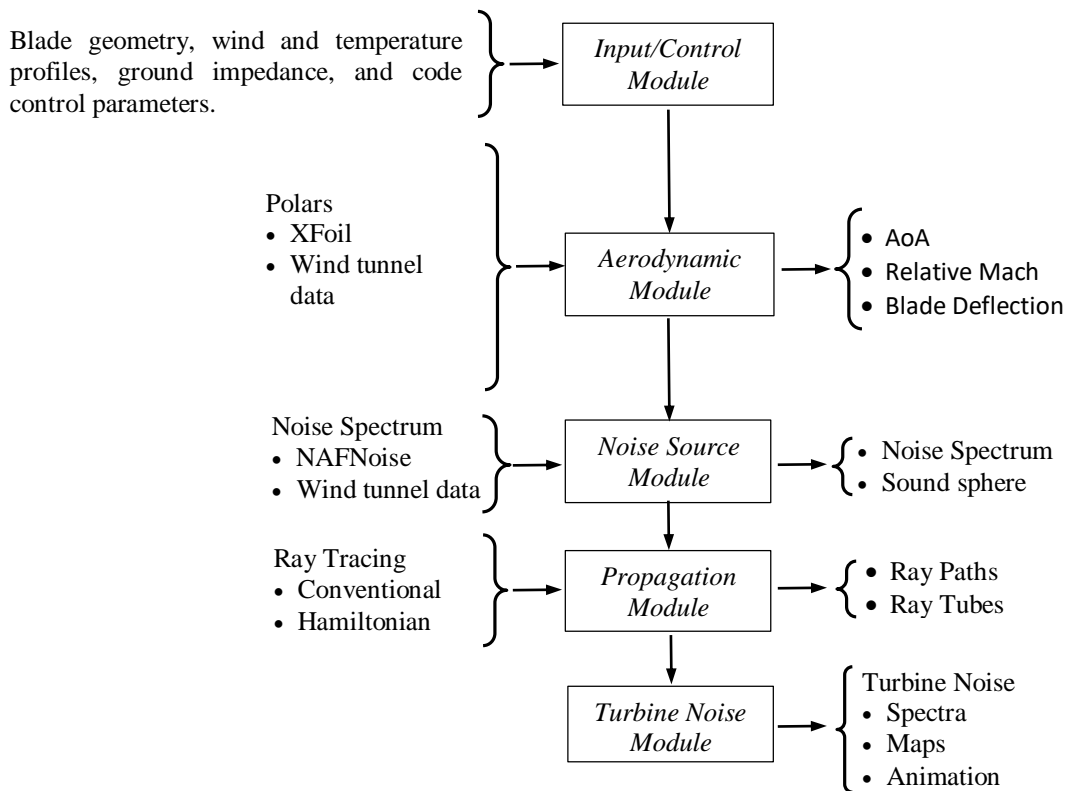


Figure 4.1: Wind Turbine Noise (WTNoise) modelling tool modules.

The inputs to WTNoise are turbine hub height, blade geometry and construction parameters. In addition, operating conditions, atmospheric and ground properties, and execution control parameters are required. The terrain has no irregularities (flat terrain assumption) and atmospheric conditions are arbitrary with height. The blades are split in the span-wise direction in several

elements and the rotation of the blade is approximated with discrete azimuth angles. Thus, aerodynamic calculations can be discretely performed during operation. These are defined in Figure 4.2a. Aerodynamic sound sources characterizing the turbine's radiation are defined at these locations.

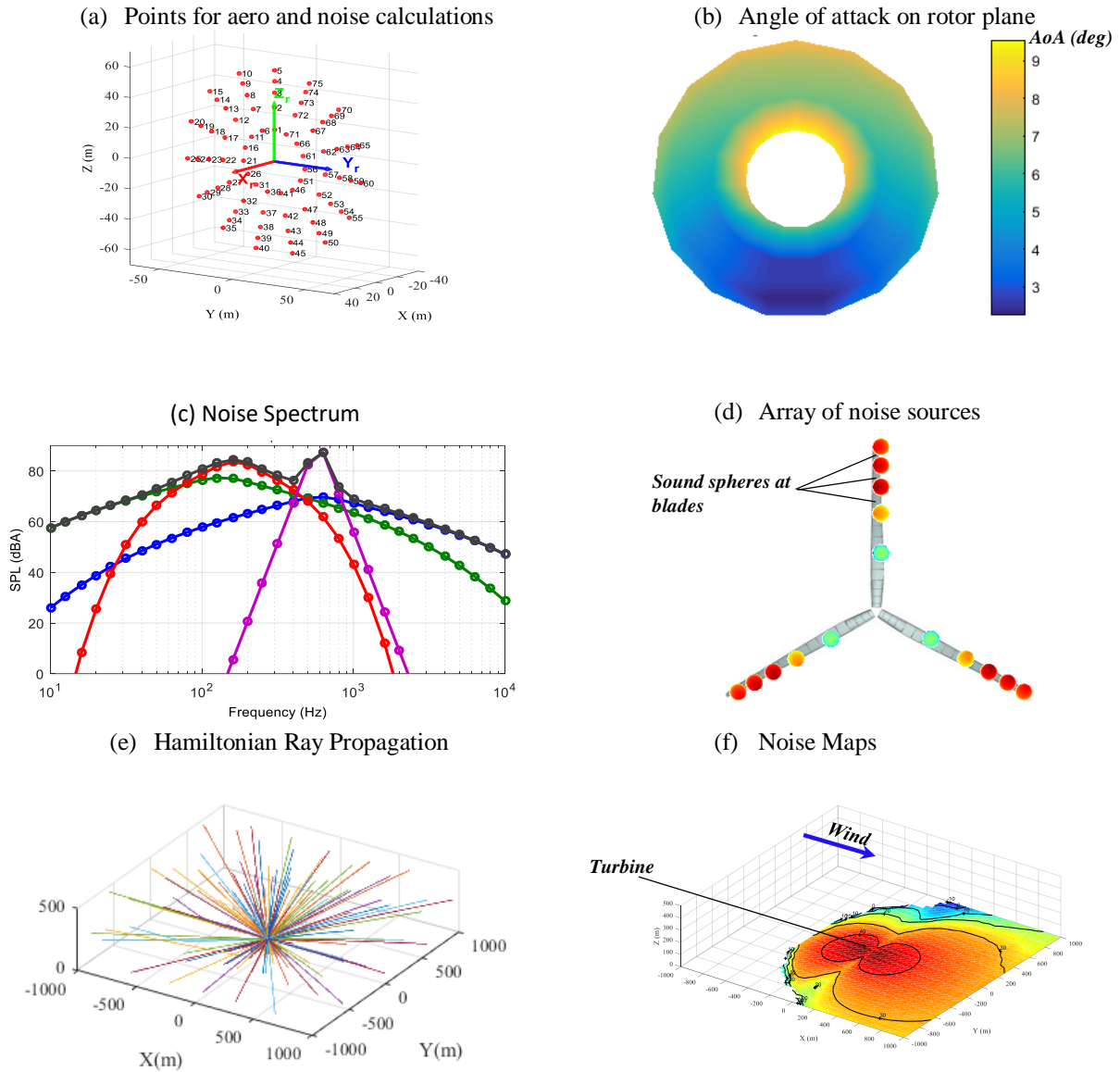


Figure 4.2: (a) Points on rotor plane for aerodynamic and noise calculation, (b) AoA for full rotation in a non-uniform flow, (c) noise source 4 spectrum computed by NAFNoise, (d) sound spheres array for the wind turbine blades, (e) Hamiltonian ray propagation (f) resulting OASPL noise map due to turbine at 48° azimuth position.

The second module is the *Aerodynamic Module*. It implements the blade element momentum method (BEM) to compute the aerodynamic parameters needed for noise calculations. These are, angles-of-attack (AoA) and relative flow Mach numbers (Sanderse, 2009). This process is followed for every element along the blade. To this end, the airfoil section polars (lift and drag coefficients as a function of angle of attack) are either computed using XFOil (Drela et al., 2001) or taken from data collected in a wind tunnel (Deavenport et al., 2010). Turbine yaw, tilt, and cone angles (see Figure 4.3) are accounted for the calculation of the AoAs. Figure 4.2b illustrates the resulting AoAs for all azimuth positions in the presence of a particular wind profile.

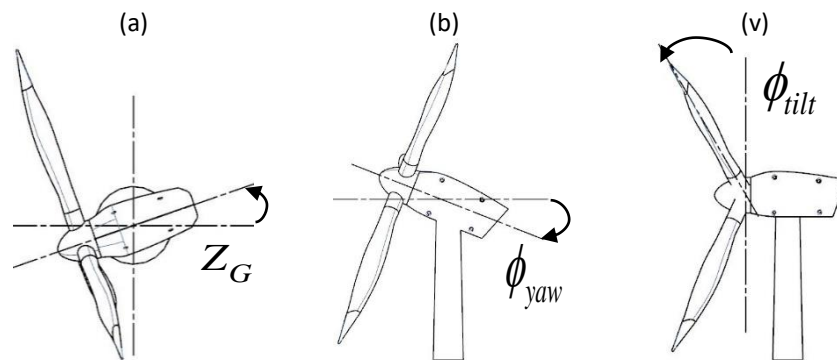


Figure 4.3: (a) Turbine top view showing yaw angle, (b) Turbine side view showing tilt angle, (c) Turbine side view showing blade cone angle (Wu, 2017).

The flow behavior over the blades of a wind turbine govern its aerodynamic noise generation mechanisms. In the *Noise Source Module*, the aerodynamic noise sources (leading and trailing edge noise) are computed for the selected blade elements and the set of azimuth blade positions. This module implements the code NAFNoise (P. Moriarty et al., 2003) or wind tunnel data (Migliore et al., 2004) to predict the aerodynamic noise in 1/3rd octave bands at a single point in the direction normal to the airfoil chord line at a distance of 1 meter. Then, the radiation directivity of the sources proposed by Brooks et al. (1989) are applied to construct sound spheres around the blade elements. An example of the resulting noise spectrum for different sound sources is shown in Figure 4.2c and the constructed sound spheres for all airfoil elements are shown in Figure 4.2d.

Next is the *Propagation Module* that implements a Hamiltonian ray tracing propagation of the individual sound spheres along the blade. This module uses the wind and temperature profiles and other atmospheric conditions (humidity, pressure, etc.) to predict the noise at an array of

microphones in the domain, typically over a plane parallel to the ground. To this end, a large number of rays are emitted from the sound sources (see Figure 4.2e). The acoustic losses, due to atmospheric attenuation and ground reflections, as well as Doppler effects caused by wind velocity are accounted for in this module.

The final module, *Turbine Noise*, concatenates the noise at the microphones produced by all the blade element sound sources and rotor azimuth positions for all 1/3rd octave frequency bands. Figure 4.2f shows a typical noise map for a specific azimuth position.

4.2. COORDINATE SYSTEMS AND ROTATION MATRICES

Defining the coordinate systems used by WTNoise is important to define its dynamic behavior. The main coordinate systems are the following: global, rotor, airfoil, and directivity (see Figure 4.4). The global coordinate system (x_g, y_g, z_g) is defined at the tower center on ground with z-axis pointing upward, x-axis pointing downwind, and y-axis perpendicular to them as shown in Figure 4.4a). The rotor coordinate system (x_r, y_r, z_r) is centered at the center of the rotor plane and rotates with the rotor during simulations.

In WTNoise, airfoil and directivity coordinate systems are needed to orient the aerodynamic noise spheres relative to the blade. The airfoil coordinate system (x_a, y_a, z_a) is shown in Figure 4.4b. The origin is located at the center of the blade element on the intersection of the blade pitch axis and the local airfoil chord (the z_a -axis points outwards of the page). The radiation directivity implemented with NAFNoise of the noise sources for trailing and leading edge are defined with respect to the coordinate system (x_d, y_d, z_d) as shown in Figure 4.4c. For illustration purposes, Figure 4.4d shows the baffled dipole directivity in terms of the directivity coordinates.

The above coordinate systems allow accounting for yaw, tilt, cone, azimuth, twist, and pitch angles. For sound propagation (propagation module), the directivity of the noise sources has to be expressed in the global coordinate system. To this end, a number of rotation matrices that links the four coordinate systems must be defined.

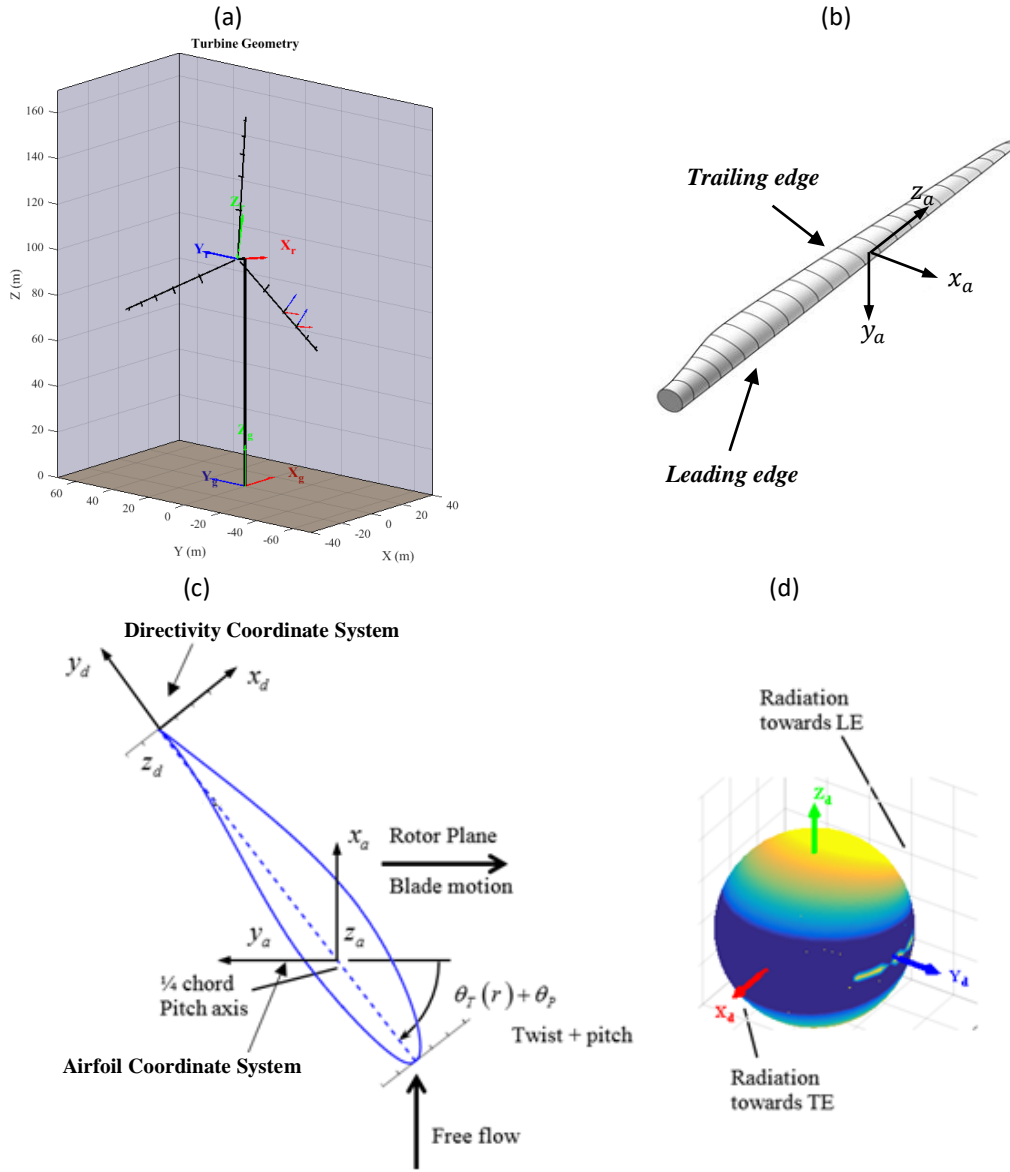


Figure 4.4: WTNoise coordinate systems: (a) global and rotor coordinate systems, (b) airfoil coordinate system (c) directivity coordinate system on the airfoil element, (d) A baffled dipole sound spheres relative to the directivity coordinate system (Wu, 2017).

Rotor to Global Rotation

To account for the rotor yaw and tilt, the global and rotor coordinate systems are related by two rotation matrices, as follows

$$\begin{Bmatrix} x_g \\ y_g \\ z_g \end{Bmatrix} = \begin{bmatrix} \cos(\phi_{yaw}) & -\sin(\phi_{yaw}) & 0 \\ \sin(\phi_{yaw}) & \cos(\phi_{yaw}) & 0 \\ 0 & 0 & 1 \end{bmatrix} \begin{Bmatrix} x_r \\ y_r \\ z_r \end{Bmatrix} = [R_{gr}^{yaw}] \begin{Bmatrix} x_r \\ y_r \\ z_r \end{Bmatrix} \quad (4.1)$$

$$\begin{Bmatrix} x_g \\ y_g \\ z_g \end{Bmatrix} = \begin{bmatrix} \cos(\phi_{ilt}) & 0 & \sin(\phi_{ilt}) \\ 0 & 1 & 0 \\ -\sin(\phi_{ilt}) & 0 & \cos(\phi_{ilt}) \end{bmatrix} \begin{Bmatrix} x_r \\ y_r \\ z_r \end{Bmatrix} = [R_{gr}^{ilt}] \begin{Bmatrix} x_r \\ y_r \\ z_r \end{Bmatrix} \quad (4.2)$$

where ϕ_{yaw} and ϕ_{ilt} are the yaw and tilt angles. The transformation from rotor to global is then

$$\begin{Bmatrix} x_g \\ y_g \\ z_g \end{Bmatrix} = [R_{gr}^{yaw}] [R_{gr}^{ilt}] \begin{Bmatrix} x_r \\ y_r \\ z_r \end{Bmatrix} \quad (4.3)$$

Airfoil to Rotor Rotation

The rotor and airfoil coordinate systems are related to each other by the rotor cone and the blade azimuth angle. The rotation of the airfoil coordinate system due to coning is the following

$$\begin{Bmatrix} x_r \\ y_r \\ z_r \end{Bmatrix} = \begin{bmatrix} \cos(\phi_{cone}) & 0 & -\sin(\phi_{cone}) \\ 0 & 1 & 0 \\ \sin(\phi_{cone}) & 0 & \cos(\phi_{cone}) \end{bmatrix} \begin{Bmatrix} x_a \\ y_a \\ z_a \end{Bmatrix} = [R_{ra}^{cone}] \begin{Bmatrix} x_a \\ y_a \\ z_a \end{Bmatrix} \quad (4.4)$$

The rotation matrix that accounts for the azimuth angle is

$$\begin{Bmatrix} x_r \\ y_r \\ z_r \end{Bmatrix} = \begin{bmatrix} 1 & 0 & 0 \\ 0 & \cos(\phi_{azimuth}) & -\sin(\phi_{azimuth}) \\ 0 & \sin(\phi_{azimuth}) & \cos(\phi_{azimuth}) \end{bmatrix} \begin{Bmatrix} x_a \\ y_a \\ z_a \end{Bmatrix} = [R_{ra}^{azimuth}] \begin{Bmatrix} x_a \\ y_a \\ z_a \end{Bmatrix} \quad (4.5)$$

Thus, the rotation matrix between the rotor and airfoil coordinate systems is

$$\begin{Bmatrix} x_r \\ y_r \\ z_r \end{Bmatrix} = [R_{ra}^{azimuth}] [R_{ra}^{cone}] \begin{Bmatrix} x_a \\ y_a \\ z_a \end{Bmatrix} \quad (4.6)$$

Directivity to Airfoil Rotation

The airfoil and directivity coordinate systems are related by the angle $\tau(r)$. This angle takes into account the local blade twist (varies at different radial locations along the blade) given by $\theta_T(r)$

and the blade pitch θ_p . Thus, $\tau(r) = \theta_T(r) + \theta_p$, defines the following rotation between both coordinate systems

$$\begin{Bmatrix} x_a \\ y_a \\ z_a \end{Bmatrix} = \begin{bmatrix} \cos(\tau(r)) & \sin(\tau(r)) & 0 \\ -\sin(\tau(r)) & \cos(\tau(r)) & 0 \\ 0 & 0 & 1 \end{bmatrix} \begin{Bmatrix} x_d \\ y_d \\ z_d \end{Bmatrix} = [R_{ad}^{pitch+twist}(r)] \begin{Bmatrix} x_d \\ y_d \\ z_d \end{Bmatrix} \quad (4.7)$$

Directivity to Global Rotation

The final transform from directivity to a global coordinate system is defines as follows

$$\begin{Bmatrix} x_g \\ y_g \\ z_g \end{Bmatrix} = [R_{gr}^{yaw}] [R_{gr}^{tilt}] [R_{ra}^{azimuth}] [R_{ra}^{cone}] [R_{ad}^{pitch+twist}(r)] \begin{Bmatrix} x_d \\ y_d \\ z_d \end{Bmatrix} \quad (4.8)$$

4.3. BLADE DEFLECTION

In order to account for blade deflection, WTNoise implements either a stand-alone *AeroDyn v15* (P. Moriarty, 2004) or *FAST v8*. *AeroDyn v15* performs the aerodynamical computations by using a modified BEM algorithm developed by Ning (2014). This altered BEM method is computationally less intensive and guarantees convergence. On the other hand, *FAST v8* is a driver code that couples various modules to simulate aerodynamic and dynamic responses of a wind turbine. One of its modules is *AerDyn*. However, its aerodynamic calculations are coupled to other modules that account for structural blade deflection. The aeroelasticity implementation in WTNoise was developed by Wu (2017).

Blade deflection can be taken into account for both translational and rotational displacements. These displacements affect turbine noise predictions by altering the directivity coordinates, where the sound spheres are constructed. Translational displacements are defined with respect to the x, y, and z-axis of the blade coordinates (see Figure 4.5a). WTNoise only takes into account displacement in the blade's x-axis coordinates because this is the dominant one. Displacements in

the y and z directions can be neglected. An example of the translational displacement of a blade for a NREL 5MW wind turbine (J. M. Jonkman et al., 2009) is shown in Figure 4.5b.

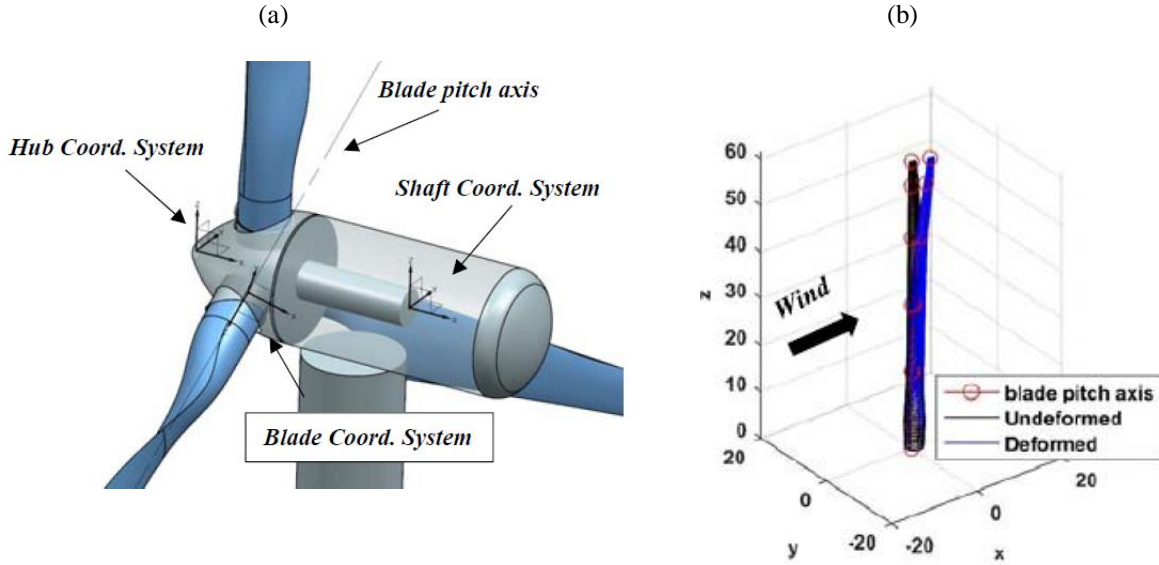


Figure 4.5: (a) Hub, blade and shaft coordinate systems for a wind turbine, (b) Blade deflection results for a NREL 5 MW wind turbine (Wu, 2017).

On the other hand, WTNoise takes into account rotational displacements due to deflection in form of changes to the cone and twist blade angles. These angular changes are defined as $\theta(r)$ and $\Psi(r)$, respectively. Thus, if deflection is taken into account, $[R_{ad}^{pitch+twist}(r)]$ and $[R_{ra}^{cone}]$ change to

$$[\hat{R}_{ad}^{pitch+twist}(r)] = \begin{bmatrix} \cos(\hat{\tau}(r)) & \sin(\hat{\tau}(r)) & 0 \\ -\sin(\hat{\tau}(r)) & \cos(\hat{\tau}(r)) & 0 \\ 0 & 0 & 1 \end{bmatrix} \quad (4.9)$$

Where, $\hat{\tau}(r) = \theta_T(r) + \theta_p + \theta(r)$. Also,

$$[\hat{R}_{ra}^{cone}(r)] = \begin{bmatrix} \cos(\phi_{cone} + \psi(r)) & 0 & -\sin(\phi_{cone} + \psi(r)) \\ 0 & 1 & 0 \\ \sin(\phi_{cone} + \psi(r)) & 0 & \cos(\phi_{cone} + \psi(r)) \end{bmatrix} \quad (4.10)$$

Therefore, the new coordinate transformation from directivity to global coordinates is

$$\begin{Bmatrix} x_g \\ y_g \\ z_g \end{Bmatrix} = \begin{bmatrix} R_{gr}^{yaw} \\ R_{gr}^{tilt} \\ R_{ra}^{azimuth} \\ \hat{R}_{ra}^{cone}(r) \\ \hat{R}_{ad}^{pitch+twist}(r) \end{bmatrix} \begin{Bmatrix} x_d \\ y_d \\ z_d \end{Bmatrix} \quad (4.11)$$

4.4. WTN PROPAGATION

Ray propagation from the noise spheres shown in Figure 4.2d has to be performed. The objective is to compute the overall wind turbine noise over the ground surface. Each sphere contains sound pressure level data from all aerodynamic noise sources (located at leading and trailing edges). Furthermore, every point on the sound spheres is expressed in the global coordinate system, after implementing equation (4.11). As addressed in section 3.2, intensity and area of the ray tubes has to be tracked during propagation. In addition, ground reflections and the process to build noise maps over the ground is explained in this section. The HRT computer implementation into WTNoise is done via a script named HRay inside the *Propagation Module*.

Wind Turbine Acoustic Field

The HRT computer implementation in WTNoise requires a starting aerodynamic noise field. The wind turbine sound spheres in Figure 4.2d along the blades are constructed as icosahedrons composed of an evenly distributed spherical grid. As shown in Figure 4.6, every point over the grid contains Sound Pressure Level (SPL) data. Additionally, an initial wavenumber vector is assigned to all grid points i.e. vectors normal to the spherical surface with magnitude equal to ω_r/c . Finally, rays are propagated from all grid points by using the HRT equations in (3.57).

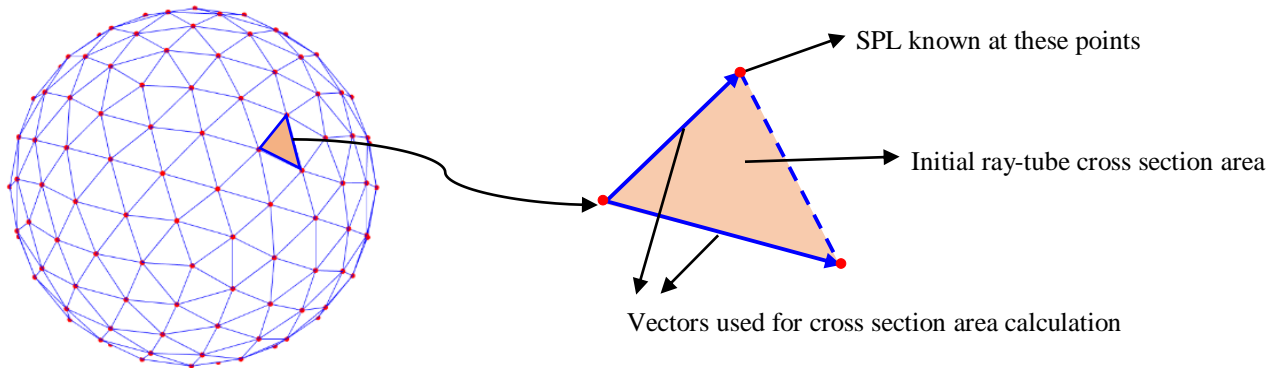


Figure 4.6: Ray tube triangular cross section area and vectors used for cross product.

A set of triangular areas over the grid are selected. The rays bounded by the initial triangles conform single ray tubes propagated through space. The initial intensity associated to each bundle of rays is then calculated by averaging the SPL for all points in the triangle and dividing the result by ρc . The ray tube areas are also computed by performing a cross product between the two vectors that form the triangular cross sections (see Figure 4.6). The magnitude of the cross product divided by two results in the tube areas. These areas are constantly changing during propagation because adverse atmospheric conditions alter the path of the rays, as shown in Figure 4.7.

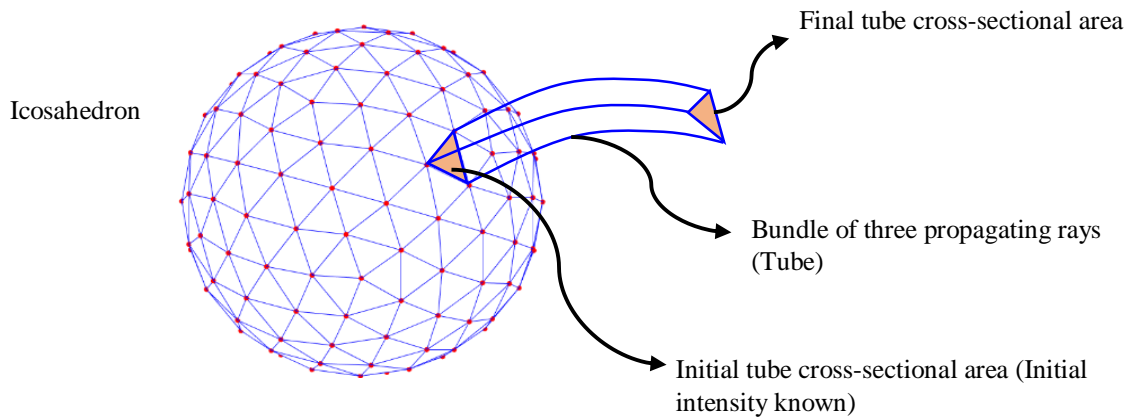


Figure 4.7: Ray tube propagation from spherical source grid.

For every propagation time-step, a new area and intensity are calculated as follows

$$I_n = \frac{I_{n-1} \times A_{n-1}}{A_n} \quad (4.12)$$

Where, I and A correspond to the ray tube intensity and area respectively and n corresponds to the time step subscript. Thus, the source's generated SPLs can be computed in space for any specified simulation time during atmospheric propagation.

Ground Reflections

The current version of WTNoise takes into account a single ground reflection. In order to account for this, a novel modeling approach is implemented as follows. First, an altitude threshold above the ground is initially defined. This is used to identify the rays that are approaching the ground. Between this altitude threshold and ground level, the wavenumber's component in the z-direction

is always negative if a ray is heading towards the ground. Using the ray path equations in (3.57), the last computed point right before reflection is identified. A straight ray is then propagated towards the ground with a constant wavenumber. Once the assumed linear paths touch the ground, their wavenumber z -components automatically change sign and the HRT equations restart the curved propagation away from the ground.

Ray tube reflections also have to be taken into account because they carry acoustic energy information associated to the propagated sound pressure levels. The ray-tube reflection procedure is the following. A wavenumber for each tube is computed by taking the average wavenumber of its three bounding rays. Then, the first ray that reflects from the tube is identified and the cross section area of the tube at this instance is computed. This cross section area is then projected to the ground. The final step is to restart the tube propagation away from the ground by using the projected area as the initial one. A scheme of this procedure is shown in Figure 4.8.

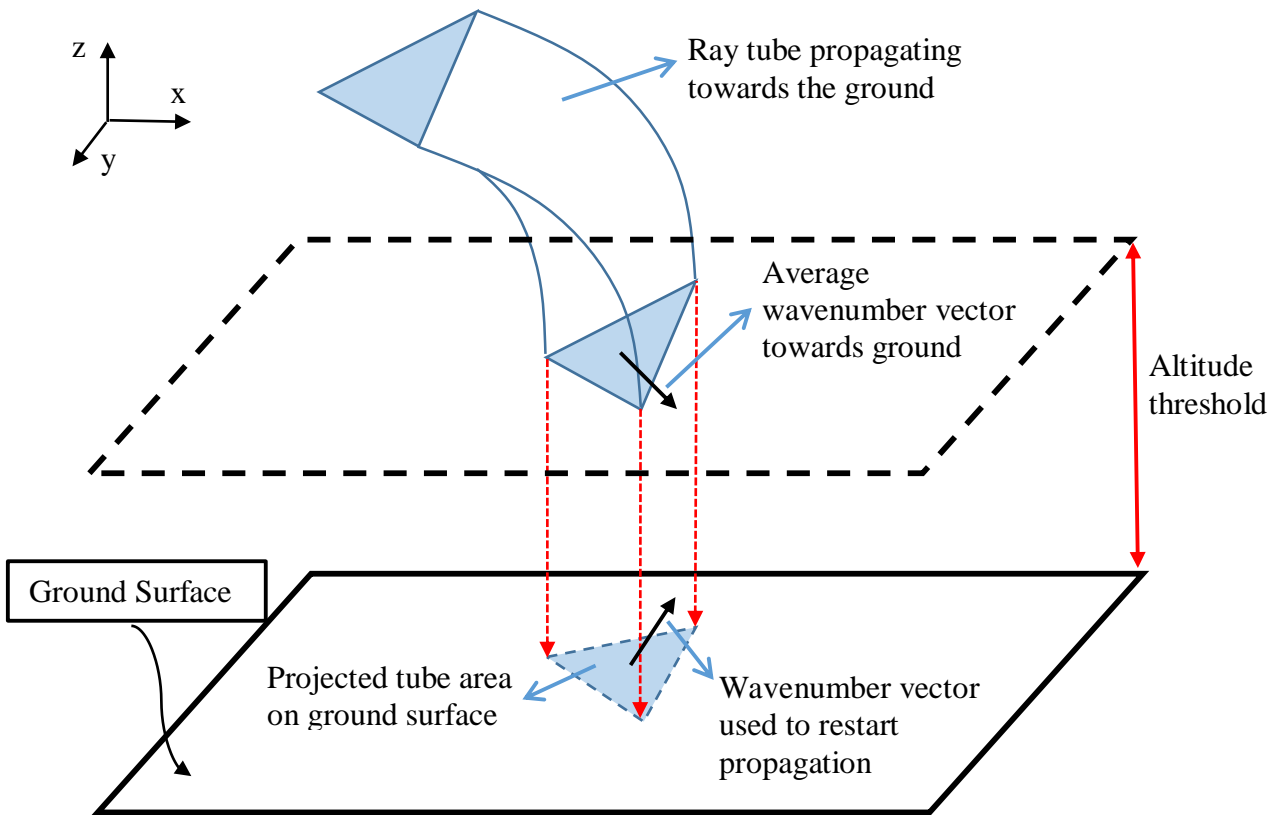


Figure 4.8: Ray tube ground reflections scheme.

The ray tube trajectories in space are calculated by averaging the trajectories of the three rays that enclose each tube. This is required to account for attenuation of sound and to identify points over the ground where the tube rays reflect. The sound pressure levels associated to the tubes at the moment of reflection are then used to interpolate over a microphone grid built on the ground. The interpolation involves traversing of a triangulation known-data structure and finding the triangles that enclose each query point. Then the value at the query points is computed through the weighted sum of values at the three vertices of the enclosing triangle.

The HRT method is not capable of prediction of noise on areas where there are no rays reflecting the ground (commonly referred to as the shadow zone). This constraint is not limited to HRT but to all ray tracing propagation methods. This phenomenon happens during propagation under two conditions. The first one corresponds to a negative speed of sound gradient (L'Espérance et al., 1992). In this case all rays tend to bend upwards, thus no ground reflections are possible. The second one happens when vertical wind velocities bend the rays away from the ground. This induces shadow zone areas over the ground. Berry et al. (1988) developed a method for noise prediction over these areas. The computation of the pressure in the shadow zone is beyond the scope of this thesis (see future work section).

4.5. NOISE PREDICTION RESULTS

This section provides results for a NREL 5MW reference turbine (J. M. Jonkman et al., 2009). The reason for selecting this turbine is that the blade geometry and other parameters are available in the open literature. The length of the blades is 61.5 meters and its maximum chord is 4.65 meters. The blade airfoil sections are composed of a series of circular, DU and NACA airfoils as shown in Figure 4.9.

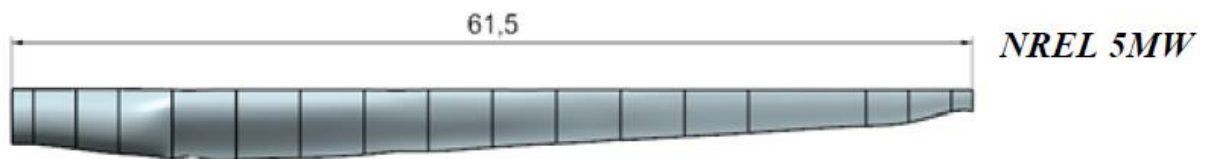


Figure 4.9: NREL 5 MW wind turbine blade.

The rated rotor speed is 12.1 rpm. For the simulations, it is assumed the hub height is 100 m and the turbine operates at 12 rpm with an inflow of 10 m/s at the hub. The turbine yaw and tilt angles are set to zero and the rotor is not coned either. The blades were divided in 5 span-wise elements and the rotation accounted for by taking 15 azimuth positions for a total of 75 sound sources distributed on the rotor plane. NAFNoise was used to predict the trailing edge noise for the 75 sound sources, e.g. leading edge noise was not modelled.

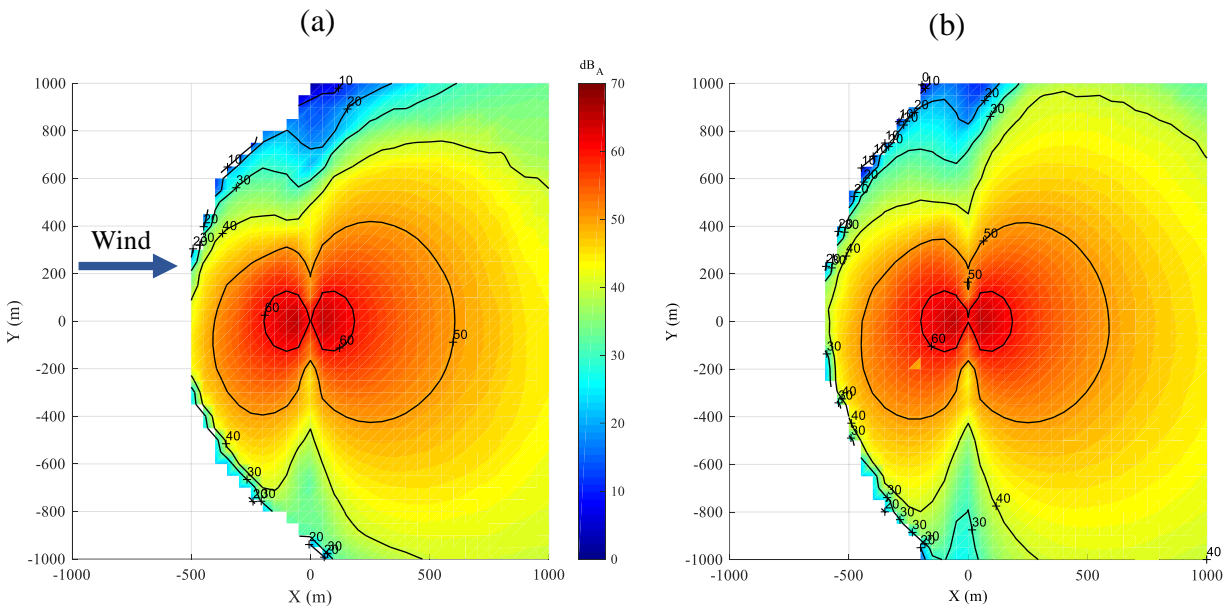


Figure 4.10: Equivalent Overall A-weighted sound pressure level noise map for one rotor revolution: (a) 2,562 and (b) 10,242 rays emitted by each of the 75 sound source.

The code computes the $1/3^{\text{rd}}$ octave band as well as overall A-weighted SPL (OASPL) spectrum for an array of microphones at each azimuth position of the rotor. In these simulations, a square grid of 1600 microphones was placed on the ground over an area of 2 km by 2 km. The turbine is at the centre in the domain. Background noise was not added to the turbine noise results. The resulting equivalent OASPL noise maps are shown in Figure 4.10. In this case, the same weather conditions as in Figure 3.10 are used, as well as the ground characteristics. The HRT was implemented to propagate 2,562 rays from the 75 noise spheres distributed along the three blades. Thus, 192,150 rays were emitted from the wind turbine for propagation with a computational time of approximately 2 hours for this case using Matlab (Figure 4.10a). Results show the characteristic directivity pattern of wind turbine noise i.e. dipole resembling. The noise map also shows higher

levels towards one side (right of downwind direction). Even though sound pressure levels over the shadow zone in the upwind direction are not known, it is safe to assume that they are very low i.e. as observed in Figure 5.1, below the 30 dBA line in the upwind direction. To assess convergence and computational time, a second simulation was performed with 10,242 rays emitted per sound source (a total of 768,150 rays emitted from the wind turbine). The result in Figure 4.10b shows nearly the same results, particularly close to the turbine. The main differences are in a reduction of the extent of the shadow region and the levels in the upper right region of the domain. The computational time for this case was approximately 12 hours.

5. CONCLUSIONS AND FUTURE WORK

The HRT model presented in this work is suitable but not limited to wind turbine noise applications. It is capable of propagating rays in 3D while maintaining low computational costs. Furthermore, it can take into account refraction effects due to atmospheric temperature variations. Complex flows can also be considered without excluding vertical wind velocity components. The latter is especially important for propagation of wind turbine noise because of the intricate turbulent flows formed along the turbine's downstream direction.

The Hamiltonian ray path equations are unique because they track wave phase changes during propagation. This is mathematically expressed with a set of coupled quasi-linear PDE's that define the behavior of bending and convective effects on the wavenumbers and ray paths. A simple ray path validation using analytical solutions shows that the Hamiltonian approach is highly accurate for propagation over long distances. Furthermore, the HRT acoustic pressure fields show improved accuracy and computational advantages over other more common propagation techniques, such as FFP and ERT methods. For wind turbine noise simulations, the HRT predictions showed characteristic wind turbine directivity patterns. Thus, proving its capabilities to predict noise from complex moving noise sources.

Overall, it can be concluded that the developed HRT model provides the necessary accuracy, computational efficiency, and physical insight for atmospheric noise propagation involving noise produced by wind turbines. It presents many advantages over more common numerical and analytical propagation models, as well as those used by commercial software.

Future work includes addressing many issues complementary to the HRT propagation such as developing and implementing solutions for prediction over shadow regions. Regarding ground reflections and attenuation, Fresnel zones can also be used as briefly described in section 2.3. In addition, non-uniform terrain and scattering zones should be addressed in order to be able to predict noise over realistic environments. Alternatives to ray-tube energy calculations should also be

investigated, including the implementation of Gaussian beams as described in section 2.2 and the transport equation shown in section 2.1 as a second alternative.

When comparing the HRT and the popular ERT method, it is clear that the ERT is limited by its large numerical errors and computational efficiency. Further research regarding the sources of the ERT numerical and ray path errors should be addressed. Moreover, even though the HRT method is capable of computing sound pressure levels at any location in space i.e. it is not limited to ground predictions, this work does not include the identification of caustics zones. Caustics zones are areas where all the three bounding rays of a tube converge, thus predicting infinite and erroneous sound pressure level prediction.

REFERENCES

- Amiet, R. K. (1975). Acoustic radiation from an airfoil in a turbulent stream. *Journal of Sound and Vibration*, 41(4), 407-420. doi:10.1016/S0022-460X(75)80105-2
- ANSI. (2010). American National Standard Method for Determining the Acoustic Impedance of Ground Surfaces. In *ANSI/ASA S1.18*.
- ANSI. (2014). Methods for Calculation of the Absorption of Sound by the Atmosphere. In *ANSI/ASA S1.26*.
- Arakawa, C., Fleig, O., Iida, M., & Shimooka, M. (2005). Numerical approach for noise reduction of wind turbine blade tip with earth simulator. *Journal of the Earth Simulator*, 2(3), 11-33.
- Attenborough, K. (1987). On the acoustic slow wave in air-filled granular media. *The Journal of the Acoustical Society of America*, 81(1), 93-102. doi:10.1121/1.394938
- Attenborough, K. (2005). *Outdoor Ground Impedance*. Paper presented at the EuroNoise 2015.
- Attenborough, K., Bashir, I., & Taherzadeh, S. (2011). Outdoor ground impedance models. *The Journal of the Acoustical Society of America*, 129(5), 2806-2819. doi:10.1121/1.3569740
- Attenborough, K., Li, K. M., & Horoshenkov, K. (2007). *Predicting outdoor sound*. New York;London;: Taylor & Francis.
- Bailly, C., & Juvé, D. (2000). Numerical Solution of Acoustic Propagation Problems Using Linearized Euler Equations. *AIAA Journal*, 38(1), 22-29. doi:10.2514/2.949
- Barlas, E., Zhu, W. J., Shen, W. Z., Kelly, M., & Andersen, S. J. (2017). Effects of wind turbine wake on atmospheric sound propagation. *Applied Acoustics*, 122, 51-61. doi:https://doi.org/10.1016/j.apacoust.2017.02.010
- Bass, H. E. (1990). Atmospheric absorption of sound: Update. *The Journal of the Acoustical Society of America*, 88(4), 2019-2021. doi:10.1121/1.400176
- Bass, H. E. (1995). Atmospheric absorption of sound: Further developments. *The Journal of the Acoustical Society of America*, 97(1), 680. doi:10.1121/1.412989
- Bass, H. E. (1996). Erratum: Atmospheric absorption of sound: Further developments. *The Journal of the Acoustical Society of America*, 99(2), 1259-1259.
- Behrouzifar, A., Darbandi, M., & Schneider, G. E. (2015). Numerical Investigation of Actuator Disc Thickness Effect on Predicting the Performance and Far Wake of the Horizontal Axis Wind Turbine. (57342), V001T001A042. doi:10.1115/IMECE2015-52074
- Bérenghier, M. C., Gauvreau, B., Blanc-Benon, P., & Juve, D. (2003). *Outdoor sound propagation: a short review on analytical and numerical approaches*. Paper presented at the 6th French Conference on Acoustics, 8-11 April 2002, Germany.
- Bérenghier, M. C., Stinson, M. R., Daigle, G. A., & Hamet, J. F. (1997). Porous road pavements: Acoustical characterization and propagation effects. *The Journal of the Acoustical Society of America*, 101(1), 155-162. doi:10.1121/1.417998
- Berry, A., & Daigle, A. (1988). Controlled experiments of the diffraction of sound by a curved surface. *The Journal of the Acoustical Society of America*, 83(6), 2047-2058. doi:10.1121/1.396385
- Bolin, K., Boué, M., & Karasalo, I. (2009). Long range sound propagation over a sea surface. *The Journal of the Acoustical Society of America*, 126(5), 2191-2197. doi:10.1121/1.3238236
- Bowdler, D., Leventhall, G., & Raspet, R. (2012). Wind turbine noise. *The Journal of the Acoustical Society of America* 132(2), 1233.
- Brokesova, J. (2006). *Asymptotic Ray Method in Seismology*. Prague, Czech Republic: MATFYZPRESS.

- Brooks, T., Pope, S., & Marcolini, M. (1989). *Airfoil self-noise and prediction* (NASA-RP-1218, L-16528, NAS 1.61:1218). Retrieved from Hampton, VA, United States: <http://ntrs.nasa.gov/search.jsp?R=19890016302>
- Brouwer, H. H. (2014). A Ray Acoustics Model for the Propagation of Aircraft Noise through the Atmosphere. *International Journal of Aeroacoustics*, 13(5-6), 363-383. doi:10.1260/1475-472X.13.5-6.363
- Buck, S., Palo, S., & Moriarty, P. (2013). *Application of phased array techniques for amplitude modulation mitigations*. Paper presented at the 5th international conference on wind turbine noise, Denver, Colorado.
- Burley, C., & Pope, S. (2014). *APET User Guide*. Retrieved from
- Červený, V. (2001). *Seismic ray theory*. Cambridge;New York;: Cambridge University Press.
- Cheng, R. (2007). *Long-range wind turbine noise propagation by the parabolic equation method*. (Dissertation/Thesis), ProQuest Dissertations Publishing,
- Chessell, C. I. (1973). Three-dimensional acoustic-ray tracing in an inhomogeneous anisotropic atmosphere using Hamilton's equations. *The Journal of the Acoustical Society of America*, 53(1), 83-87. doi:10.1121/1.1913331
- Chessell, C. I. (1977). Propagation of noise along a finite impedance boundary. *The Journal of the Acoustical Society of America*, 62(4), 825-834. doi:10.1121/1.381603
- Chien, C. F., & Soroka, W. W. (1975). Sound propagation along an impedance plane. *Journal of Sound and Vibration*, 43(1), 9-20. doi:http://dx.doi.org/10.1016/0022-460X(75)90200-X
- Chien, C. F., & Soroka, W. W. (1980). A note on the calculation of sound propagation along an impedance surface. *Journal of Sound and Vibration*, 69(2), 340-343. doi:10.1016/0022-460X(80)90618-5
- Coton, F. N., & Wang, T. (1999). The prediction of horizontal axis wind turbine performance in yawed flow using an unsteady prescribed wake model. *Proceedings of the Institution of Mechanical Engineers*, 213(1), 33.
- Cotté, B., & Blanc-Benon, P. (2009). Time-domain simulations of sound propagation in a stratified atmosphere over an impedance ground. *The Journal of the Acoustical Society of America*, 125(5), EL202-EL207. doi:10.1121/1.3104633
- Defrance, J., Salomons, E., Noordhoek, I., Heimann, D., Plovsing, B., Watts, G., . . . de Roo, F. (2007). Outdoor sound propagation reference model developed in the European Harmonoise project. *Acta Acustica United With Acustica*, 93(2), 213-227.
- Delany, M. E., & Bazley, E. N. (1970). Acoustical properties of fibrous absorbent materials. *Applied Acoustics*, 3(2), 105-116. doi:http://dx.doi.org/10.1016/0003-682X(70)90031-9
- Devenport, W., Burdisso, R. A., Camargo, H., Crede, E., Remillieux, M., Rasnick, M., & Van Seeters, P. (2010). *Aeroacoustic Testing of Wind Turbine Airfoils*. Retrieved from
- Deygout, J. (1966). Multiple knife-edge diffraction of microwaves. *IEEE Transactions on Antennas and Propagation*, 14(4), 480-489. doi:10.1109/TAP.1966.1138719
- Diagle, G. (1994). Review of Physical Mechanism and Computational Models (Outdoor Propagation). *Journal of the Canadian Acoustical Association* 22(3), 117-118.
- Dieminger, W., Hartmann, G. K., & Leitinger, R. (1996). *The upper atmosphere: data analysis and interpretation*. New York;Berlin;: Springer-Verlag.
- Drela, M., & Youngren, H. (2001). *XFOIL 6.94 User Guide*. Retrieved from Cambridge, Massachusetts:
- Ducosson, I. (2006). *Wind Turbine Noise Propagation Over Flat Ground*. (Master's Program in Sound and Vibration), Chamlers University of Technology, Gotenorg, Sweden.

- Embleton, T. F. W., Piercy, J. E., & Daigle, G. A. (1983). Effective flow resistivity of ground surfaces determined by acoustical measurements. *The Journal of the Acoustical Society of America*, 74(4), 1239-1244. doi:10.1121/1.390029
- Embleton, T. F. W., Thiessen, G. J., & Piercy, J. E. (1976). Propagation in an inversion and reflections at the ground. *The Journal of the Acoustical Society of America*, 59(2), 278-282. doi:10.1121/1.380883
- ESDU. (1989). *The Calculation of Overground Sound Propagation in the Presence of Wind and Temperature Gradients* (ESDU 89036). Retrieved from
- Evans, L. B., Bass, H. E., & Sutherland, L. C. (1972). Atmospheric Absorption of Sound: Theoretical Predictions. *The Journal of the Acoustical Society of America*, 51(5B), 1565-1575. doi:10.1121/1.1913000
- Forssén, J., Schiff, M., Pedersen, E., & Waye, K. P. (2010). Wind Turbine Noise Propagation over Flat Ground: Measurements and Predictions. *Acta Acustica united with Acustica*, 96(4), 753-760. doi:10.3813/aaa.918329
- Georges, T., Jones, R., & Riley, J. (1986). Simulating ocean acoustic tomography measurements with Hamiltonian ray tracing. *IEEE Journal of Oceanic Engineering*, 11(1), 58-71. doi:10.1109/JOE.1986.1145142
- Glauert, H. (1930). Aerodynamic Theory. *Journal of the Royal Aeronautical Society*, 34(233), 409-414. doi:10.1017/S0368393100114397
- Goldman, B. (2013). *Modifications to Psu-wopwop For Enhanced Noise Prediction Capabilities*. (Master of Science), Pennsylvania State University, State College, Pennsylvania.
- Guntur, S., Jonkman, J. M., Jonkman, B., Wang, Q., Sprague, M. A., Hind, M., . . . Schreck, S. J. (2016). FAST v8 Verification and Validation for a MW-scale Wind Turbine with Aeroelastically Tailored Blades. In *34th Wind Energy Symposium: American Institute of Aeronautics and Astronautics*.
- GWEC. (2016). *Global Wind Report: Annual Market Update 2015*. Retrieved from <http://www.gwec.net/publications/global-wind-report-2/>
- Hairer, E. (2008). *The Numerical Solution of Differential Algebraic Systems*. New York: Springer.
- Hansen, C. H., Doolan, C. J., & Hansen, K. L. (2017). *Wind farm noise: measurement, assessment and control*. Hoboken: John Wiley & Sons Inc.
- Hansen, M., Sørensen, J. N., Voutsinas, S., Sørensen, N., & Madsen, H. A. (2006). State of the art in wind turbine aerodynamics and aeroelasticity. *Progress in Aerospace Sciences*, 42(4), 285-330. doi:http://dx.doi.org/10.1016/j.paerosci.2006.10.002
- Hansen, M. O. L. (2015). *Aerodynamics of wind turbines*. New York, NY: Routledge.
- Harris, C. M. (1966). Absorption of Sound in Air versus Humidity and Temperature. *The Journal of the Acoustical Society of America*, 40(1), 148. doi:10.1121/1.1910031
- Hidaka, T., Kageyama, K., & Masuda, S. (1985). Sound propagation in the rest atmosphere with linear sound velocity profile. *Journal of the Acoustical Society of Japan (E)*, 6(2), 117-125. doi:10.1250/ast.6.117
- Hornikx, M., Waxler, R., & Forssén, J. (2010). The extended Fourier pseudospectral time-domain method for atmospheric sound propagation. *The Journal of the Acoustical Society of America*, 128(4), 1632-1646. doi:10.1121/1.3474234
- Huber, J., & Barrington, J. P. (2002). Three dimensional atmospheric propagation module for noise prediction. In *40th AIAA Aerospace Sciences Meeting & Exhibit: American Institute of Aeronautics and Astronautics*.

- IEC. (2006). Wind Turbine Generator Systems Part 11: Acoustic noise measurement techniques. In *IEC 61400-11:2002+AI:2006*.
- Iomin, A., & Zaslavsky, G. M. (2003). Sensitivity of ray paths to initial conditions. *Communications in Nonlinear Science and Numerical Simulation*, 8(3), 401-413. doi:http://dx.doi.org/10.1016/S1007-5704(03)00034-0
- ISO. (1993). Acoustics-Attenuation of Sound During Propagation Outdoors-Part 1. In *ISO 9613-1*.
- ISO. (1996). Acoustics-Attenuation of Sound During Propagation Outdoors-Part 2. In *ISO 9613-2*.
- Jensen, B. K., W.;Porter, M.;Schmidt, H. (2011). *Computational ocean acoustics* (Vol. 2nd;2.). New York: Springer.
- Johansson, L. (2003). *Sound Propagation Around Off-Shore Wind Turbines: Long-Range Parabolic Equation Calculations for Baltic Sea Conditions*. (Licentiate), Royal Institute of Technology, Stockholm, Sweden. (ISSN 1651-5536)
- Jonkman, J. M., Hayman, G.J., Jonkman, B.J., Damiani, R.R., Murray, R.E. . (2017). *AeroDyn v15 User's Guide and Theory Manual*. Retrieved from Golden, Colorado:
- Jonkman, J. M., & Marshall, L. b. (2005). *FAST User's Guide* (NREL/EL-500-38230). Retrieved from Golden, Colorado:
- Jonkman, J. M., & National Renewable Energy, L. (2009). *Definition of a 5-MW reference wind turbine for offshore system development*. Retrieved from
- Kaliski, K., Duncan, E., Wilson, D. K., & Vecherin, S. (2011). *Improving Predictions of Wind Turbine Noise using PE Modeling*. Paper presented at the NOISE-CON, Portland, Oregon.
- Kampanis, N., & Ekaterinaris, J. (2001). Numerical Prediction of Far-Field Turbine Noise Over a Terrain of Moderate Complexity. *Systems Analysis Modelling Simulation*, 41, 107-121.
- Kim, H., Lee, S., Son, E., Lee, S., & Lee, S. (2012). Aerodynamic noise analysis of large horizontal axis wind turbines considering fluid–structure interaction. *Renewable Energy*, 42, 46-53. doi:http://dx.doi.org/10.1016/j.renene.2011.09.019
- Kim, T., Petersen, M. M., & Larsen, T. J. (2014). A comparison study of the two-bladed partial pitch turbine during normal operation and an extreme gust conditions. *Journal of Physics: Conference Series*, 524(1), 012065.
- Kinsler, L. E. (2000). *Fundamentals of acoustics* (Vol. 4th). New York: Wiley.
- Komatsu, T. (2008). Improvement of the Delany-Bazley and Miki models for fibrous sound-absorbing materials. *Acoustical Science and Technology*, 29(2), 121-129. doi:10.1250/ast.29.121
- Koyanagi, S. i., Nakano, T., & Kawabe, T. (2008). Application of Hamiltonian of ray motion to room acoustics. *The Journal of the Acoustical Society of America*, 124(2), 719-722. doi:10.1121/1.2946714
- L'Espérance, A., Nicolas, J. R., Herzog, P., & Daigle, G. A. (1992). Heuristic model for outdoor sound propagation based on an extension of the geometrical ray theory in the case of a linear sound speed profile. *Applied Acoustics*, 37(2), 111-139. doi:http://dx.doi.org/10.1016/0003-682X(92)90022-K
- Lamancusa, J. S., & Daroux, P. A. (1993). Ray tracing in a moving medium with two-dimensional sound-speed variation and application to sound propagation over terrain discontinuities. *The Journal of the Acoustical Society of America*, 93(4), 1716-1726. doi:doi:http://dx.doi.org/10.1121/1.406737
- Larsen, T. J., & Hansen, M. (2007). *How 2 HAWC2, the user's manual*. Retrieved from Denmark:

- Lee, S., Lee, D., & Honhoff, S. (2016). Prediction of far-field wind turbine noise propagation with parabolic equation. *The Journal of the Acoustical Society of America*, *140*(2), 767-778. doi:10.1121/1.4958996
- Leloudas, G., Zhu, W. J., Sørensen, J. N., Shen, W. Z., & Hjort, S. (2007). Prediction and Reduction of Noise from a 2.3 MW Wind Turbine. *Journal of Physics: Conference Series*, *75*, 012083. doi:10.1088/1742-6596/75/1/012083
- Li, K. M., Attenborough, K., & Heap, N. W. (1991). Source height determination by ground effect inversion in the presence of a sound velocity gradient. *Journal of Sound and Vibration*, *145*(1), 111-128. doi:http://dx.doi.org/10.1016/0022-460X(91)90609-N
- Lighthill, M. J. S. (1978). *Waves in fluids*. New York;Cambridge [Eng.]: Cambridge University Press.
- Lowson, M. V. (1993). *Assesment and Prediction of Wind Turbine Noise* (ESTU-W--13/00284/REP). Retrieved from United Kingdom:
- Marsh, K. J. (1982). The concave model for calculating the propagation of noise from open-air industrial plants. *Applied Acoustics*, *15*(6), 411-428. doi:http://dx.doi.org/10.1016/0003-682X(82)90003-2
- Marten, D., & Wendler, J. (2013). *QBlade Guidelines v0.6*. Retrieved from
- Masson, C., Smaili, A., & Leclerc, C. (2001). Aerodynamic analysis of HAWTs operating in unsteady conditions. *Wind Energy*, *4*(1), 1-22. doi:10.1002/we.43
- McAninch, G. L., & Heath, S. L. (2006). *On The Determination of Shadow Boundaries and Relevant Eigenrays For Sound Propagation In Stratified Moving Media*. Paper presented at the 44th American Institute of Aeronautics and Astronautics (AIAA) Aerospace Sciences Meeting and Exhibit, Reno, NV; United States.
- Melnikov, Y. A., Borodin, V. N., & SpringerLink. (2017). *Green's Functions: Potential Fields on Surfaces* (Vol. 48). Cham: Springer International Publishing.
- Migliore, P., & Oerlemans, S. (2004). Wind Tunnel Aeroacoustic Tests of Six Airfoils for Use on Small Wind Turbines. *Journal of Solar Energy Engineering*, *126*(4), 974. doi:10.1115/1.1790535
- Miki, Y. (1990). Acoustical properties of porous materials-Modifications of Delany-Bazley models. *Journal of the Acoustical Society of Japan (E)*, *11*(1), 19-24. doi:10.1250/ast.11.19
- Miller, R. H. (1983). The aerodynamics and dynamic analysis of horizontal axis and wind turbines. *Journal of Wind Engineering and Industrial Aerodynamics*, *15*(1), 329-340. doi:http://dx.doi.org/10.1016/0167-6105(83)90202-7
- Mo, Q., Yeh, H., Lin, M., & Manocha, D. (2015). Analytic ray curve tracing for outdoor sound propagation. *Applied Acoustics*, *104*, 142-151. doi:10.1016/j.apacoust.2015.10.011
- Mo, Q., Yeh, H., Lin, M., & Manocha, D. (2017). Outdoor sound propagation with analytic ray curve tracer and Gaussian beam. *The Journal of the Acoustical Society of America*, *141*(3), 2289-2299. doi:10.1121/1.4977005
- Mo, Q., Yeh, H., & Manocha, D. (2016). Tracing Analytic Ray Curves for Light and Sound Propagation in Non-Linear Media. *IEEE Transactions on Visualization and Computer Graphics*, *22*(11), 2493-2506. doi:10.1109/TVCG.2015.2509996
- Moriarty, P. (2004). *AeroDyn Theory Manual* (NREL/EL-500-36881). Retrieved from
- Moriarty, P. (2005). *NAFNoise User's Guide*. Retrieved from Golden, Colorado:
- Moriarty, P., Guidati, G., & Migliore, P. (2005). Prediction of Turbulent Inflow and Trailing-Edge Noise for Wind Turbines. In *11th AIAA/CEAS Aeroacoustics Conference: American Institute of Aeronautics and Astronautics*.

- Moriarty, P., & Migliore, P. G. (2003). *Semi-empirical aeroacoustic noise prediction code for wind turbines*. Retrieved from Golden, Colorado:
- Mylonas, L. (2014). *Assessment of Noise Prediction Methods Over Water for Long Range Sound Propagation of Wind Turbines*. (Msc Wind Power Project Management), Uppsala University, Visby, Sweden.
- Ning, S. A. (2014). A simple solution method for the blade element momentum equations with guaranteed convergence. *Wind Energy*, 17(9), 1327-1345. doi:10.1002/we.1636
- Nobile, M. A., & Hayek, S. I. (1985). Acoustic propagation over an impedance plane. *The Journal of the Acoustical Society of America*, 78(4), 1325-1336. doi:10.1121/1.392902
- NORDTEST. (1999). Ground Surfaces: Determination of the Acoustic Impedance. In *NT ACOU 104*.
- Oerlemans, S. (2011). *An Explanation for enhanced amplitude modulation of wind turbine noise* (NLR-CR-2011-071). Retrieved from Amsterdam, The Netherlands:
- Oerlemans, S., Sijtsma, P., & Méndez López, B. (2007). Location and quantification of noise sources on a wind turbine. *Journal of Sound and Vibration*, 299(4-5), 869-883. doi:10.1016/j.jsv.2006.07.032
- Peng, Y. (2014). *Propagation of wind turbine noise through wakes and turbulent atmosphere*. (Dissertation/Thesis), ProQuest Dissertations Publishing,
- Pinder, J. N. (1992). Mechanical Noise from Wind Turbines. *Wind Engineering*, 16(3), 158-168.
- Plovsig, B. (2006a). *Nord 2000. Comprehensive Outdoor Sound Propagation Model. Part 1: Propagation in an Atmosphere without Significant Refraction*. (AV1849/00). Retrieved from Denmark:
- Plovsig, B. (2006b). *Propagation in an Atmosphere without Significant Refraction* (AV 1849/00). Retrieved from
- Plovsig, B. (2006). *Nord 2000. Comprehensive Outdoor Sound Propagation Model. Part 2: Propagation in an Atmosphere with Refraction*. Retrieved from
- Porter, M. B., & Bucker, H. P. (1987). Gaussian beam tracing for computing ocean acoustic fields. *The Journal of the Acoustical Society of America*, 82(4), 1349-1359. doi:10.1121/1.395269
- Porter, M. B., & Liu, Y. (1994). Finite Element Ray Tracing. *Theoretical and Computational Acoustics*, 2, 947-956.
- Prospathopoulos, J. M. (2007). Application of a ray theory model to the prediction of noise emissions from isolated wind turbines and wind parks. *Wind energy (Chichester, England)*, 10(2), 103-119. doi:10.1002/we.211
- Prospathopoulos, J. M., & Voutsinas, S. G. (2005). Noise Propagation Issues in Wind Energy Applications. *Journal of Solar Energy Engineering*, 127(2), 234-241. doi:10.1115/1.1862257
- Raman, G. (2016). A review of wind turbine noise measurements and regulations. *Wind engineering*, 40(4), 319-342. doi:10.1177/0309524X16649080
- Rasmussen, K. B. (1986). Outdoor sound propagation under the influence of wind and temperature gradients. *Journal of Sound and Vibration*, 104(2), 321-335. doi:http://dx.doi.org/10.1016/0022-460X(86)90271-3
- Rayleigh, S. (1945). *Theory of Sound* (2nd, Revis ed. Vol. 1). Mineola: Dover Publications, Incorporated.
- Rosenbaum, J. E. (2011). *Enhanced propagation modeling of directional aviation noise: A hybrid parabolic equation-fast field program method*. (3471859 Ph.D.), The Pennsylvania State University, Ann Arbor. ProQuest Dissertations & Theses Global database.

- Salomons, E., van Maercke, D., Defrance, J., & de Roo, F. (2011). The Harmonoise Sound Propagation Model. *Acta Acustica united with Acustica*, 97(1), 62-74. doi:10.3813/AAA.918387
- Salomons, E. M. (1998). Improved Green's function parabolic equation method for atmospheric sound propagation. *The Journal of the Acoustical Society of America*, 104(1), 100-111. doi:http://dx.doi.org/10.1121/1.423260
- Salomons, E. M. (2001). *Computational atmospheric acoustics*. Dordrecht, Boston: Kluwer Academic Publishers.
- Sanderse, B. (2009). *Aerodynamics of Wind Turbine Wakes: Literature Review* (ECN-E-09-016). Retrieved from
- Shirzadeh, R., Weijtjens, W., Guillaume, P., & Devriendt, C. (2015). The dynamics of an offshore wind turbine in parked conditions: a comparison between simulations and measurements. *Wind Energy*, 18(10), 1685-1702. doi:10.1002/we.1781
- Slawsky, L. M., Zhou, L., Roy, S. B., Xia, G., Vuille, M., & Harris, R. A. (2015). Observed Thermal Impacts of Wind Farms Over Northern Illinois. *Sensors*, 15(7), 14981-15005. doi:10.3390/s150714981
- Son, E., Kim, H., Kim, H., Choi, W., & Lee, S. (2010). Integrated numerical method for the prediction of wind turbine noise and the long range propagation. *Current Applied Physics*, 10(2), S316-S319. doi:http://dx.doi.org/10.1016/j.cap.2009.11.034
- Sørensen, J. N. r., & Shen, W. Z. (2002). Numerical Modeling of Wind Turbine Wakes. *Journal of Fluids Engineering*, 124(2), 393-399. doi:10.1115/1.1471361
- Sutherland, L. C. (2004). Atmospheric absorption in the atmosphere up to 160 km. *The Journal of the Acoustical Society of America*, 115(3), 1012-1032. doi:10.1121/1.1631937
- Taraldsen, G. (2005). The Delany-Bazley impedance model and Darcy's law. *Acta Acustica united with Acustica*, 91(1), 41-50.
- Taraldsen, G., & Jonasson, H. (2011). Aspects of ground effect modeling. *The Journal of the Acoustical Society of America*, 129(1), 47-53. doi:10.1121/1.3500694
- Tuinstra, M. (2014). A Fast Atmospheric Sound Propagation Model for Aircraft Noise Prediction. *International Journal of Aeroacoustics*, 13(5-6), 337-361. doi:doi:10.1260/1475-472X.13.5-6.337
- van den Berg, G. P. (2005). The Beat is Getting Stronger: The Effect of Atmospheric Stability on Low Frequency Modulated Sound of Wind Turbines. *Journal of Low Frequency Noise, Vibration and Active Control*, 24(1), 1-23. doi:10.1260/0263092054037702
- van Maercke, D., & Salomons, E. (2009). *The Harmonoise sound propagation model: further developments and comparison with other models*. Paper presented at the NAG/DAGA 2009, Rotterdam, The Netherlands.
- Virieux, J., Garnier, N., Blanc, E., & Dessa, J. X. (2004). Paraxial ray tracing for atmospheric wave propagation. *Geophysical Research Letters*, 31(20), n/a-n/a. doi:10.1029/2004GL020514
- Wagner, S., Bareiß, R., Guidati, G., & SpringerLink. (1996). *Wind Turbine Noise* (1 ed.). Berlin, Heidelberg: Springer Berlin Heidelberg.
- Wasala, S. H., Storey, R. C., Norris, S. E., & Cater, J. E. (2015). Aeroacoustic noise prediction for wind turbines using Large Eddy Simulation. *Journal of Wind Engineering and Industrial Aerodynamics*, 145, 17-29. doi:http://dx.doi.org/10.1016/j.jweia.2015.05.011
- Wilson, D. K. (1997). Simple, relaxational models for the acoustical properties of porous media. *Applied Acoustics*, 50(3), 171-188. doi:10.1016/S0003-682X(96)00048-5

- Wu, D. (2017). *The Effect of Blade Aeroelasticity and Turbine Parameters on Wind Turbine Noise*. (Mster of Science), Virginia Poltechnic Institute and State University, Blacksburg, VA.
- Zauderer, E. (2006). *Partial differential equations of applied mathematics* (Vol. 3rd). Hoboken, N.J: Wiley-Interscience.
- Zayas, J., Derby, M., Gilman, P., Ananthan, S., Lantz, E., Cotrell, J., . . . Tusing, R. (2015). *Enabling Wind Power Nationwide*. Retrieved from
- Zhu, W. J. (2004). *Modelling of Noise From Wind Turbines*. (M.Sc. in Wind Energy), Technical University of Denmark, Kongens Lyngby, Denmark.
- Zhu, W. J., Heilskov, N., Shen, W. Z., & Sørensen, J. N. (2005). Modeling of Aerodynamically Generated Noise From Wind Turbines. *Journal of Solar Energy Engineering*, 127(4), 517-528. doi:10.1115/1.2035700
- Zhu, W. J., Sørensen, J. N., & Shen, W. Z. (2005). An Aerodynamic Noise Propagation Model for Wind Turbines. *Wind Engineering*, 29(2), 129-141. doi:doi:10.1260/0309524054797168

APPENDIX A: AERODYNAMIC *BEM* METHOD

The Blade Element Momentum (BEM) method for aerodynamic rotor is described below (M. O. L. Hansen, 2015). The development of this technique was initiated in the work by Glauert (1930). It combines momentum theory with local physical characteristics along the blades.

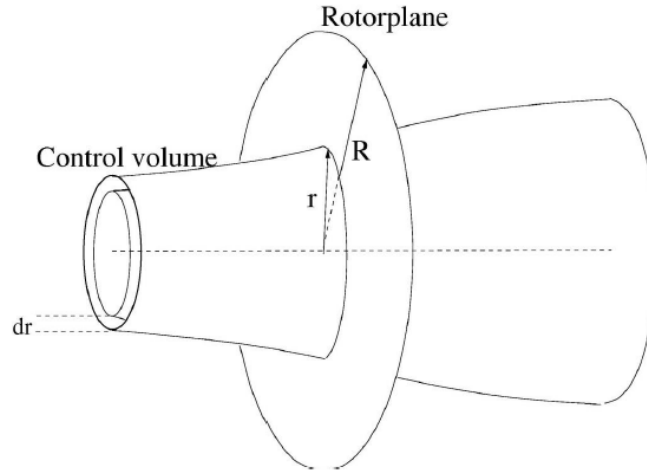


Figure A.1: Annular control volume used for BEM method (M. O. L. Hansen, 2015).

From momentum theory, an expression for the thrust and torque produced by the wind turbine is obtained. If the flow over a wind turbine is bounded by a control volume consisting of annular stream tubes (see Figure A.1), then the thrust (dT) and torque (dM) is

$$dT = (V_0 - u_1) d\dot{m} = 2\pi r \rho u (V_0 - u_1) dr \quad (\text{A.1})$$

$$dM = r C_\theta d\dot{m} = 2\pi r^2 \rho u C_\theta dr \quad (\text{A.2})$$

In this case, ρ is air's density, and the flow velocities u , u_1 and V_0 are shown in Figure A.2a. On the other hand, C_θ is the azimuthal component of flow velocity at the trailing edge of the rotor blades as shown in Figure A.2b.

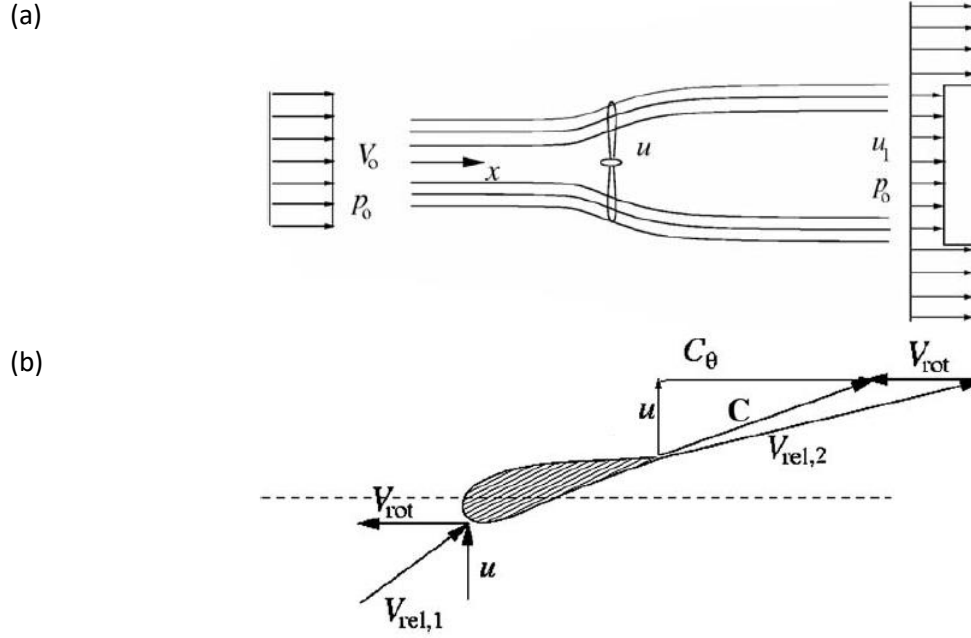


Figure A.1: (a) BEM control volume flow velocities and (b) trailing edge velocity triangle for a single airfoil (Hansen, 2015).

Velocities u and u_1 are related to V_0 by a constant named the axial induction factor as follows

$$u = (1-a)V_0 \quad (\text{A.3})$$

$$u_1 = (1-2a)V_0 \quad (\text{A.4})$$

In addition, C_θ is related to the rotor's angular velocity ω by means of the tangential induction factor, as follows

$$C_\theta = 2a'\omega r \quad (\text{A.5})$$

If equations (A.3) through (A.5) are used with equations (A.1) and (A.2), then the thrust and torque become

$$dT = 4\pi r \rho V_0^2 a(1-a) dr \quad (\text{A.6})$$

$$dM = 4\pi r^3 \rho V_0 \omega (1-a) a' dr \quad (\text{A.7})$$

The differential torque and moment can also be obtained by locally analyzing the velocities at the trailing edge of a single airfoil 2D section. The flow angles and the velocity components used for analysis are shown in Figure A.3a. In addition, the loads acting on the airfoil are shown in Figure A.3b.

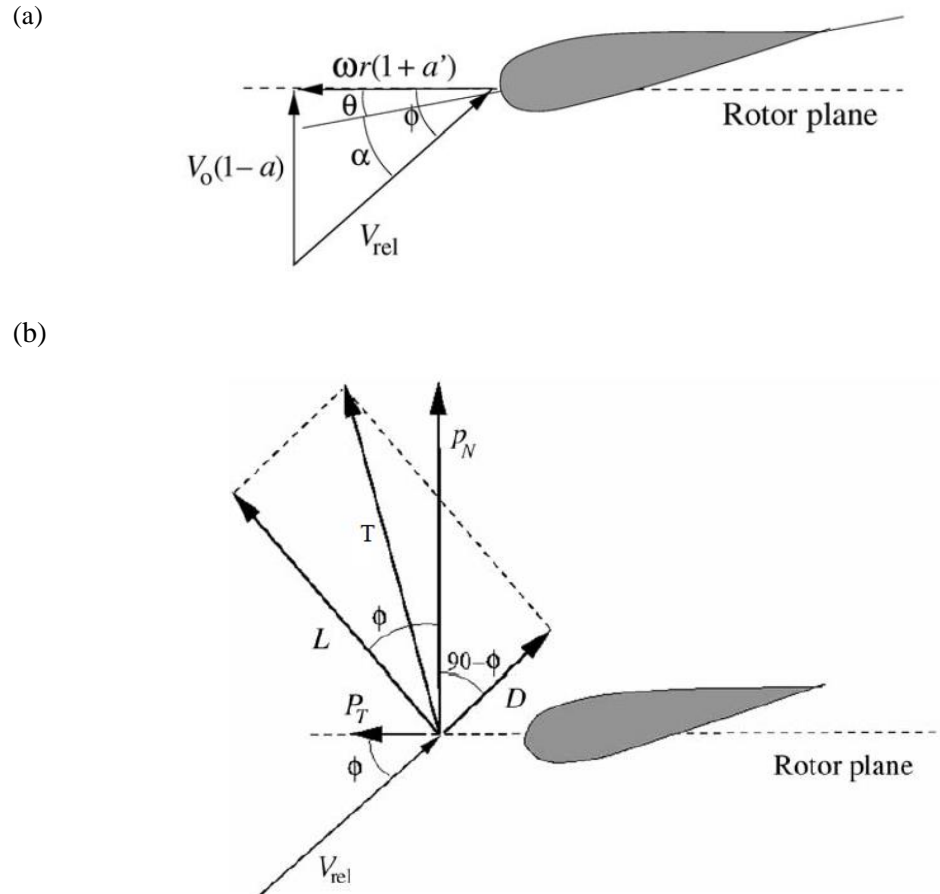


Figure A.3: (a) Flow velocity components at airfoils leading edge and angles and (b) Forces acting on a single airfoil section (M. O. L. Hansen, 2015).

The normal and tangential loads P_N and P_T can be trigonometrically obtained from Figure A.3. These loads are responsible for the rotation of the rotor and the thrust that it produces. The torque and moment produced by them are the following

$$dT = BP_N dr = \frac{1}{2} \rho B \frac{V_0^2 (1-a)^2}{\sin^2 \phi} cC_n dr \quad (\text{A.8})$$

$$dM = rBP_T dr = \frac{1}{2} \rho B \frac{V_0^2 (1-a) \omega r (1+a')}{\sin \phi \cos \phi} c C_t r dr \quad (\text{A.9})$$

Where, c is the airfoil's chord, B is the number of blades of the wind turbine, $C_n = P_n / \frac{1}{2} \rho V_{rel}^2 c$ is the normal load coefficient and $C_t = P_T / \frac{1}{2} \rho V_{rel}^2 c$ is the tangential load coefficient. If equations (A.8) and (A.9) are equated to equations (A.1) and (A.2), respectively, then an expression for both the axial and tangential coefficients is found. That is

$$a = \frac{1}{\frac{4 \sin^2 \phi}{\sigma C_n} + 1} \quad (\text{A.10})$$

$$a' = \frac{1}{\frac{4 \sin \phi \cos \phi}{\sigma C_t} - 1} \quad (\text{A.11})$$

The BEM procedure is determined by the presented momentum theory and flow characteristics over an airfoil. It iteratively computes the values for both the axial and tangential induction factors as well as normal and tangential loads, until a reduced error between iterations is reached. From the BEM method, the angle of attack is one of the most important calculated parameters needed for aeroacoustic noise prediction.

In order to improve physical accuracy, some corrections can also be implemented into the BEM method. For example, the Prandtl correction factor F takes into account the vortex system formed at the wake of the wind turbine. On the other hand, a Glauert correction determines the correct empirical relationship between the thrust coefficient C_T (normalized thrust of the wind turbine to the available power in a cross section equal to the swept area by the blades) and the axial induction factor. For large axial induction factors, momentum theory fails to predict and accurate thrust coefficient.

A BEM algorithm is presented below. It includes Glauert and Prandtl corrections. Its inputs are the following:

- I. Data for each individual airfoil along the blade:
 - Local twist angle (θ_T) and radial locations along the blade (r).
 - Lift (C_L) and drag (C_D) coefficients for an adequate range of angles of attack.
 - Airfoil chord (c).
- II. General turbine's parameters:
 - Number of blades (B).
 - Blade pitch angle (θ).
 - Rotor radius (R).
 - Rotor rotation velocity (ω).
- III. Environmental conditions:
 - Wind speed (V_0).
 - Air density (ρ).

Once all the inputs are correctly defined, the BEM code follows the next steps for each individual airfoil located at an annular distance r from the center of the rotor:

1. Compute the airfoil solidity σ

$$\sigma = \frac{cB}{2\pi r} \quad (\text{A.12})$$

2. The axial and tangential induction factors are initialized to zero ($a = 0$ and $a' = 0$).
3. The flow angle ϕ is computed

$$\phi = \tan^{-1} \frac{(1-a)V_0}{(1+a')\omega r} \quad (\text{A.13})$$

4. The local angle of attack is determined by subtracting the local pitch (Total blade pitch θ_p plus local blade twist θ_T) from the flow angle

$$\alpha = (\theta_p + \theta_r) - \phi = \theta - \phi \quad (\text{A.14})$$

5. The lift and drag coefficients are read from the input for the angle of attack computed on the previous step.
6. The normal and tangential load coefficients are calculated

$$C_n = C_l \cos \phi + C_d \sin \phi \quad (\text{A.15})$$

$$C_t = C_l \sin \phi - C_d \cos \phi \quad (\text{A.16})$$

7. The axial and tangential induction factors have to be updated as follows:

- a. Compute the thrust coefficient

$$C_T = \frac{(1-a)^2 \sigma C_n}{\sin^2 \phi} \quad (\text{A.17})$$

- b. Compute Prandtl's tip loss correction factor

$$F = \frac{2}{\pi} \cos^{-1}(e^{-f}) \quad (\text{A.18})$$

where, $f = \frac{B}{2} \frac{R-r}{r \sin \phi}$.

- c. Update the axial induction factor using Glauert's correction

$$C_T = \begin{cases} 4a(1-a)F & \text{if } a \leq \frac{1}{3} \\ 4a(1 - \frac{1}{4}(5-3a)a)F & \text{if } a > \frac{1}{3} \end{cases} \quad (\text{A.19})$$

- d. Update tangential induction factor

$$a' = \frac{1}{\frac{4F \sin \phi \cos \phi}{\sigma C_t} - 1} \quad (\text{A.20})$$

8. If the values for the axial and tangent factors have changed more than a specific tolerance (usually around 10^{-4}), then go back to step three. If the values for the axial and tangent factors have changed more than a specific tolerance then continue to step nine.
9. The relative velocity component is calculated ($V_{rel} = V_0(1 - a)/\sin\phi$). Finally, the local loads in the normal and tangential directions to the rotor plane, P_N and P_T , are computed as follows

$$P_N = \frac{1}{2} \rho V_{rel}^2 c C_n \quad (\text{A.21})$$

$$P_T = \frac{1}{2} \rho V_{rel}^2 c C_t \quad (\text{A.22})$$

APPENDIX B: AERODYNAMIC NOISE SOURCES

All the airfoil self-noise mechanisms are described in this section. The first four mechanisms formulation was developed by (Brooks et al., 1989). These are semi-empirical models based on wind tunnel measurements of NACA 0012 airfoils. The last mechanism (TI) formulation was developed by Amiet (1975) and Lawson (1993).

Turbulent Boundary Layer-Trailing Edge Noise (TBL-TE)

The first noise source is determined by the interaction between the turbulent boundary layer and the trailing edge of the airfoil, as shown in Figure B.1.

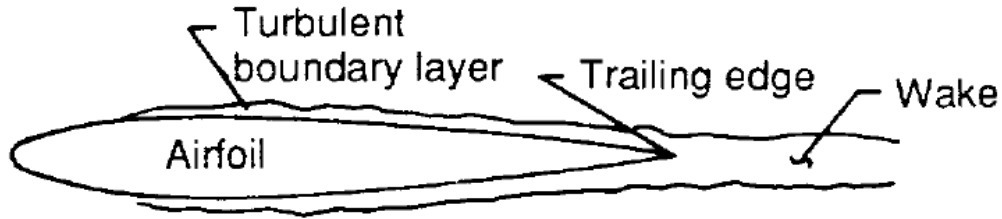


Figure B.1: Turbulent Boundary Layer-Trailing Edge Noise (Brooks et al., 1989).

This type of noise source is very common at high Reynolds numbers, and it can originate in both the suction and pressure side of an airfoil. The noise produced for the pressure side is computed as follows

$$L_{p(TBL-TE)} = 10 \log_{10} \left[\frac{\delta^* M^5 L D_h}{r_e^2} \right] + A \left(\frac{S_t}{S_{t1}} \right) + (K_1 - 3) + \Delta K_1 \quad (\text{B.1})$$

Where δ^* is the boundary layer thickness in meters, M is the Mach number, and L is the span of the airfoil in meters. D_h is the noise directivity, r_e is the distance to the observer, St is the Strouhal number, $t_1 = 0.02M^6$, $K_1(Re_c)$ is an empirical function that depends on the Reynolds number based on the chord Re_c . On the other hand, $\Delta K_1(\alpha, Re_{\delta^*})$ is an empirical function that depends on the Reynolds number and is based on boundary layer thickness δ^* and the angle of attack. Finally

A is an empirical spectral shape obtained from experimentation. In the case of the suction side, a similar equation is used (P. Moriarty et al., 2003).

Separated Flow Noise (SF)

As the angle of attack of an airfoil is larger, the lift to drag coefficient gets smaller. This is because the size of the turbulent boundary layer on the suction side becomes larger (see Figure B.2). This causes stalling and thus large amounts of noise. The equation for the noise produced in this case is similar to equation (B.1), the difference is that it contains different empirical functions that are only a function of the angle of attack (P. Moriarty et al., 2003).

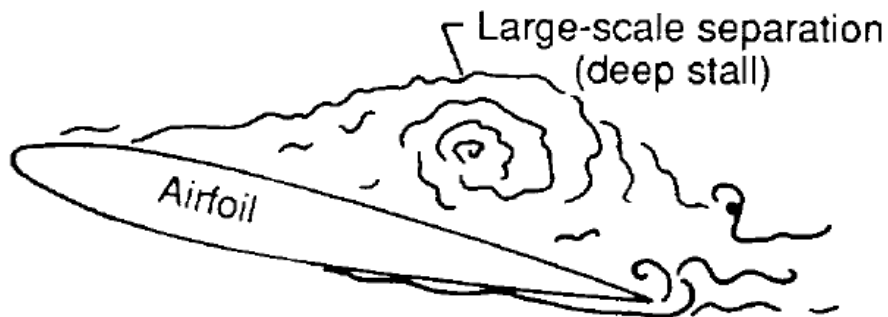


Figure B.2: Flow Separation Noise (Brooks et al., 1989).

Laminar Boundary Layer-Vortex Shedding Noise (LBL)

In this case, the noise is generated when there is a feedback loop, caused by the interaction of the laminar boundary layer and the vortices that are being shed at the trailing edge of the airfoil, as shown (see Figure B.3). This type of mechanism has more probability of being present at the pressure side of an airfoil, and is tonal in nature because of the amplification caused by the feedback loop (P. Moriarty et al., 2003).

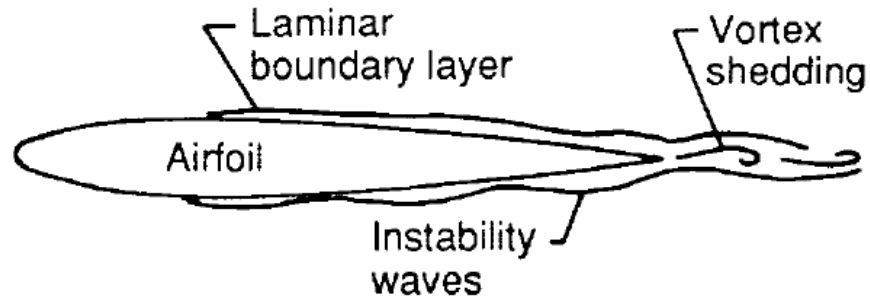


Figure B.3: Laminar Boundary Layer-Vortex Shedding Noise (Brooks et al., 1989).

The noise produced by this source is computed using the following equation

$$L_{p(LBL)} = 10 \log_{10} \left[\frac{\delta^* M^5 L D_h}{r_c^2} \right] + G_1 \left(\frac{St'}{St'_{peak}} \right) + G_2 \left(\frac{Re_c}{Re'_c} \right) + G_3(\alpha) \quad (B.2)$$

In this case, α is the angle of attack, On the other hand, G_1 , G_2 , and G_3 are empirical relation functions dependent on St' (Strouhal number with respect to the boundary layer thickness) and $Re_c(\alpha)$ (Reynolds number with respect to the angle of attack α). St'_{peak} and Re'_c are reference Strouhal and Reynolds numbers (P. Moriarty et al., 2003) .

Trailing Edge Bluntness-Vortex Shedding Noise (TEB)

The geometry of the trailing edge of an airfoil can be responsible for vortex shedding generation. If the airfoil trailing edge's thickness is very large compared to the boundary layer thickness, the bluntness vortex shedding noise will be a dominant one. This phenomenon is shown in Figure B.4.

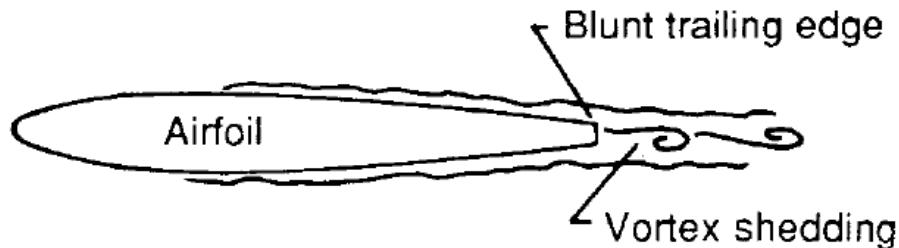


Figure B.4: Trailing Edge Bluntness-Vortex Shedding Noise (Brooks et al., 1989).

The noise produced by this type of mechanism is computed as follows

$$L_{p(TEB)} = 10 \log_{10} \left[\frac{\delta^* M^5 L D_h}{r_e^2} \right] + G_4 \left(\frac{h}{\delta_{avg}^*}, \Psi \right) + G_5 \left(\frac{h}{\delta_{avg}^*}, \Psi, \frac{St''}{St''_{peak}} \right) \quad (B.3)$$

Where, G_4 and G_5 are empirical relation functions that depend on the following parameters: δ_{avg}^* is the average boundary layer thickness, h is the trailing edge thickness, ψ is the trailing edge angle (this angle is defined between the two airfoil surfaces on the airfoil's pressure and suction side that meet at the trailing edge). On the other hand, St'' and St''_{peak} are the Strouhal numbers with respect to h and h/δ_{avg}^* , respectively (P. Moriarty et al., 2003).

Turbulent Inflow Noise (TI)

This mechanism is characterized by the interaction of turbulent incoming flow and the leading edge of an airfoil. It becomes of great importance when the turbulent eddies from the incoming flow are significantly larger than the airfoils leading edge radius. The noise produced by this mechanism is calculated as follows

$$L_{p(inflow)} = L_{p(inflow)}^H + 10 \log_{10} \left[\frac{LFC}{1 + LFC} \right] \quad (B.4)$$

Where,

$$L_{p(inflow)}^H = 10 \log_{10} \left[\frac{\rho_0^2 c_0^2 \lambda L}{2r_e^2} M^3 u^2 I^2 \frac{k^3}{(1+k^2)^{7/3}} D_L \right] + 58.4 \quad (B.5)$$

In this case ρ_0 corresponds to the air density, c_0 is the speed of sound, λ is the turbulence scale (parameter used according to International Electrotechnical Commission-IEC standard), u is the wind mean speed, I is percentage of wind turbulence, D_L is a directivity function, and M is the Mach number. K is the local wavenumber given by $K = \pi f c / U$ (f is the frequency in Hz, c is the local airfoil chord, and U is the local flow velocity over the airfoil). On the other hand, stands for Low Frequency Correction Factor and is given by

$$LFC = 10 S^2 M K^2 \beta^{-2} \quad (B.6)$$

Where, $S^2 = \left(\frac{2\pi K}{\beta^2} + \left(1 + 2.4 \frac{K}{\beta^2} \right)^{-1} \right)^{-1}$, and $\beta^2 = 1 - M^2$ (P. Moriarty et al., 2003).

Airfoil Self-Noise Directivity

All the airfoil self-noise mechanisms described above contain a term that accounts for directivity. Both high frequency directivity D_H and the low frequency one D_L corrections are defined for an observer relative to the trailing edge of the airfoil. They are defined as follows

$$D_H(\Theta, \Phi) \approx \frac{2 \sin^2\left(\frac{1}{2}\Theta\right) \sin^2 \Phi}{(1 + M \cos \Theta)(1 + (M - M_c) \cos \Theta)^2} \quad (\text{B.7})$$

$$D_L(\Theta_e, \Phi_e) \approx \frac{\sin^2 \Theta_e \sin^2 \Phi_e}{(1 + M \cos \Theta_e)^4} \quad (\text{B.8})$$

Where, Θ_e and Φ_e are two directivity angles defined at a coordinate system at the trailing edge of the airfoil. This coordinate system accounts for refractive and Doppler effects triggered by the flow velocity around the airfoil (Brooks et al., 1989). Figure 0.5 shows a flat plate representing the airfoil with its coordinate system located at the trailing edge. Both directivity angles used in equations (B.7) and (B.8) angles are also shown with respect to a stationary observer.

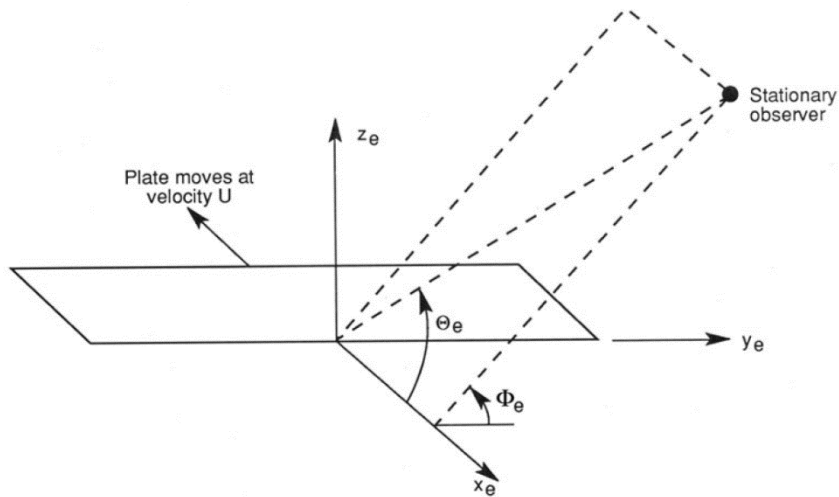


Figure B.5: Airfoil-self noise directivity angles (Brooks et al., 1989).

On the other hand, M is the Mach number and M_c is the convective Mach number. Note that for the case where θ_e and ϕ_e are equal to 90 degrees, both directivity functions are equal to one (Brooks et al., 1989).

APPENDIX C: EIKONAL EQUATIONS SOLUTION

The solution for the Eikonal equation in (2.53) will be addressed in this section, following the formulation by Brouwer (2014). First, the notation from equation (2.53) is changed for the sake easier mathematical manipulation as follows

$$|\vec{q}|^2 = \left(\frac{1 - \vec{V} \cdot \vec{q}}{c^2(\vec{r})} \right)^2 \quad (\text{C.1})$$

Where, $\vec{q} = \nabla\tau$ (recall that this vector corresponds to the wave front gradient and τ is the wave front). Brouwer (2014) determined that by the method of characteristics, equation (C.1) can be decomposed in the following wave front and ray's location equations

$$\begin{aligned} \frac{\partial q_x}{\partial t} &= -\sqrt{q_x^2 + q_y^2 + q_z^2} \frac{\partial c}{\partial x} + \left[q_y \left(\frac{\partial V_y}{\partial x} - \frac{\partial V_x}{\partial y} \right) + q_z \left(\frac{\partial V_z}{\partial x} - \frac{\partial V_x}{\partial z} \right) \right] + V_x \left(\frac{\partial q_x}{\partial x} + \frac{\partial q_y}{\partial y} + \frac{\partial q_z}{\partial z} \right) \\ \frac{\partial q_y}{\partial t} &= -\sqrt{q_x^2 + q_y^2 + q_z^2} \frac{\partial c}{\partial y} - \left[q_x \left(\frac{\partial V_y}{\partial x} - \frac{\partial V_x}{\partial y} \right) - q_z \left(\frac{\partial V_z}{\partial y} - \frac{\partial V_y}{\partial z} \right) \right] + V_y \left(\frac{\partial q_x}{\partial x} + \frac{\partial q_y}{\partial y} + \frac{\partial q_z}{\partial z} \right) \\ \frac{\partial q_z}{\partial t} &= -\sqrt{q_x^2 + q_y^2 + q_z^2} \frac{\partial c}{\partial z} + \left[-q_x \left(\frac{\partial V_z}{\partial x} - \frac{\partial V_x}{\partial z} \right) - q_y \left(\frac{\partial V_z}{\partial y} - \frac{\partial V_y}{\partial z} \right) \right] + V_z \left(\frac{\partial q_x}{\partial x} + \frac{\partial q_y}{\partial y} + \frac{\partial q_z}{\partial z} \right) \end{aligned} \quad (\text{C.2})$$

$$\begin{aligned} \frac{\partial x}{\partial t} &= \frac{cq_x}{|\vec{q}|} + V_x \\ \frac{\partial y}{\partial t} &= \frac{cq_y}{|\vec{q}|} + V_y \\ \frac{\partial z}{\partial t} &= \frac{cq_z}{|\vec{q}|} + V_z \end{aligned} \quad (\text{C.3})$$

If wind and temperature only have a component in the x-axis, equations (C.2) and(C.3) become

$$\begin{aligned} \frac{\partial q_x}{\partial t} &= -q_z \frac{\partial V_x}{\partial z} + V_x \left(\frac{\partial q_x}{\partial x} + \frac{\partial q_y}{\partial y} + \frac{\partial q_z}{\partial z} \right) \\ \frac{\partial q_y}{\partial t} &= 0 \\ \frac{\partial q_z}{\partial t} &= -\sqrt{q_x^2 + q_y^2 + q_z^2} \frac{\partial c}{\partial z} + q_x \frac{\partial V_x}{\partial z} \end{aligned} \quad (\text{C.4})$$

$$\frac{\partial x}{\partial t} = \frac{cq_x}{|\vec{q}|} + V_x \quad (\text{C.5})$$

$$\frac{\partial y}{\partial t} = \frac{cq_y}{|\vec{q}|}$$

$$\frac{\partial z}{\partial t} = \frac{cq_z}{|\vec{q}|}$$

These equations are numerically solved through a second order Runge Kutta method. This method is based on a numerical trapezoidal approximation for an integral. To solve a first order differential equation such as $dx/dt = f(x, t)$, its integral is approximated with the trapezoidal rule as follows

$$x_{n+1} - x_n = \int_{t_n}^{t_{n+1}} f(x, t) dt \approx \frac{\Delta t}{2} [f(x_n, t_n) + f(x_{n+1}, t_{n+1})] \quad (\text{C.6})$$

However, since x_{n+1} is not known it must be approximated using forward Euler's rule: $x_{n+1} \approx x_n + \Delta t f(x_n, t_n)$. Thus, the programmed runge-kutta follows the next steps:

1. Evaluate $f(x_n, t_n)$:

$$R_1 = f(x_n, t_n) \quad (\text{C.7})$$

2. Apply Euler's rule by computing:

$$x_n + \Delta t R_1 = x_n + \Delta t f(x_n, t_n) \quad (\text{C.8})$$

3. Evaluate :

$$R_2 = f(x_n + \Delta t R_1, t_{n+1}) \quad (\text{C.9})$$

4. Apply the trapezoidal rule

$$x_{n+1} = x_n + \frac{\Delta t}{2} (R_1 + R_2) \quad (\text{C.10})$$

This is an iterative procedure method. It is a second order method and it iterates twice before giving the final solution. The RungeKutta solving method applied to the Eikonal equations are the following:

1. Evaluate the functions at t_n :

Solve for ray path location

$$\begin{aligned} R_{1,x} &= c(x_n, y_n, z_n) \frac{q_{x,n}}{\sqrt{q_{x,n}^2 + q_{y,n}^2 + q_{z,n}^2}} + V_{x,n}(x_n, y_n, z_n) \\ R_{1,y} &= c(x_n, y_n, z_n) \frac{q_{y,n}}{\sqrt{q_{x,n}^2 + q_{y,n}^2 + q_{z,n}^2}} \\ R_{1,z} &= c(x_n, y_n, z_n) \frac{q_{z,n}}{\sqrt{q_{x,n}^2 + q_{y,n}^2 + q_{z,n}^2}} \end{aligned} \quad (\text{C.11})$$

Solve for wavefront gradient

$$\begin{aligned} R_{1,q_x} &= -q_z(x_n, y_n, z_n) \frac{\partial V_x}{\partial z}(x_n, y_n, z_n) + \dots \\ &V_x(x_n, y_n, z_n) \left(\frac{\partial q_x}{\partial x}(x_n, y_n, z_n) + \frac{\partial q_y}{\partial y}(x_n, y_n, z_n) + \frac{\partial q_z}{\partial z}(x_n, y_n, z_n) \right) \\ R_{1,q_y} &= 0 \\ R_{1,q_z} &= -\sqrt{q_x(x_n, y_n, z_n)^2 + q_y(x_n, y_n, z_n)^2 + q_z(x_n, y_n, z_n)^2} \frac{\partial c}{\partial z}(x_n, y_n, z_n) + \dots \\ &q_x(x_n, y_n, z_n) \frac{\partial V_x}{\partial z}(x_n, y_n, z_n) \end{aligned} \quad (\text{C.12})$$

2. Apply Euler's rule:

Solve for ray path location

$$\begin{aligned} x_n + \Delta t R_{1,x} \\ y_n + \Delta t R_{1,y} \\ z_n + \Delta t R_{1,z} \end{aligned} \quad (\text{C.13})$$

Solve for wavefront gradient

$$\begin{aligned}
q_{x,n} + \Delta t R_{1,q_x} \\
q_{y,n} + \Delta t R_{1,q_y} \\
q_{z,n} + \Delta t R_{1,q_z}
\end{aligned} \tag{C.14}$$

3. Evaluate the functions at t_{n+1} :

Solve for ray path location

$$\begin{aligned}
R_{2,x} &= c(x_n + \Delta t R_{1,x}, y_n + \Delta t R_{1,y}, z_n + \Delta t R_{1,z}) \times \dots \\
&\frac{q_{x,n} + \Delta t R_{1,q_x}}{\sqrt{(q_{x,n} + \Delta t R_{1,q_x})^2 + (q_{y,n} + \Delta t R_{1,q_y})^2 + (q_{z,n} + \Delta t R_{1,q_z})^2}} + V_{x,n}(x_n + \Delta t R_{1,x}, y_n + \Delta t R_{1,y}, z_n + \Delta t R_{1,z}) \\
R_{2,y} &= c(x_n + \Delta t R_{1,x}, y_n + \Delta t R_{1,y}, z_n + \Delta t R_{1,z}) \frac{q_{y,n} + \Delta t R_{1,q_y}}{\sqrt{(q_{x,n} + \Delta t R_{1,q_x})^2 + (q_{y,n} + \Delta t R_{1,q_y})^2 + (q_{z,n} + \Delta t R_{1,q_z})^2}} \\
R_{2,z} &= c(x_n + \Delta t R_{1,x}, y_n + \Delta t R_{1,y}, z_n + \Delta t R_{1,z}) \frac{q_{z,n} + \Delta t R_{1,q_z}}{\sqrt{(q_{x,n} + \Delta t R_{1,q_x})^2 + (q_{y,n} + \Delta t R_{1,q_y})^2 + (q_{z,n} + \Delta t R_{1,q_z})^2}}
\end{aligned} \tag{C.15}$$

Solve for wavefront gradient

$$\begin{aligned}
R_{1,q_x} &= -q_z(x_n + \Delta t R_{1,x}, y_n + \Delta t R_{1,y}, z_n + \Delta t R_{1,z}) \frac{\partial V_x}{\partial z}(x_n + \Delta t R_{1,x}, y_n + \Delta t R_{1,y}, z_n + \Delta t R_{1,z}) + \dots \\
V_x(x_n + \Delta t R_{1,x}, y_n + \Delta t R_{1,y}, z_n + \Delta t R_{1,z}) &\times \left[\frac{\partial q_x}{\partial x}(x_n + \Delta t R_{1,x}, y_n + \Delta t R_{1,y}, z_n + \Delta t R_{1,z}) + \dots \right. \\
&\left. \frac{\partial q_y}{\partial y}(x_n + \Delta t R_{1,x}, y_n + \Delta t R_{1,y}, z_n + \Delta t R_{1,z}) + \frac{\partial q_z}{\partial z}(x_n + \Delta t R_{1,x}, y_n + \Delta t R_{1,y}, z_n + \Delta t R_{1,z}) \right] \\
R_{1,q_y} &= 0 \\
R_{1,q_z} &= -[q_x(x_n + \Delta t R_{1,x}, y_n + \Delta t R_{1,y}, z_n + \Delta t R_{1,z})^2 + \dots \\
&q_y(x_n + \Delta t R_{1,x}, y_n + \Delta t R_{1,y}, z_n + \Delta t R_{1,z})^2 + q_z(x_n + \Delta t R_{1,x}, y_n + \Delta t R_{1,y}, z_n + \Delta t R_{1,z})^2]^{0.5} \times \dots \\
&\frac{\partial c}{\partial z}(x_n + \Delta t R_{1,x}, y_n + \Delta t R_{1,y}, z_n + \Delta t R_{1,z}) + q_x(x_n + \Delta t R_{1,x}, y_n + \Delta t R_{1,y}, z_n + \Delta t R_{1,z}) \frac{\partial V_x}{\partial z} \times \dots \\
&(x_n + \Delta t R_{1,x}, y_n + \Delta t R_{1,y}, z_n + \Delta t R_{1,z})
\end{aligned} \tag{C.16}$$

4. Apply the trapezoidal rule

Solve for ray path location

$$x_{n+1} = x_n + \frac{\Delta t}{2} (R_{1,x} + R_{2,x}) \quad (\text{C.17})$$

$$y_{n+1} = y_n + \frac{\Delta t}{2} (R_{1,y} + R_{2,y})$$

$$z_{n+1} = z_n + \frac{\Delta t}{2} (R_{1,z} + R_{2,z})$$

Solve for wavefront gradient

$$q_{x,n+1} = q_{x,n} \quad (\text{C.18})$$

$$q_{y,n+1} = q_{y,n}$$

$$q_{z,n+1} = q_{z,n} + \frac{\Delta t}{2} (R_{1,k_z} + R_{2,k_z})$$

Alternatively, a fourth order Runge-Kutta method, that iterates four times before obtaining the results at one-step further in time, can also be implemented.

APPENDIX D: 4TH ORDER RUNGE-KUTTA HRT SOLUTION

A fourth order Runge-Kutta numerical method is used to solve first order differential equations of the form $dx/dt = f(x, t)$ (Hairer, 2008). This section provides the procedure that should be followed when using this method, specifically for the HRT equations in (3.57).

A generic Runge-Kutta method must follow the next steps:

1. Evaluate $R_1 = f(x_n, t_n)$ (initial conditions required at time t_n)
2. Evaluate $R_2 = f\left(x_n + \frac{\Delta t}{2} R_1, t_{n+1/2}\right)$
3. Evaluate $R_3 = f\left(x_n + \frac{\Delta t}{2} R_2, t_{n+1/2}\right)$
4. Evaluate $R_4 = f(x_n + \Delta t R_3, t_{n+1})$
5. Obtain the results at the next time step:

$$x_{n+1} = x_n + \frac{\Delta t}{6} (R_1 + 2R_2 + 2R_3 + R_4) \quad (\text{D.1})$$

If the fourth order Runge-Kutta steps specified above are applied to the HRT propagation equations in (3.57), then the following is obtained:

1. Evaluate the functions at t_n :

Solve for ray path location

$$R_{1,x} = c(x_n, y_n, z_n) \frac{k_{x,n}}{\sqrt{k_{x,n}^2 + k_{y,n}^2 + k_{z,n}^2}} + V_{x,n}(x_n, y_n, z_n)$$

$$R_{1,y} = c(x_n, y_n, z_n) \frac{k_{y,n}}{\sqrt{k_{x,n}^2 + k_{y,n}^2 + k_{z,n}^2}} + V_{y,n}(x_n, y_n, z_n)$$

$$R_{1,z} = c(x_n, y_n, z_n) \frac{k_{z,n}}{\sqrt{k_{x,n}^2 + k_{y,n}^2 + k_{z,n}^2}} + V_{z,n}(x_n, y_n, z_n)$$

Solve for wavenumber

$$R_{1,k_x} = 0$$

$$R_{1,k_y} = 0$$

$$R_{1,k_z} = -\sqrt{k_{x,n}^2 + k_{y,n}^2 + k_{z,n}^2} \frac{\partial c}{\partial z}(x_n, y_n, z_n) - k_{x,n} \frac{\partial V_x}{\partial z}(x_n, y_n, z_n)$$

2. Evaluate $R_2 = f\left(x_n + \frac{\Delta t}{2} R_1, t_{n+1/2}\right)$

Solve for ray path location

$$R_{2,x} = c\left(x_n + \frac{\Delta t}{2} R_{1,x}, y_n + \frac{\Delta t}{2} R_{1,y}, z_n + \frac{\Delta t}{2} R_{1,z}\right) \frac{k_{x,n} + \frac{\Delta t}{2} R_{1,k_x}}{\sqrt{\left(k_{x,n} + \frac{\Delta t}{2} R_{1,k_x}\right)^2 + \left(k_{y,n} + \frac{\Delta t}{2} R_{1,k_y}\right)^2 + \left(k_{z,n} + \frac{\Delta t}{2} R_{1,k_z}\right)^2}} + V_{x,n}\left(x_n + \frac{\Delta t}{2} R_{1,x}, y_n + \frac{\Delta t}{2} R_{1,y}, z_n + \frac{\Delta t}{2} R_{1,z}\right)$$

$$R_{2,y} = c\left(x_n + \frac{\Delta t}{2} R_{1,x}, y_n + \frac{\Delta t}{2} R_{1,y}, z_n + \frac{\Delta t}{2} R_{1,z}\right) \frac{k_{y,n} + \frac{\Delta t}{2} R_{1,k_y}}{\sqrt{\left(k_{x,n} + \frac{\Delta t}{2} R_{1,k_x}\right)^2 + \left(k_{y,n} + \frac{\Delta t}{2} R_{1,k_y}\right)^2 + \left(k_{z,n} + \frac{\Delta t}{2} R_{1,k_z}\right)^2}} + V_{y,n}\left(x_n + \frac{\Delta t}{2} R_{1,x}, y_n + \frac{\Delta t}{2} R_{1,y}, z_n + \frac{\Delta t}{2} R_{1,z}\right)$$

$$R_{2,z} = c\left(x_n + \frac{\Delta t}{2} R_{1,x}, y_n + \frac{\Delta t}{2} R_{1,y}, z_n + \frac{\Delta t}{2} R_{1,z}\right) \frac{k_{z,n} + \frac{\Delta t}{2} R_{1,k_z}}{\sqrt{\left(k_{x,n} + \frac{\Delta t}{2} R_{1,k_x}\right)^2 + \left(k_{y,n} + \frac{\Delta t}{2} R_{1,k_y}\right)^2 + \left(k_{z,n} + \frac{\Delta t}{2} R_{1,k_z}\right)^2}} + V_{z,n}\left(x_n + \frac{\Delta t}{2} R_{1,x}, y_n + \frac{\Delta t}{2} R_{1,y}, z_n + \frac{\Delta t}{2} R_{1,z}\right)$$

Solve for wavenumber

$$R_{2,k_x} = 0$$

$$R_{2,k_y} = 0$$

$$R_{2,k_z} = -\sqrt{\left(k_{x,n} + \frac{\Delta t}{2} R_{1,k_x}\right)^2 + \left(k_{y,n} + \frac{\Delta t}{2} R_{1,k_y}\right)^2 + \left(k_{z,n} + \frac{\Delta t}{2} R_{1,k_z}\right)^2} \frac{\partial c}{\partial z}\left(x_n + \frac{\Delta t}{2} R_{1,x}, y_n + \frac{\Delta t}{2} R_{1,y}, z_n + \frac{\Delta t}{2} R_{1,z}\right) - \left(k_{x,n} + \frac{\Delta t}{2} R_{1,k_x}\right) \frac{\partial V_x}{\partial z}\left(x_n + \frac{\Delta t}{2} R_{1,x}, y_n + \frac{\Delta t}{2} R_{1,y}, z_n + \frac{\Delta t}{2} R_{1,z}\right)$$

3. Evaluate $R_3 = f\left(x_n + \frac{\Delta t}{2} R_2, t_{n+1/2}\right)$

Solve for ray path location

$$R_{3,x} = c(x_n + \frac{\Delta t}{2} R_{2,x}, y_n + \frac{\Delta t}{2} R_{2,y}, z_n + \frac{\Delta t}{2} R_{2,z}) \frac{k_{x,n} + \frac{\Delta t}{2} R_{2,k_x}}{\sqrt{\left(k_{x,n} + \frac{\Delta t}{2} R_{2,k_x}\right)^2 + \left(k_{y,n} + \frac{\Delta t}{2} R_{2,k_y}\right)^2 + \left(k_{z,n} + \frac{\Delta t}{2} R_{2,k_z}\right)^2}} + V_{x,n}(x_n + \frac{\Delta t}{2} R_{2,x}, y_n + \frac{\Delta t}{2} R_{2,y}, z_n + \frac{\Delta t}{2} R_{2,z})$$

$$R_{3,y} = c(x_n + \frac{\Delta t}{2} R_{2,x}, y_n + \frac{\Delta t}{2} R_{2,y}, z_n + \frac{\Delta t}{2} R_{2,z}) \frac{k_{y,n} + \frac{\Delta t}{2} R_{2,k_y}}{\sqrt{\left(k_{x,n} + \frac{\Delta t}{2} R_{2,k_x}\right)^2 + \left(k_{y,n} + \frac{\Delta t}{2} R_{2,k_y}\right)^2 + \left(k_{z,n} + \frac{\Delta t}{2} R_{2,k_z}\right)^2}} + V_{y,n}(x_n + \frac{\Delta t}{2} R_{2,x}, y_n + \frac{\Delta t}{2} R_{2,y}, z_n + \frac{\Delta t}{2} R_{2,z})$$

$$R_{3,z} = c(x_n + \frac{\Delta t}{2} R_{2,x}, y_n + \frac{\Delta t}{2} R_{2,y}, z_n + \frac{\Delta t}{2} R_{2,z}) \frac{k_{z,n} + \frac{\Delta t}{2} R_{2,k_z}}{\sqrt{\left(k_{x,n} + \frac{\Delta t}{2} R_{2,k_x}\right)^2 + \left(k_{y,n} + \frac{\Delta t}{2} R_{2,k_y}\right)^2 + \left(k_{z,n} + \frac{\Delta t}{2} R_{2,k_z}\right)^2}} + V_{z,n}(x_n + \frac{\Delta t}{2} R_{2,x}, y_n + \frac{\Delta t}{2} R_{2,y}, z_n + \frac{\Delta t}{2} R_{2,z})$$

Solve for wavenumber

$$R_{3,k_x} = 0$$

$$R_{3,k_y} = 0$$

$$R_{3,k_z} = -\sqrt{\left(k_{x,n} + \frac{\Delta t}{2} R_{2,k_x}\right)^2 + \left(k_{y,n} + \frac{\Delta t}{2} R_{2,k_y}\right)^2 + \left(k_{z,n} + \frac{\Delta t}{2} R_{2,k_z}\right)^2} \frac{\partial c}{\partial z}(x_n + \frac{\Delta t}{2} R_{2,x}, y_n + \frac{\Delta t}{2} R_{2,y}, z_n + \frac{\Delta t}{2} R_{2,z}) - \left(k_{x,n} + \frac{\Delta t}{2} R_{2,k_x}\right) \frac{\partial V_x}{\partial z}(x_n + \frac{\Delta t}{2} R_{2,x}, y_n + \frac{\Delta t}{2} R_{2,y}, z_n + \frac{\Delta t}{2} R_{2,z})$$

4. Evaluate $R_4 = f(x_n + \Delta t R_3, t_{n+1})$

Solve for ray path location

$$R_{4,x} = c(x_n + \Delta t R_{3,x}, y_n + \Delta t R_{3,y}, z_n + \Delta t R_{3,z}) \frac{k_{x,n} + \Delta t R_{3,k_x}}{\sqrt{\left(k_{x,n} + \Delta t R_{3,k_x}\right)^2 + \left(k_{y,n} + \Delta t R_{3,k_y}\right)^2 + \left(k_{z,n} + \Delta t R_{3,k_z}\right)^2}} + V_{x,n}(x_n + \Delta t R_{3,x}, y_n + \Delta t R_{3,y}, z_n + \Delta t R_{3,z})$$

$$R_{4,y} = c(x_n + \Delta t R_{3,x}, y_n + \Delta t R_{3,y}, z_n + \Delta t R_{3,z}) \frac{k_{y,n} + \Delta t R_{3,k_y}}{\sqrt{\left(k_{x,n} + \Delta t R_{3,k_x}\right)^2 + \left(k_{y,n} + \Delta t R_{3,k_y}\right)^2 + \left(k_{z,n} + \Delta t R_{3,k_z}\right)^2}} + V_{y,n}(x_n + \Delta t R_{3,x}, y_n + \Delta t R_{3,y}, z_n + \Delta t R_{3,z})$$

$$R_{4,z} = c(x_n + \Delta t R_{3,x}, y_n + \Delta t R_{3,y}, z_n + \Delta t R_{3,z}) \frac{k_{z,n} + \Delta t R_{3,k_z}}{\sqrt{\left(k_{x,n} + \Delta t R_{3,k_x}\right)^2 + \left(k_{y,n} + \Delta t R_{3,k_y}\right)^2 + \left(k_{z,n} + \Delta t R_{3,k_z}\right)^2}} + V_{z,n}(x_n + \Delta t R_{3,x}, y_n + \Delta t R_{3,y}, z_n + \Delta t R_{3,z})$$

Solve for wavenumber

$$R_{4,k_x} = 0$$

$$R_{4,k_y} = 0$$

$$R_{4,k_z} = -\sqrt{\left(k_{x,n} + \Delta t R_{3,k_x}\right)^2 + \left(k_{y,n} + \Delta t R_{3,k_y}\right)^2 + \left(k_{z,n} + \Delta t R_{3,k_z}\right)^2} \frac{\partial c}{\partial z}(x_n + \Delta t R_{3,x}, y_n + \Delta t R_{3,y}, z_n + \Delta t R_{3,z}) - \left(k_{x,n} + \Delta t R_{3,k_x}\right) \frac{\partial V_x}{\partial z}(x_n + \Delta t R_{3,x}, y_n + \Delta t R_{3,y}, z_n + \Delta t R_{3,z})$$

5. Obtain the final results at the next time step:

Solve for ray path location

$$x_{n+1} = x_n + \frac{\Delta t}{6} (R_{1,x} + 2R_{2,x} + 2R_{3,x} + R_{4,x})$$

$$y_{n+1} = y_n + \frac{\Delta t}{6} (R_{1,y} + 2R_{2,y} + 2R_{3,y} + R_{4,y})$$

$$z_{n+1} = z_n + \frac{\Delta t}{6} (R_{1,z} + 2R_{2,z} + 2R_{3,z} + R_{4,z})$$

Solve for wavenumber

$$k_{x,n+1} = k_{x,n}, \quad k_{y,n+1} = k_{y,n}, \quad k_{z,n+1} = k_{z,n} + \frac{\Delta t}{6} (R_{1,k_z} + 2R_{2,k_z} + 2R_{3,k_z} + R_{4,k_z})$$

If this procedure is followed iteratively for all propagation steps, the HRT ray paths will be tracked in space (as demonstrated in chapter 3 for the second order Runge-Kutta method).

APPENDIX E: NREL 5-MW BLADE PROPERTIES

The following data corresponds to a NREL-5-MW and was obtained from J. M. Jonkman et al. (2009), as shown in Table E.1.

Table E.1: NREL 5-MW distributed blade properties (J. M. Jonkman et al., 2009).

Blade Span (m)	Blade Twist (deg.)	Blade Chord (m)	Airfoil
0.000	13.308	3.542	Cylinder_1
1.367	13.308	3.542	Cylinder_1
4.100	13.308	3.854	Cylinder_1
6.833	13.308	4.167	Cylinder_2
10.25	13.308	4.557	DU99-W-405
14.35	11.48	4.652	DU99-W-350
18.45	10.162	4.458	DU99-W-350
22.55	9.011	4.249	DU97-W-300
26.65	7.795	4.007	DU91-W2-250
30.75	6.544	3.748	DU91-W2-250
34.85	5.361	3.502	DU93-W-210
38.95	4.188	3.256	DU93-W-210
43.05	3.125	3.010	NACA-64-618
47.15	2.319	2.764	NACA-64-618
51.25	1.526	2.518	NACA-64-618
54.67	0.863	2.313	NACA-64-618
57.40	0.37	2.086	NACA-64-618
60.13	0.106	1.419	NACA-64-618
61.50	0	1.419	NACA-64-618